Master Thesis, Department of Geosciences

Estimating the sulphur dioxide and ash emissions from the Grímsvötn 2011 volcanic eruption and simulating their transport across Northern Europe

Eldbjørg Dirdal Moxnes

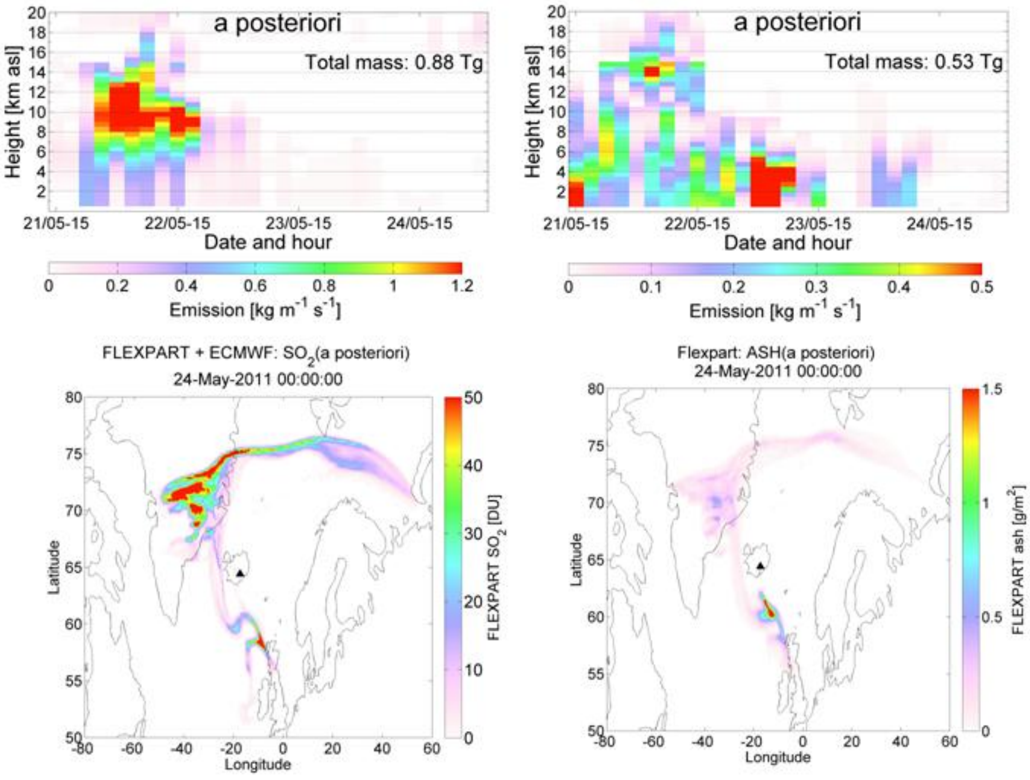

UNIVERSITY OF OSLO

FACULTY OF MATHEMATICS AND NATURAL SCIENCES

Estimating the sulphur dioxide and ash emissions from the Grímsvötn 2011 volcanic eruption and simulating their transport across Northern Europe

Eldbjørg Dirdal Moxnes

Master Thesis in Geosciences

Discipline: Meteorology

Department of Geosciences

Faculty of Mathematics and Natural Sciences

University of Oslo

1 June, 2013

Abstract

A volcanic eruption releases gases and solid matter into the atmosphere. Eruptions that inject SO_2 deep into the atmosphere are particularly important for the Earth's climate because this can lead to perturbation of the radiation transmission in the atmosphere. Additionally, if volcanic ash is injected at flight altitudes, aircraft can encounter dangerous engine damage. To accurately model and predict the transport of SO_2 and ash, information of the source term (the amount of material being emitted to the atmosphere and its variations with time and altitude) is needed. This is not easy to measure directly as satellites normally only observe the total amount of ash or SO_2 in the atmospheric column. An inversion method is used to estimate the source terms for SO_2 and ash from the Grímsvötn eruption in May 2011. The method takes input from a dispersion model and satellite observations as well as several a priori source estimates. The Lagrangian particle dispersion model, FLEXPART, run on two different meteorological analysis data sets, is used to simulate the transport of ash and SO_2 emitted by the eruption. Simulations are carried out for a large number of emission times and altitudes above the volcano where the particles are released and subsequently tracked in the model atmosphere. Modelled total atmospheric columns from the various emission times and altitudes are compared with satellite observations from two different satellite instruments (IASI and SEVIRI). The misfit between the observations and the model results is minimized by making a linear combination of the emissions from the different times and altitudes. In this way, a source term for the volcanic emissions is obtained. The inversion method is performed for SO_2 and ash separately. The inverted source terms for Grímsvötn show that the SO_2 was emitted mostly to high altitudes (from 8-12 km) over a period of about 21 hours (21 May 21 UTC to 22 May 18 UTC). The ash was emitted mostly to low altitudes (below 5 km) in several emission pulses during roughly 51 hours over the time period 21 May 12 UTC to 23 May 15 UTC. Some ash was also emitted to higher altitudes together with the SO_2. FLEXPART forward runs are performed using the inverted source terms for ash and SO_2 to examine the similarities and differences in the subsequent transport patterns of the two substances. The transport simulations show that the SO_2 is transported mostly north-westward and the ash mostly south-eastward. This corresponds well with independent satellite observations from GOME-2 and SCIAMACHY (for SO_2) and measured aerosol mass concentrations at different surface stations in Scandinavia (for ash). This demonstrates that the inversion method, in this case, is able to distinguish between emissions and transport of SO_2 and ash. The method is useful for improving the forecasts of ash and SO_2 in case of volcanic eruptions, which will aid aviation and help evaluate any potential climate impacts.

Acknowledgements

First, I would like to thank my supervisor Nina Kristiansen at NILU for teaching me all that was needed and guiding me through this study, and always in a positive and encouraging style. I could not have done this without you. I also thank my supervisor Andreas Stohl for professional guidance and getting me back on track all the times I was completely lost.

I thank Lieven Clarisse for providing me IASI satellite data and being very helpful in answering questions. Thanks to Fred Prata for sharing SEVIRI ash data, and Throstur Thorsteinsson and the University of Iceland for sharing ash ground sample data. I would also like to thank Arve Kylling for providing me with SEVIRI ash data that was used temporarily during this work.

Many thanks to my mum and dad for financing my study life and for not kicking me out of the house, and to all of my friends in skiing and running for the exhausting work-outs, hard competitions and interesting discussions that broke up and lightened everyday life. I would also like to thank my boyfriend for always being there for me, patient and kind.

Abbreviations and acronyms

AIRS	Atmospheric Infrared Sounder (on AQUA satellite)
a.g.l	Above ground level
a.s.l	Above sea level
AURA	A NASA satellite
AVOID	Airborne Volcanic Object Infrared Detector – Camera to detect ash
CALIOP	Cloud-Aerosol LIdar with Orthogonal Polarization
CALIPSO	Cloud-Aerosol Lidar and Infrared Pathfinder Satellite Observation
DOAS	Differential Optical Absorption Spectroscopy
ECMWF	European Centre for Medium-Range Weather Forecasts
ENVISAT	Environmental Satellite
EUMETSAT	European Organisation for the Exploitation of Meteorological Satellites.
FLEXPART	A Lagrangian dispersion model
GEOS-CHEM	A global 3-D atmospheric composition model
GFS	Global Forecast System
GOME-2	Global Ozone Monitoring Experiement-2(instrument on MetOp-A satellite)
GVP	The Smithsonian Institution's Global Volcanism Program
HIRS	High resolution Infrared Sounder
IASI	Infrared Atmospheric Sounding Interferometer (on MetOp satellite)
ICAO	International Civil Aviation Organization
IMO	Icelandic Meteorological Office
LIDAR	Light Detection And Ranging
MER	Mass Eruption Rate
MODIS	Moderate-Resolution Imaging Spectroradiometer
MSG	Meteosat Second Generation
MetOp-A	Polar orbiting meteorological satellite operated by EUMETSAT
NAME	Numerical Atmospheric-dispersion Modelling Environment (NAME)
NASA	National Aeronautics and Space Administration
NCEP	U. S National Centers for Environmental Prediction
NOAA/ESRL	National Oceanic & Atmospheric Administration (U.S Department of Commerce), Earth System Research Laboratory.
NWP	Numerical Weather Prediction
OMI	Ozone Monitoring Instrument (on AURA satellite)
RADAR	Radio Detection and Ranging
SCIAMACHY	SCanning Imaging Absorption SpectroMeter for Atmospheric CHartographY)
SEVIRI	Spinning Enhanced Visible and Infrared Imager
TOMS	Total Ozone Mapping Spectrometer
VAAC	Volcanic Ash Advisory Center

Contents

Chapter 1

Introduction

There are about 500 active terrestrial volcanoes on Earth. Of these, approximately three percent erupt each year. Ten percent of these (on average 1.5 each year) are so explosive that gases and particles may be transported into the stratosphere (Brasseur et al., 1999). Volcanic emissions consist of a mixture of gases, aerosols and silicate particles which collectively span seven orders of magnitude in size (Durant et al., 2010). The composition of the type of gases and the size of the particles vary greatly among the different volcanoes. The main gas components erupted are normally H_2O (70%), CO_2 (20%) and SO_2 (6%) (Brasseur et al., 1999).

Eruptions that inject material deep into the stratosphere are particularly important for Earth's climate. SO_2 in the atmosphere is converted to sulfate aerosols, which have a long residence time in the stratosphere. The aerosols perturb the radiation transmission by scattering sunlight and thus possibly increase the Earth's albedo and cool the planet (Textor et al., 2003).

The term "tephra", Greek for "ash", describes all fragmented material ejected during explosive volcanic eruptions that travels through the atmosphere (Durant et al., 2010). The full size distribution of tephra is given in figure 1.1. The volcanic ash is a subset of tephra and includes particles smaller than 2000 µm in diameter. The volcanic ash can further be separated into fine ash ($d < 63$ µm) and coarse ash (63 µm $< d < 2000$ µm) (see figure 1.1). The larger particles fall out of the atmosphere within minutes to hours and are deposited close to the volcano, while the smaller particles can remain in the atmosphere for days and be transported long distances away from the volcano. Volcanic ash that is deposited on the Earth's surface or suspended in the surface air (or in the higher altitude levels), may also have several effects on environment and climate. Additionally, if ash is injected at flight altitudes aircrafts can experience dangerous engine damage (Prata and Tupper, 2009).

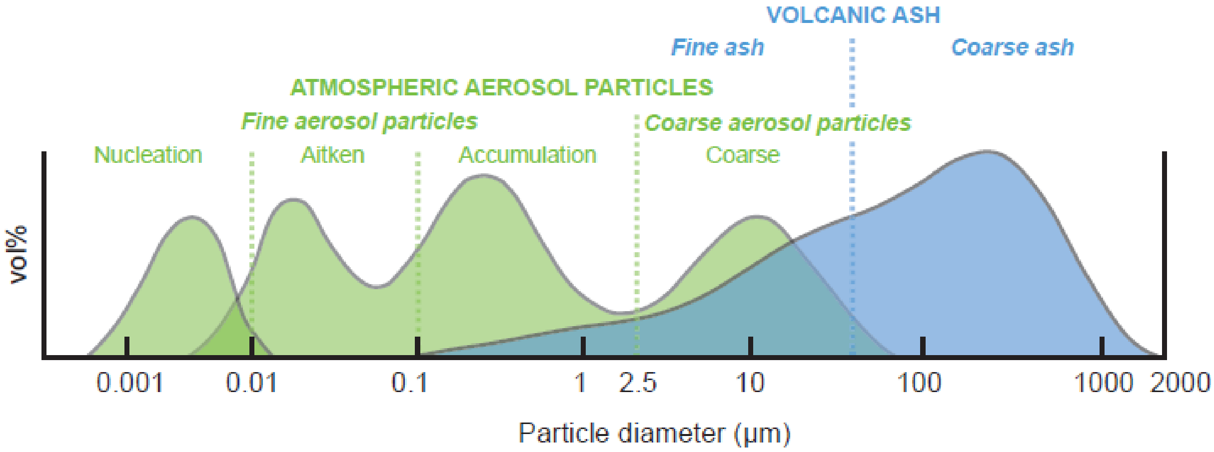

Figure 1.1: *The full size range of tephra. The subset volcanic ash is shown as the blue distribution and the other subsets are colored green. Taken from Durant et al. (2010)*

Modelling and forecasting the transport of ash and SO_2 depends critically on the knowledge of the emission strength as a function of altitude and time, called the *source term*. An estimate of the source term is, unfortunately, difficult to obtain by direct measurements. The major goal of this study is to estimate the source terms of SO_2 and ash from the eruption of the Grímsvötn volcano in May 2011 and accurately simulate the atmospheric transport of SO_2 and ash from the eruption. An inversion method that uses both simulated and observed columns of SO_2 and ash is used to estimate individual source terms for SO_2 and ash for the Grímsvötn eruption.

Further, model simulations using the obtained source term are performed with a Lagrangian particle dispersion model, FLEXPART. The transport of SO_2 has often been used as an approximation for ash transport. This is quite a strong assumption that might lead to large errors in the forecasts for ash. Measurements from several previous eruptions have shown that SO_2 and ash may take different transport directions in the days following an eruption (e.g. Prata and Kerkmann, 2007; Kerminen et al., 2011). The method used in this study will be tested for whether it can distinguish between the emissions of SO_2 and ash and the subsequent transport. If successful, the model will make it possible to more accurately consider the potential climate impact of a large volcanic eruption and improve forecasting for aviation.

Chapter 2

Background

This chapter begins with an introduction to volcanoes, moving on to SO_2 and ash, their effects on climate and environment, and how their concentrations can be detected and forecasted. Further on follows a description of the SO_2-ash separation processes, wind and transport in the atmosphere and a section presenting methods to estimate the source term. The chapter ends with an elaboration of the Grímsvötn volcano investigated in this thesis.

2.1 Volcanoes and classification

The word *volcano* is derived from the name of Vulcano, a volcanic island in the Aeolian Islands of Italy whose name in turn originates from Vulcan, the name of a god of fire in Roman mythology[1]. A volcano is an opening or fracture in the Earth’s surface or crust, and is generally found where tectonic plates are diverging or converging (see figure 2.1). Volcanoes can also form where there is a stretching and thinning of the Earth's crust in the interiors of plates. The large tectonic plates move relatively slowly with a movement of millimeters to centimeters per year. The movements allow melted stones and gases to enter the surface from the interior of Earth. As long as it is below the Earth’s surface, the mass of melted stones is named *magma* while the name changes to *lava* when entering the surface.

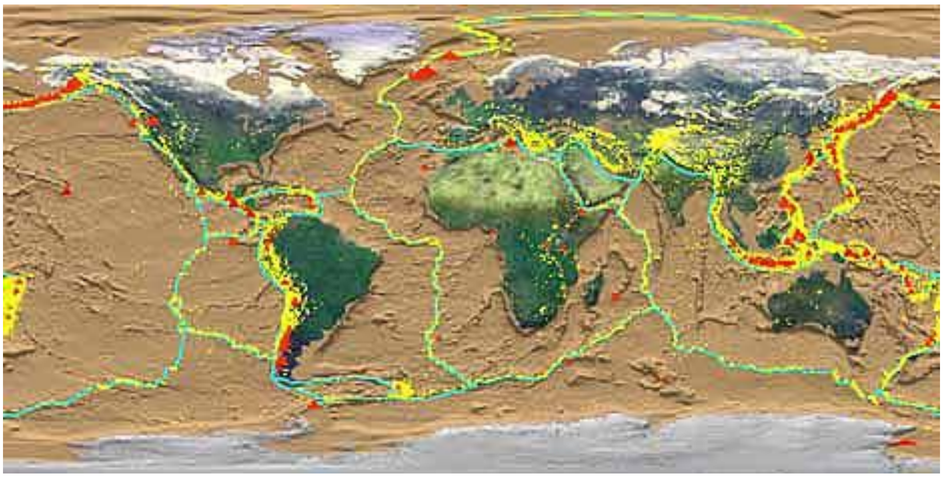

Figure 2.1: *Map of the world showing the tectonic plates boundaries (neon lines), recent earthquakes (yellow dots) and active volcanoes (red triangles) Source: NASA.*

---

[1] From Online Etymology Dictionary found here: http://www.etymonline.com/

There are several ways to classify volcanoes, one of which is based on the eruption mechanism. There are three main types in this classification (Schminke, 2004):

1. *Magmatic eruptions* caused by decompression of gas within magma.

2. *Phreatic eruptions* caused by superheating of steam via contact with magma.

3. *Phreatomagmatic* eruptions caused by compression of gas within magma. When magma is rising through the Earth’s crust it carries a great amount of thermal energy. When this hot magma comes in contact with water or ice an insulating vapor film can form (Zimanowski, 2000). Eventually this vapor film will collapse leading to direct coupling of the cold water and hot magma. The water then quickly converts to its gaseous state (steam) via the transfer of thermal energy. This is due to the second law of thermodynamics, which states, “isolated systems spontaneously evolve towards thermodynamic equilibrium – the state of maximum entropy”.[2] The conversion of liquid water to steam is typically associated with a significant increase in the volume of the water molecules. Because the magma and surrounding country rock can be viewed as a finite space, the rapidly expanding water can cause the surrounding rock/magma to mechanically fail, which means that the rock breaks into fragments. Fragmentation causes an increase in contact area between magma and water, creating a feedback mechanism, and leading to further fragmentation and the production of many small particles (Zimanowski, 2000). The efficiency of the fragmentation process (i.e. to what degree the surrounding rocks are broken apart) is a function of the confining pressure and the water-to-magma ratio (Sheridan and Wohlerz, 1983). The optimum range of water-to-magma ratios to fuel an explosive event is 0.1-0.3. The result of the interaction between water and magma is that, due to the higher fragmentation, the particles erupted are much finer-grained than in other explosive eruptions (Morrissey et al., 2000).

The three types of mechanisms lead to four types of eruptions in terms of activity (Cas and Wright, 1987). One type of activity is based on the content of the erupting magma. A volcano is said to be felsic if the erupting magma contains more than 63 % of silicia (silicon dioxide, SiO_2). Magma with high silicia content has high viscosity (i.e. it is “sticky”, it flows slowly); the gas bubbles are trapped and gas pressure can build up. This leads usually to *explosive* eruptions. Another type of activity arises if the magma contains less than 52 % silicia. Then the volcano is called mafic. The magma is then less viscous (i.e. “runny”, it flows more easily) and gas bubbles can easily travel through the magma and escape. Then the eruption usually is *effusive,* which means that the lava pours out without significant explosive activity, typically sliding silently down the sides of the volcano. Between those two main categories lies the intermediate category which includes erupted magma containing 52-63 % silicia. These volcanoes generally only occur above subduction[3] zones such as Mount Merapi in Indonesia. The fourth and last category contains the very rare eruptions with magmatic silicia content less than 45 %.

---

[2] The entropy of a gas is much larger than that of a liquid.

[3] Subduction zones are regions with convergent plate movement, i.e. were one tectonic plate moves under another and then sinks into the mantle.

The so-called Volcanic Explosivity Index (VEI) (Newhall and Self, 1982) can tell something about the size of the eruption. The volume of products, eruption plume height and qualitative observations are all used to determine the VEI for each individual eruption. The scale starts at 0, applying to non-explosive eruptions. The scale is logarithmic and has no end, and the terms range from "gentle" to "mega-colossal" (see table 1). The largest value used until now is category 8 for the eruption of Lake Toba (North Sumatra, Indonesia) 69,000 to 77,000 years ago. The famous eruptions of Krakatoa (Indonesia) in 1883 and Mount Pinatubo (Philippines) in 1991 are, for example, both categorized with a value of 6.

VEI	Ejection volume	Plume Height	Description	Recurrence
0	$<10^4$ m^3	<100m	Effusive	Continuous
1	$>10^4$ m^3	100-1000m	Gentle	Daily
2	$>10^6$ m^3	1-5 km	Explosive	Weekly
3	$>10^7$ m^3	3-15 km	Severe	Few months
4	>0.1 km^3	10-25 km	Cataclysmic	Decade
5	>1 km^3	>25 km	Paroxysmal	Few decades
6	>10 km^3	>25 km	Colossal	Century
7	>100 km^3	>25 km	Super-colossal	Millennium
8	>1000 km^3	>25 km	Mega-colossal	10,000 years

Table 1: *The different values of VEI (Volcanic Explosivity Index)*
(Source: http://www.almanac.com/content/volcanoes-how-measure-volcanic-eruptions)

2.2 SO_2 and ash in the atmosphere

CO_2 and H_2O are the most abundant gases emitted during a volcanic eruption and they both work as climate gases. However, their concentrations in the atmosphere are already so high that contributions from volcanic eruptions are more or less negligible. The background concentration of sulphur dioxide, SO_2, however, is small, so additional amounts easily becomes significant (Brasseur et al., 1999).

SO_2 is an invisible gas with a nasty and sharp smell. The effect of the SO_2 emissions from a volcanic eruption is dependent on the height of the plume. At surface level, the gas is recognized as a health hazard that causes inflammation and irritation of the eyes and respiratory tract. In the atmosphere, SO_2 is converted into sulfuric acid (H_2SO_4) by the following reactions (Jacob, 1999):

$$\mathrm{SO_2 + OH + M \leftrightarrow HSO_3 + M} \qquad (2.1)$$

$$\mathrm{HSO_3 + O_2 \leftrightarrow SO_3 + HO_2} \qquad (2.2)$$

$$\mathrm{SO_3 + H_2O + M \rightarrow H_2SO_4 + M} \qquad (2.3)$$

H_2SO_4 then condenses rapidly to form fine sulphate (SO_4^{2-}) aerosols. The lifetime of SO_2 against reaction with OH (reaction 2.1) is 1-2 weeks. There is another reaction chain that is much faster and is therefore thought to provide the most dominant atmospheric pathway for oxidation of SO_2 to sulphate aerosols:

$$SO_2 \leftrightarrow SO_2 + H_2O \qquad (2.4)$$

$$SO_2 + H_2O \leftrightarrow HSO_3^- + H^+ \qquad (2.5)$$

$$H_2O_2 \leftrightarrow H_2O_2 \qquad (2.6)$$

$$HSO_3^- + H_2O_2 + H^+ \rightarrow SO_4^{2-} + 2H^+ + H_2O \qquad (2.7)$$

The results of reaction 2.1-2.3 and 2.4 – 2.7 are the same: increased levels of sulphate aerosols in atmosphere. The lifetime of these aerosols in the troposphere is short (1-3 weeks) mostly due to wet deposition. In the stratosphere, however, there is little wet deposition, and the aerosols have a much longer lifetime (1-3 years) and hence any environmental impact from stratospheric sulphate aerosols can last for much longer than for those in the troposphere.

The *direct effects* of the stratospheric sulphate aerosols are the warming of the stratosphere due to the aerosols' absorption of solar and terrestrial radiation, and the cooling of the troposphere because of the aerosols blocking of direct sunlight. The anthropogenic emissions of sulphate aerosols are about ten times larger than the volcanic contribution (see table 2). Despite this, the radiative anthropogenic forcing is only slightly larger (IPCC, 2007). This is because the emitted material from a volcano normally reaches higher altitudes than the material emitted from surface level.

Source	**% of total sulphate aerosol burden**
Anthropogenic	
-Fossil fuel burning	72
-Biomass burning	2
Natural	
-Marine phytoplankton	19
-Volcanoes	7

Table 2: *The contributions to the total sulphate aerosol burden. Numbers taken from IPCC(2007)*

The cooling effect from sulphate aerosols has partly neutralized the climate warming due to greenhouse gases increase during the 20th century (Dufresne et al., 2005). The change in reflected radiation at the top of atmosphere due to the scattering and absorption of radiation by (anthropogenic) sulphate aerosols has ranged from -0.3W/m^2 to -0.9 W/m^2 in different publications (see Penner et al., 1998). The amount of reflection depends nonlinearly on the relative humidity and it is found that by not allowing the relative humidity to increase above 90 %, the effect could decrease from -0.9 to -0.55 W/m^2. In temperature, the cooling effect is estimated to 0.5 K (Dufresne et al., 2005). For comparison, the increase in greenhouse gases has led to a warming of 1.4 K.

It has been suggested to use anthropogenic SO_2 injections into the atmosphere to increase tropospheric cooling and thereby reduce global warming (e.g. Wigley, 2006). However, there are still many uncertainties regarding this suggestion. For example effects such as winter warming, altered rainfall patterns and ozone depletion are not understood well enough (Robock, 2000). Continuous and long-term altering of the climate system may also have additional effects beyond short-term volcanic impacts.

The *indirect effect* of stratospheric sulfate aerosols is a very non-linear function of the aerosol burden and therefore not easy to predict. It is, however, clear that as the sulphate aerosols grow and coagulate, they settle into the upper troposphere where they work as cloud condensation nuclei (Textor et al., 2003). The resulting increased concentrations of droplets and the decrease in their sizes, change the clouds' optical properties and thereby further modify the Earth's radiation balance.

Sulphate in the stratosphere also influences the atmospheric circulation. Graf et al. (2007) show that in winters with volcanic activity, the production of planetary wave energy in the troposphere is higher. The stratospheric flux is also increased, so the result is a higher concentration of wave energy in the stratosphere that is expected to affect the North Atlantic Oscillation[4].

Another important climate effect comes from the heterogeneous reactions that happen at the sulphate aerosols in the stratosphere. The most likely ones are (Brasseur et al., 1999):

$$\mathrm{N_2O_5 + H_2O \rightarrow 2HNO_3} \qquad (2.8)$$

$$\mathrm{ClONO_2 + H_2O \rightarrow HNO_3 + HOCl} \qquad (2.9)$$

The products of these reactions lead further to reactions that alter chlorine and nitrogen chemical species in the stratosphere. This generates chlorine monoxide (ClO), which destroys ozone. The ozone layer is located in the lower stratosphere, absorbing ultraviolet heating and thereby leading to radiative heating. Studies of the effect of these reactions have shown significant ozone reduction over middle latitudes. For example, analyses have shown that the global amount of ozone was reduced by 4 % over a period of 2-3 years after the famous Mount Pinatubo (Philippines) eruption in June 1991 (Randel et al., 1995)

Ash deposited at the Earth's surface or located in the surface air and at higher altitude levels might also have several effects on environment and climate. Seifert et al. (2011) found that the ash particles from the large eruption of the Eyjafjallajökull volcano in April 2010 lead to stronger heterogeneous ice nucleation in tropospheric clouds. They evaluated 90 cloud cases over central Europe and found that all clouds with temperature below -15 degrees contained ice. Typically clouds in this geographical area do not contain ice before their temperatures are below -25 degrees.

---

[4] The North Atlantic Oscillation (NAO) is a climatic phenomenon regarding fluctuations in the difference of atmospheric pressure at sea level between the semi-permanent center of low pressure found between Iceland and southern Greenland, Icelandic low, and the semi-permanent center of high pressure found north-west of Africa in the Atlantic Ocean.

Deposition of ash on snow and ice can darken the surfaces. The result of this is an increase in absorbed energy which can lead to earlier melting and might change the Earth's albedo by reflecting less sun light (United States Environmental Protection Agency, [EPA]). Changes in melting time and magnitude may also cause problems for populations using melted water as potable water.

Coarse mode particles, defined as particles in the interval from PM2.5 to PM10[5], might have health implications if found in high concentrations in the surface layer. Figure 2.2 shows volume size distributions measured in Stockholm, Sweden, during the Grímsvötn May 2011 eruption. The figure shows that the distribution during the ash episode looks quite similar to an episode showing the dust from studded winter tires and winter sanding.

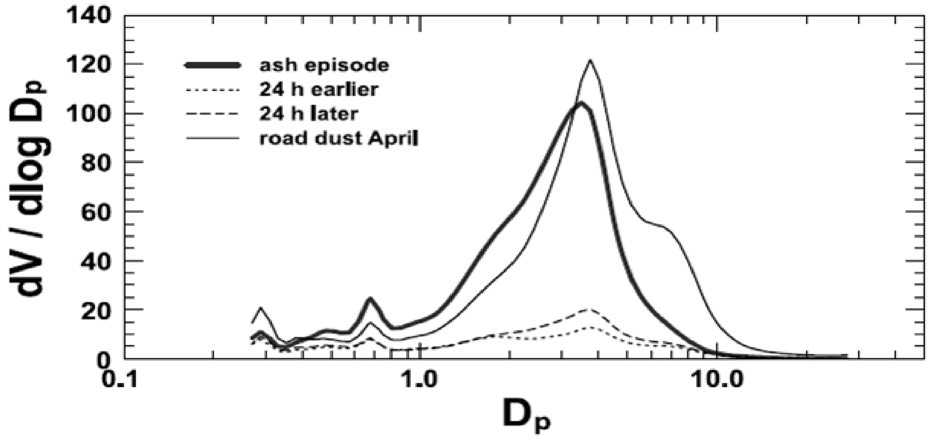

Figure 2.2: *Volume size distributions showing the ash episode from 22 UTC at 24 May 2011 to 06 UTC at 25 May 2011 together with the distribution one day before and one day after and a distribution measured during road dust in April. Measurements from Stockholm, Sweden. Figure taken from Tesche et al. (2012)*

The EU directive from 2008 states that daily mean PM10 concentrations should not exceed 50 µ/m^3 more than 35 days a year (EU directive 2008/50/EG). Tesche et al. (2012) report that the daily mean concentrations during the Grímsvötn 2011 eruption did not exceed 25-45 µ/m^3 at any of their measurements sites (18 sites in Sweden and in the southern parts of Finland and Norway) but during a longer lasting volcanic eruption combined with stationary meteorological conditions, this might happen. Several studies also show increased mortality associated with coarse mode particles. For example, a recent study by Meister et al. (2012) indicates an increased mortality of 1.68% per 10 µ/m^3 increase of coarse mode particles.

Aside from the climate impacts and health hazards of volcanic emissions, volcanic ash can also significantly affect air traffic. Silicate (SiO_4^{4-}), the primary component of volcanic ash, has a melting temperature that is lower than the operating temperatures of modern jet engines.

---

[5] PM=Particulate Matter
PM10: Particles with an aerodynamic diameter < 10 micrometer.
PM2.5: Particles with an aerodynamic diameter < 2.5 micrometer.

Because of this, ash particles can melt and then accumulate as re-solidified deposits in the jet engine, which can then cause an engine failure. The problems related to aircrafts were first properly recognized and documented following a well-publicized incident involving a British Airways jet and a volcanic cloud from an eruption of the Galunggung volcano in Indonesia in 1982. The aircraft lost power to all engines and reportedly dropped more than 12,000 feet before power was restored to three engines and an emergency landing made at Jakarta (Indonesia). Additionally, the ash particles' geometrical form of angular fragments has the sharpness of a pocket-knife blade that can, upon impact with aircraft travelling at high speeds, cause damage to forward-facing surfaces, including windscreens, fuselage surfaces, compressor fan blades, instruments and electrical components on board (Casadevall et al., 1996). The overall result of an aircraft flying into an ash cloud can therefore be degraded engine performance, loss of visibility and failure of critical navigational and operational instruments.

Bernard and Rose (1984) found that SO_2 in high concentrations could also cause fuel contamination, and when converted to sulphate aerosols, damage airframe and windows on air planes.

The hazard to aviation is not only confined to airborne volcanic ash and the potential danger for aircraft flying into a volcanic ash cloud. Significant danger and economic cost occur from ash-fall at airports and on runways in regions vulnerable to volcanic activity. Figure 2.3 shows that there are more than 100 airports around the world with a risk of being affected by volcanic hazards (Guffanti et al., 2004).

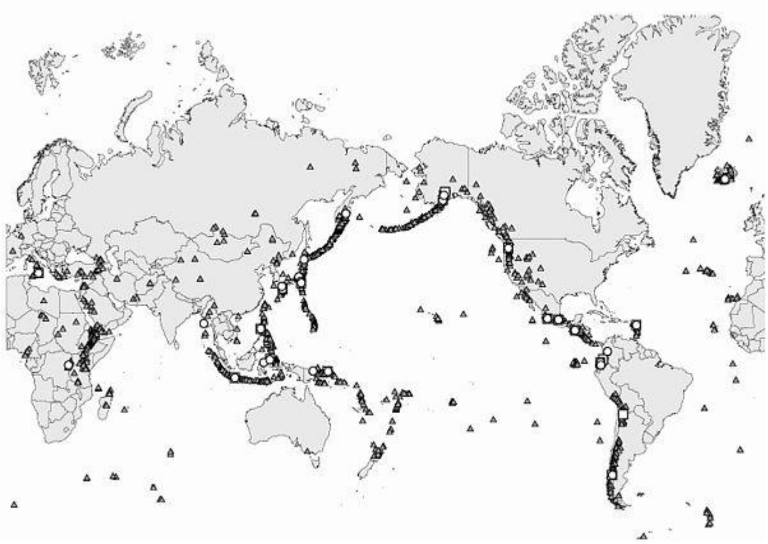

Figure 2.3: *Locations of volcanoes responsible for ash/aircraft encounters, 1973-2000 (circles) and airport closures, 1971-2001 (squares). Active and potentially active young volcanoes are shown with triangles.*
Source: http://www.nwas.org/committees/rs/volcano/ash.htm

Reported aircraft trouble as well as several near catastrophes during the 1980's and 1990's caused sufficient alarm to stimulate the research community into devising ways to detect ash clouds and avoid such hazardous air space. During the 1990's, the Volcanic Ash Advisory Centers (VAACs) under the International Civil Aeronautical Organization (ICAO) of the World Meteorological Organization (WMO) were formed. There is today one VAAC for each of the nine regions of the world (see figure 2.4). The purpose of the VAAC is to collect information from volcano observatories, satellite images and pilot reports on ash clouds released by volcanoes. The information is analyzed and transport models are used to forecast the further movement of the ash cloud. The forecasts are distributed to adjacent VAACs and to interested parties as Meteorological Watch Offices and Area Control Centers for aircraft. Before the eruption of Eyjafjallajökull (Iceland) in 2010, the International Civil Aviation Organization (ICAO) was operating with zero limits for ash (ICAO, 2007). If any ash was predicted or observed in the air space, flights were restricted or cancelled. During the Eyjafjallajökull eruption this led to closures of the controlled airspace in many European countries, resulting in the largest air traffic shutdown since World War II (Zehner, Ed. 2012). However, in the ending phase of the eruption of Eyjafjallajökull, the International Civil Aviation Organization changed from zero tolerance to the following ash concentration limits applying to the European area (ICAO, 2010):

i) Flight allowable when ash concentration is below 2×10^{-3} g/m^{3}.
ii) Flight allowable under certain specific conditions when concentration is in
the range 2-4 x 10^{-3} g/m$^{3.}$
iii) Flight prohibited when concentration is larger than 4×10^{-3} g/m^{3}.

These limitations were in operational use during the Grímsvötn eruption of May 2011 and caused cancellation of several flights over Europe. The closure of air traffic was generally based on the volcanic ash forecasts issued by the responsible VAAC (London and Toulouse) but airlines could also individually regulate their flight routes after having a safety case approved by the responsible civil aviation authority. This led to a situation that was very different than during the eruption one year earlier when most air traffic was grounded.

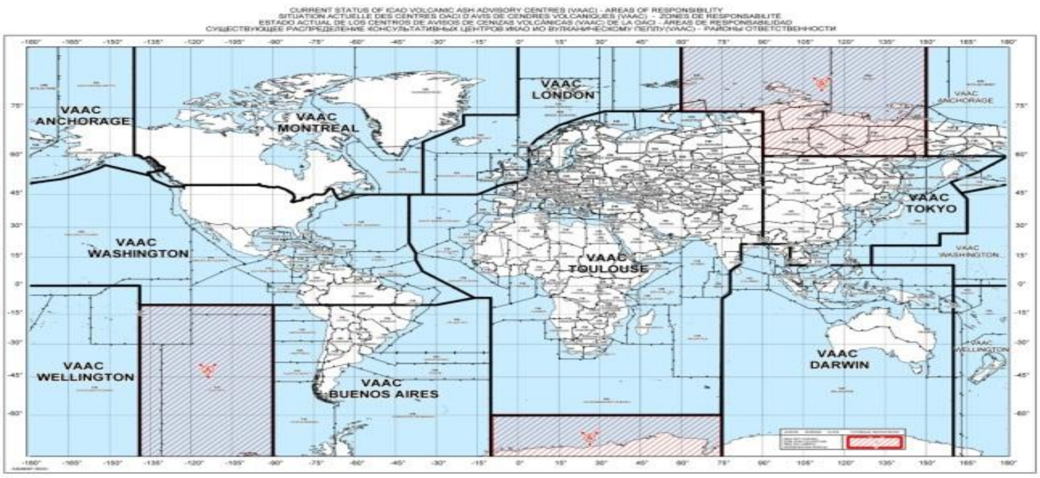

Figure 2.4: *Coverage of the nine VAAC's.*
Source: http://www.icao.int/anb/iavwopsg/VAAC06.ppt

2.3 Detecting and forecasting volcanic SO_2 and ash

The currently most common way to detect volcanic ash and SO_2 is by using measurement techniques involving instruments on satellites. Compared to ground-based measurements, satellites provide a comprehensive cartography of volcanic emissions at a global scale and with different resolution, but only the strongest sources are picked up due to limitations in the ground resolution and/or sensitivity of the current sensors (Theys et al., 2012). In recent years the quality and precision of the instruments have improved and today there exist instruments that measure in the visible (VIS), ultra-violet (UV) and infrared (IR) parts of the electromagnetic spectrum (see fig. 2.5), all of which can be used to retrieve information about volcanic emissions.

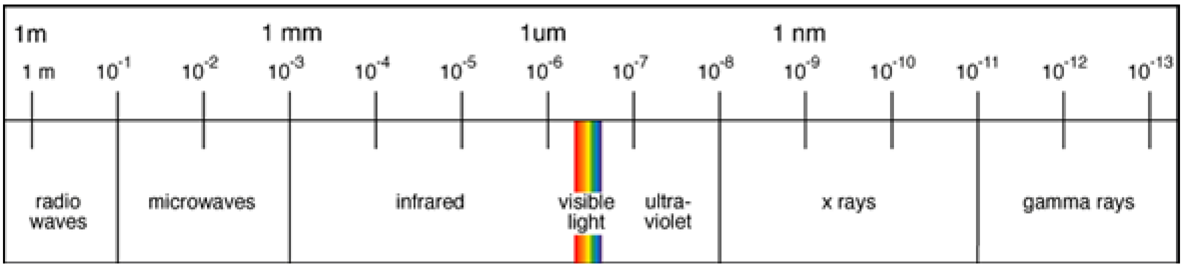

Figure 2.5: *The electromagnetic spectrum.*
Source: http://www.columbia.edu/~vjd1/electromag_spectrum.gif

Different types of instruments are placed on various satellites (see table 3 for an overview). Some satellites are geostationary, meaning that they have an orbital velocity that is almost one sidereal day. Thus, the satellite is locked to the Earths' rotational period and has a stationary footprint on the ground. The altitude of these types of satellites is about 36 000 km and the location is directly above the Equator. The polar orbiting satellites fly at a much lower altitude than the geostationary ones and have less frequent global coverage.

Instrument	**Satellite**	**Type**	**Launched**	**Wave-length**	**Retrieved species**	**Spatial resolution**	**Temporal resolution (images/day)**
SEVIRI	MSG (series of 4 satellites)	Geos.	Aug. 2002	IR/VIS	Ash + SO_2	3 x 3 km^2	96
IASI	MetOp-A	Polar	Oct. 2006	IR	Ash + SO_2	12 x 12 km^2	2
MODIS	NASA-Terra and NASA-Aqua	Polar	Terra: Dec. 1999; Aqua: May 2002	From VIS to IR	Ash + SO_2	1 x 1 km^2	4 (two instruments in orbit)
AIRS	NASA-Aqua	Polar	May 2002	VIS/IR	Ash + SO_2	14x 14km^2	2
GOME-2	MetOp-A	Polar	Oct. 2006	UV/VIS	SO_2	80 x 40 km^2	2
SCIAMACHY	ENVISAT	Polar	Mar. 2002 – Apr. 2012	UV to NIR	SO_2	30 x 60 km^2	1
OMI	AURA	Polar	Jul. 2004	UV	SO_2	24 x 13 km^2	1

Table 3: *Overview of some of the instruments used to detect atmospheric constituents. Data taken from Prata (2008), Theys et al. (2012), www.eumetsat.int and www.nasa.gov*

There are two main types of satellite retrievals: the operational ones and those called “research mode”. Both use retrieval algorithms to estimate the amounts of the wanted species from the radiation measured by the satellite instrument. Before doing the retrievals, many assumptions must be made, as for example the height of plume and the composition of the species. Operational retrievals are made automatically and continuously as new data arrive from a satellite instrument. Thus, the assumptions have to be set in advance of the arrival of data. For the research-mode retrievals, the assumptions can be changed and tuned to fit the actual eruption, e.g. if one knows the approximate height of the plume or the composition of the species. As a consequence of this, the research-mode retrievals may be more accurate than the operational retrievals.

VIS satellite measurements may be useful in *qualitative* detection of ash clouds. The transparency of the atmosphere is then measured. One problem is that, as when using weather imagery, it is difficult to discriminate ash clouds from normal meteorological clouds. SO_2 is transparent, so VIS is not at all useful for detection in that case.

To make *quantitative* measurements, the IR and UV channels must be used. Advantages of IR measurements are that they can measure the Earth both at daytime and nighttime (no need for daylight), thereby providing good global coverage, and that they normally have better spatial resolution compared to UV-measurements (Prata, 2008). Especially for SO_2, the limitation with the IR measurements is that they normally cannot detect any signal from SO_2 in the lower atmospheric layers due to inference with water vapor. The UV measurements, however, have the advantage of better resolution below 5 km height, but are restricted to only observe during daytime.

SO_2 has strong and distinctive structures in its absorption spectrum both at UV and IR wavelengths. therefore both parts of the spectrum are useful for quantitative measurements. Since 1979, the Total Ozone Mapping Spectrometer (TOMS) and follow-up instruments have been measuring SO_2 in the UV spectral range (Krueger 1983, Krueger et al., 1995), although with a rather poor detection limit. In the IR, the measuring of SO_2 by satellite instruments began in 1979 with data from High resolution Infrared Sounder (HIRS) (Prata, 2008). Over the last two decades, improved spectral resolution, coverage, sensitivity and spatial resolution have all improved in SO_2 satellite measurements (Theys et al., 2012).

The first detections of volcanic ash by satellite instruments occurred in 1987, via weather satellite imagery. The detection rate was very low because of interference from meteorological clouds (Prata, 2008). Later, ash has mostly been measured in the IR channels. The original method for detecting ash clouds by use of satellite IR imagery was proposed by A. J. Prata in 1989. The split-window technique (Prata, 1989) is one example of a retrieval method operating in the IR channel. The silicate particles in an ash cloud absorb and scatter infrared radiation from other wavelengths than water and ice in a meteorological cloud. Thus, by taking the difference between two images acquired at two different wavelengths (11 and 12 μm) within the IR window it is possible to detect the ash clouds and distinguish them from other meteorological clouds. UV might also be used to detect ash. In that case, an aerosol absorbing index based on a ratio of two bands is detected (Prata, 2009).

The standard output of satellite SO_2 retrievals is a vertical column i.e. the amount of SO_2 molecules in a vertical column per unit surface area. The amount is generally expressed in Dobson Units (DU) where 1 DU=2.69 x 10^{16} molecules/cm^2. Ash is also measured in total columns and the amount is normally expressed in g/m^2, sometimes referred to as "ash mass loading". This is also the main limitation of satellite measurements, i.e. that they only provide total column values and no vertical resolution. Therefore, from satellite data it is not possible to say at which altitude(s) the volcanic clouds are located.

Even though volcanic ash is hazardous to aircraft, in-situ measurements during a flight through a volcanic cloud could give useful estimates on ash concentrations and particle size distribution. This is in many ways useful for evaluating ash clouds, but there is also a need for an instrument that can send information directly to the cockpit and that is able to detect ash *before* the aircraft flies into the ash cloud. Nicarnica Aviation has recently developed a new system called Airborne Volcanic Object Infrared Detector (AVOID) (*www.nicarnicaaviation.com*). The technology uses two fast-sampling IR imaging cameras to provide information on objects located up to 100 km ahead of the aircraft. The wavelengths used are in the so-called atmospheric window which means that few other atmospheric constituents absorb (and scatter) in the range. If radiation is backscattered from these wavelengths, it is likely that the air contains particles (volcanic ash or small ice particles). The pilot receives information about the particles' concentration in the air and can make adjustments to the flight path in order to bypass them. The pilot will have 5-10 minutes to decide whether to continue or change direction. By using this technology, the area of airspace that needs to be closed during an eruption can be minimized. The use of passive IR radiation allows the device to operate without the need for sunlight and without emitting any radiation. AVOID works equally well during the day or night.

2.3.1 Detailed descriptions of the satellite instruments used in this study

An extended description of the instruments from table 3 used in this study, either as input to the inversion method or for validation of the transport, is given below.

2.3.1.1 IASI

The Infrared Atmospheric Sounding Interferometer (IASI) is carried onboard the Meteorological Operational Satellite-A (MetOp-A) (European Organisation for the Exploitation of Meteorological Satellites [EUMETSAT], *www.eumetsat.int*). The satellite was launched October 10th, 2006, has an expected lifetime of 15 years and is an operational platform meaning that measurements are available in near real-time (3 hours after observation). The MetOp-A satellite has global coverage twice a day. However, since its swath stays the same, it has a larger number of overpasses at high latitudes as e.g. the latitude of the Iceland area. IASI observes in the infrared specter, from 3.7 -15.5 μm in 8461 channels. The spectral range covers three SO_2 absorption bands (Theys et al., 2012),

ν_1 – band at ~ 8.5µm
ν_3 – band at ~ 7.3µm
$\nu_1 + \nu_3$ – combination band at ~ 4µm

as well as volcanic ash and aerosol absorption features typical between 7.7 and 12.5 μm. Analyses have shown that IASI has very good sensitivity to SO_2 at high altitudes, and under favorable conditions, some sensitivity also in the boundary layer (Clarisse et al., 2008).

2.3.1.2 AIRS

The Atmospheric Infra-Red Sounder (AIRS) is onboard the NASA-Aqua polar orbiting satellite and had global coverage twice a day. AIRS measures temperature, water vapor, abundances of trace components in the atmosphere including ozone, carbon monoxide, carbon dioxide, methane, and sulfur dioxide, and detects suspended dust particles (AIRS webpage, *http://airs.jpl.nasa.gov/instrument/how_AIRS_works/*). The measurements are done by using the upward IR radiation from the Earth's surface and from the atmosphere at wavelengths between 3.7 and 15.4 μm. AIRS has 2378 detectors that give good accuracy. AIRS measurements can be used to retrieve SO_2 typically from the 7.3 µm channel (Prata and Bernardo, 2007) and also volcanic ash typically using two channels in the IR in the atmospheric window between 8 and 12 µm.

2.3.1.3 GOME-2

The Global Ozone Monitoring Experiment–2 (GOME-2) instrument is a UV/VIS spectrometer carried onboard the same satellite as IASI, the MetOp-A (*www.eumetsat.int*). The instrument covers the 240-790 nm wavelength interval with a spectral resolution of 0.2-0.5 nm. GOME-2 measures the solar radiation backscattered by the atmosphere and reflected by the surface of the Earth in a nadir[6] viewing geometry. 4096 spectral points from four detector channels are transferred per individual GOME-2 measurement. The spectral range and resolution allows the retrieval of a number of absorbing trace gases as well as cloud and aerosol parameters.

One technique used to retrieve the SO_2 slant column density from GOME-2 is the Differential Optical Absorption Spectroscopy (DOAS) (Platt and Stutz, 2008). The vertical or total column is then derived by use of an air-mass factor based on realistic SO_2 profiles. There are no examples were GOME-2 has been used to detect ash.

---

[6] The nadir direction is the local vertical direction pointing in the direction of the force of gravity at an actual location. (The direction opposite of the nadir is the zenith)

2.3.1.4 SCIAMACHY

The Scanning Imaging Absorption Spectrometer for Atmospheric Chartography (SCIAMACHY) was launched on board the polar orbiting satellite ENVISAT on 1 March 2002 and nadir measurements are available from August 2002 (SCIAMACHY portal, *www.sciamachy.de*). The instrument is an 8 channel grating spectrometer covering the spectral range from the UV to the NIR at moderate spectral resolution. It observes the solar radiation scattered by the atmosphere and reflected from the Earth's surface. A special feature of SCIAMACHY is the alternation between limb[7] and nadir measurements, facilitating the measurement of both vertical profiles from the mesosphere down to the upper troposphere at low spatial resolution and the measurement of total columns at high spatial resolution (up to 30 x 60 km^2 depending on wavelength and solar elevation). The communication with the ENVISAT satellite was lost abruptly on 8 April 2012. Attempts to re-establish contact did not succeed and the end of the mission was declared on 9 May 2012.

One technique used to retrieve the SO_2 slant column density from SCIAMACHY is the same as the one given for GOME-2 in previous section. Like for GOME-2 there are no examples were SCIAMACHY has been used for ash detection.

2.3.1.5 SEVIRI

The Spinning Enhanced Visible and Infrared Imager (SEVIRI) instrument is onboard the Meteosat Second Generation (MSG) satellite (*www.eumetsat.int*). MSG is more precisely a series of four satellites that will operate consecutively until 2020. The satellites are geostationary which means that they have an orbital velocity almost identical to one sidereal day. Thus, the satellite is locked to the Earths' rotational period and has a stationary footprint on the ground. The altitude of the satellite is about 36 km and the location is directly above Equator. SEVIRI observes in 12 channels from visible to infrared. The retrieval of volcanic ash can be done using measurements from SEVIRI in two IR channels (Prata and Kerkmann, 2007). SEVIRI does not observe at a higher latitude than about 70 degrees north and has a lower concentration limit of 0.2 g/m^2 for ash detection (Fred Prata, personal communication).

2.4 Separation of SO_2 and ash

The detection of ash by satellite instruments is more complicated than that of SO_2 because of the complexity of the ash according to different size, geometrical shape and composition. SO_2 is easier to quantify because of low background values and the good sensitivity to absorption in both UV and IR. Due to this, SO_2 measurements have sometimes been used as an approximation for ash (Prata, 2008). This might be far from "correct" as some satellite measurements also show that SO_2 and ash may move in different directions in the days following an eruption. For example Thomas and Prata (2011) found separation in periods of the Eyjafjallajökull eruption in 2010 when they compared SEVIRI ash measurements with SO_2 measurements from a number of IR and UV satellite-based sensors. The separation of SO_2 and ash might happen i) in the eruption process or ii) during transport.

---

[7] Limb measurements: The instrument observes in a slantwise direction through the atmosphere.

i) The SO_2 and ash might be emitted at different time periods of the eruption due to volcanic controls of eruption style. The height of the plume often varies greatly with time (see for example figure 3.3, which shows the ash plume height tops during the Grímsvötn 2011 eruption). The wind speed and direction might also change quickly, so if ash and SO_2 reach the same altitude but at different times, the wind might be different and transport them in different directions. Another issue for separation during the eruption is that SO_2 and ash might be emitted at the same time, but still reach different altitudes again due to the eruption style itself.

ii) The ash and SO_2 might also be emitted together (at the same time and at the same height), but still separate during the transport due to different specific gravities, different settling velocity or to other factors such as geometrical shape (Holasek et al., 1996).

The hot erupted material from a volcanic eruption will ascend in the troposphere with the force of the initial upward velocity of the eruption itself and the thermal heat of the hot material. During the ascent the material is cooled due to the temperature profile of the troposphere. When reaching the tropopause, the temperature profile changes, leading to warmer air above. This creates a blocking inversion layer that hampers further vertical movement. The initial velocity and diffusion processes might still allow the material to move higher, but as is displayed in figure 2.6, the plume starts to spread more in the horizontal direction than in the vertical direction making an “umbrella” shape. Holasek et al. (1996) conducted a series of analogue laboratory experiments to study the motion of such volcanic umbrella plumes from short-lived explosive eruptions. They found that in a period of 10^3 to 10^4 seconds after the simulated “eruption”, the motion of “particles” (here ash) and “gases” (here SO_2) were similar. But later, a clear separation of ash and gas was seen, with the ash lying in the bottom of the umbrella and the gas on top. Only a uniform size distribution of ash particles was used in the experiment and it is likely that the effect of a varying range of sizes may make the separation less well defined. However, the laboratory experiments fit well with what they found when studying the Sakurajima volcano (Japan): plumes, thought to consist of volcanic gas, were observed above plumes of ash. This means that sulphate aerosols might be formed from SO_2 up to a kilometer above the injection height of the ash.

Prata and Kerkmann (2007) conducted the first simultaneous satellite measurements of SO_2 and ash from a real eruption. They used the SEVIRI instrument to look at the eruption of Karthala volcano on the Comoros Island in November 2005. Like Holasek et al. (1996), they found separation of ash and SO_2, but they distinguished between three layers: one quickly moving upper level (approximately at 12 km altitude) SO_2 cloud, a slower moving middle (8 km) ash cloud and a boundary layer (lower than 3 km) consisting of mostly SO_2. By detecting this they question the appropriateness of using SO_2 as a tracer for volcanic ash.

Figure 2.6: *A picture of the Grímsvötn May 2011 eruption column that clearly shows the "umbrella" shape. Taken from Petersen et al. (2011). Photo taken by Photo Bolli Valgarðsson, 21 May 2011 at 19:20 UTC.*

2.5 Wind and transport

When the material is in the atmosphere, the general atmospheric circulation and local winds are essential for the further transport and impact on environment and climate. It is normal that the wind change direction and/or strength with height, i.e. that it is *wind shear*. Following an eruption the material is normally transported over great horizontally distances while the vertical spread is much smaller (1-2 km) (Prata, 2008)

2.5.1 Horizontal transport

The differential heating between low and high latitudes is the basic of air motion. This leads to horizontal pressure gradients that initiate the movement of air as wind. If no other forces were involved, the wind would always flow in the direction of the pressure gradient force. However, the wind is affected by friction that slows the wind and the Coriolis force that changes the wind's direction.

The heating of the tropics makes the pressure surfaces bulge upward and the cooling at the poles make the pressure surfaces bulge downward. This leads to an equator-to-pole motion in the upper levels. This pole ward flux leads to low surface pressure in low latitudes and high surface pressure in high latitudes. This drives an Equator-ward compensating flow at low levels. Together these two flows form a large circulation cell, typically called the Hadley cell.

Another more elaborate model is the three-cell model which divide each of the hemispheres into three different cells, namely a (limited) Hadley cell that circulate air between the tropics and subtropics, a Ferrel cell in the middle latitudes and a polar cell (Aguado and Burt, 1998). Each of the three cells behaves as the large Hadley cell described above and together they form the Trade Winds and the Westerlies, which dominate the horizontal transport in the troposphere. Volcanic clouds in the lower troposphere will tend to follow these main transport patterns. Thus, volcanic clouds from the Equator to 30°N will mainly be transported westward while the clouds between 30°N and 60° N will be transported eastward.

Wind speeds generally increase with height between the surface and tropopause because of decreasing surface friction and because of stronger pressure gradient force. When there are steeply sloping pressure surfaces, there is a strong pressure gradient force resulting in a so called jet stream. Thus, in the middle and upper troposphere the zonal winds are stronger than the meridional. Figure 2.7 (left) shows that the Polar Jetstream is located at middle latitudes and that the Subtropical Jet stream is closer to equator. A jetstream is normally around 9-12 km altitude and the wind speed may reach 100m/s making transport over long distances in just a few hours possible. This can spread volcanic clouds more than 1,000 km in less than 3 hours (Prata 2008). This further leads to volcanic clouds travelling more rapidly in the zonal than in the meridional direction. Figure 2.7 (right) shows the dispersion of SO_2 from three different volcanic eruptions that happened during the same year (2011): Grímsvötn (-17.33°, 64.42°) eruption starting 21 May, Puyehue-Cordón Caulle (-40.59°, -72.12°) starting 3 June and Nabro (13.37°, 41.70°) starting 12 June 2011. The zonal dispersion of the SO_2 cloud is much larger than the meridional, especially for the eruptions at middle/high latitudes.

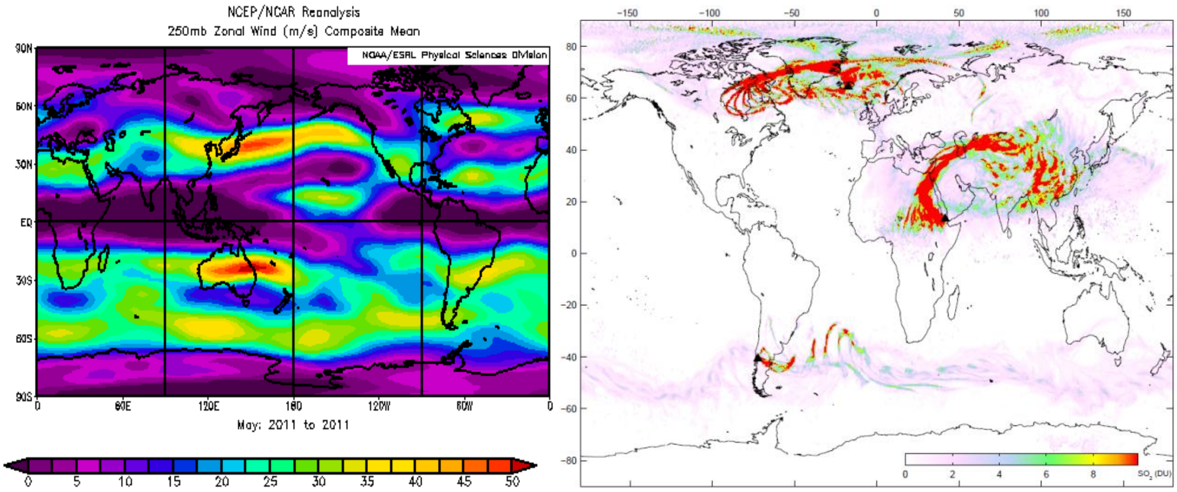

Figure 2.7: *Left: Mean zonal wind at 250 mb in m/s for May 2011. Taken from NOAA/ESRL Physical Sciences Division, see* http://www.esrl.noaa.gov/psd/cgi-bin/data/composites/printpage.pl *Right: Composite image of maximum observed SO_2 columns for the period 20 May to 30 June 2011. The value for each grid cell equals the maximum observed SO_2 columns in that grid cell for the given time period during which three major volcanic eruptions took place. Grímsvötn (−17.33°, 64.42°) erupted first on 21 May, then Puyehue-Cordón Caulle (−40.59°, −72.12°) on 3 June and finally Nabro (13.37°, 41.70°) on 12 June. A plume altitude of 10 km was assumed. Taken from Clarisse et al. (2012)*

2.5.2 Vertical transport

Using only values for the wind speeds in the vertical, the transport time from surface to tropopause is about 3 months. The real value is about 1 month due to the effect of buoyancy. If an object is lighter than the surrounding air, the object will be accelerated upwards. If it is heavier the acceleration will be downward. In addition to the buoyancy, turbulence plays an important part in vertical transport.

Figure 2.8 shows the typical timescales of vertical transport in the atmosphere. The temperature inversion in the stratosphere makes the exchange of air between the troposphere and the stratosphere slower than the mixing inside the troposphere. The timescale is also larger for transport from the troposphere to the stratosphere than in the opposite direction.

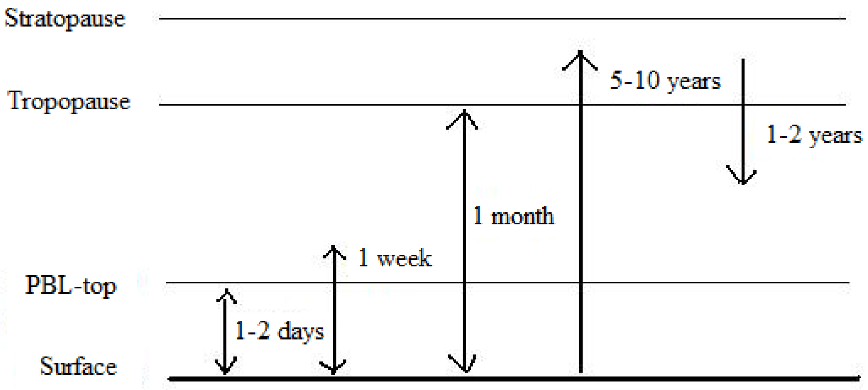

Figure 2.8. *An illustration of the different timescales of vertical transport. Numbers taken from Jacob (1999).*

For SO_2 and ash released at low altitude to be transported into the stratosphere is as figure 2.8 shows a process with very long timescale. A strong volcanic eruption can eject material directly into the stratosphere. The effects of a volcanic eruption are therefore very much dependent on the volcanic strength.

2.6 Methods to estimate the source term

The dispersion modelling of the movement of the ash/SO_2 cloud depends critically on the knowledge of the source term and less on the wind fields, as these are generally known more accurately (Prata, 2008). Unfortunately, the source term is difficult to determine from direct observations and methods. The satellite instruments normally only deliver total columns and cannot alone provide information on the source term.

There exist several methods that attempt to provide an estimate of the source term. One analysis technique that can be used to estimate the initial injection height of both the SO_2 and the ash involves trial-and-error fits between observations of the cloud and model results by guessing the initial height of the volcanic cloud (Prata 2008). The disadvantage with this method is that the model runs and observations are matched by eye, a process that is both subjective and time-consuming. There are also inversion techniques that combine satellite observations and models to estimate the source terms. One such technique is used in this study and is described in chapter 3. Some other methods are described in the two next sections. They are split into two categories: the methods most useful for SO_2 and the methods most useful for ash.

2.6.1 Methods useful for SO_2

There exist a couple of more or less objective and quantitative methods to derive source terms from satellite derived vertical columns of SO_2 (summarized in Theys et al., 2012). The “Box method” considers the SO_2 contained within a circle or box with dimensions that correspond to the total distance travelled by the plume in one day. A correction is made to account for SO_2 loss and the daily flux is then calculated by dividing the mass inside the box with one day. The method may be problematic for low altitudes when the kinetics of the SO_2 reaction is fast and the plume is quickly dispersed.

The “Traverse method” (Merucci et al., 2011) is another technique that may be used to estimate the emission fluxes for SO_2. This technique estimate the emission fluxes by using satellite measurements of the SO_2 mass per unit distance and wind speed. However, the estimates have low spatial and temporal resolution, and not all volcanoes are located in the view of a satellite.

The “Delta-M method” relies on time series of the SO_2 mass obtained by successive satellite overpasses and on an equation for mass conservation which is inverted to yield SO_2 fluxes from SO_2 mass time series as provided by the satellite (Krueger et al., 1996). The equation can be solved analytically assuming a constant flux over a time interval between two mass estimates, or an analytic function can be fitted to the mass series. In the latter, the time dependent flux is obtained by applying the mass conservation to the fitted curve. The advantage of this technique is that it is completely independent of the wind field. The drawback is that it yields only a first order estimate of the fluxes which might yield too smooth fluxes or fluxes with spikes.

2.6.2 Methods useful for ash

The above methods for SO_2 could in theory also be used for volcanic ash emission estimates. However, since the correction of loss of ash (i.e. the lifetime) is much more complex for ash than for SO_2, the techniques are not ideal for ash.

Since ash is visible by eye, an estimate of the height of the ash emissions can be given if the volcanic eruption is observed by people. Aircrafts measurements can in some cases give information on the plume height and, if flying into the ash clouds, information on the composition of the plume can be collected. However, because of safety reasons (see section 2.2), the latter is not preferable and sometimes not possible at all.

In the cases where the volcano is observed by ground-based Weather Radio Detection And Ranging (RADAR) or Light Detection and Ranging (LIDAR), estimates of the plume height can be given. If the LIDAR is located very close to the volcano it can use amounts of backscattered light to detect the height of eruption plume. RADARs can give the height of eruption plumes from measuring the reflexivity of particles (Petersen et al., 2012).

Space-based LIDAR, such as the Cloud-Aerosol Lidar with Orthogonal Polarization (CALIOP) on board the Cloud-Aerosol Lidar and Infrared Pathfinder Satellite Observation

(CALIPSO) platform, can provide height estimates for aerosols and thereby tell something about the eruption plume (CALIPSO webpage, *http://www-calipso.larc.nasa.gov*). However, both the horizontal spatial sampling and the temporal coverage is poor, and the LIDAR has to be located right above the volcano which is not often the case.

During recent years different empiric relationships have been used to estimate the source term for ash (Wilson et al., 1980/Wilson and Walker, 1987; Sparks et al., 1997; Mastin et al., 2009a; Dacre et al., 2011). Each formula requires the plume heights as input. This might be taken from observations from RADAR or LIDAR as described above, or might need to be guessed. Some formulas also need an estimate of the density of the emitted material.

Mastin et al. (2009a) pointed out an empirical relationship between plume height (H) and mass eruption rate (MER) based on published observation data on plume height, erupted volume or mass and duration for a few dozen well documented volcanic eruptions:

$$\mathrm{MER} = \left(\frac{\mathrm{H}}{\mathrm{a}}\right)^{1/\mathrm{b}} \times \rho \quad (2.10)$$

Here a and b are constants and ρ is the density of ash particles (typically 700 to 3200 kg/m^3). The plume height, H is defined as “the elevation at which most ash spreads laterally from the plume”. This could generally be set as equal to the height of the center of the umbrella cloud. This height is usually lower than the plume height top (see figure 2.9) which is the one estimated from most ground-based and airborne instruments. The difference between those two height levels is usually less than a few kilometers for eruptions with eruption rate less than 10^8 kg/s. For larger eruptions, the height difference can be much larger. For example up to 17 km at the Mount Pinatubo (Philippines) eruption (Holasek et. al, 1996).

The above equation shows that the mass eruption rate increases with plume height. However, the relationship is rather simplified and derived using only a limited number of observations particularly for relatively “small” eruptions. The MER in equation 2.10 gives an estimate of emissions of the ash particles spanning the full ash size distribution (see fig. 1.1). But only the smallest particles (< 63 µm), the fine ash, are important for long-range transport, and are taken into account in the long-range transport simulations. To estimate the fine ash fraction is not straight forward. The fraction varies by nearly two orders of magnitude (Mastin et al., 2009a) and is therefore one of the largest uncertainties when it comes to the modelling of long-range dispersion of volcanic ash.

Degruyter & Bonadonna (2012) introduced an equation that accounts for meteorological data as atmospheric temperature, pressure, wind and humidity. They showed that the prediction of their equation falls within a factor of 2 of the one-dimensional model prediction, whereas for example the equation of Mastin et al. (2009a) can deviate by a factor of 10.

Mastin (2007) made a one-dimensional model (PLUMERIA) that can estimate the fluxes of mass and the injection height distribution by using observed plume heights, atmospheric conditions and prescribed properties of the volcano vent as input.

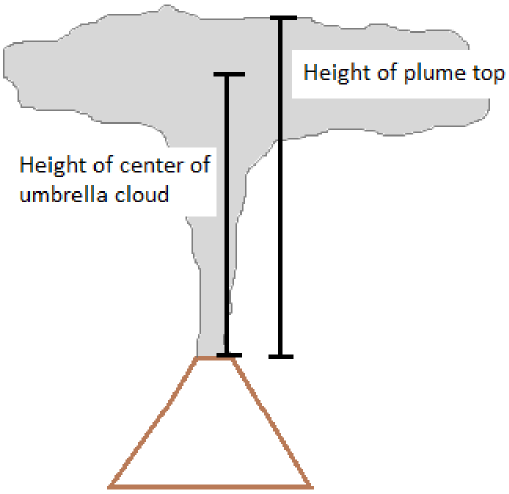

Figure 2.9: *An illustration of the difference between the height of the center of umbrella plume and the plume top height.*

2.7 Grímsvötn volcano

Iceland is one of the world's most geologically unstable areas. Over the past 500 years Iceland's volcanoes have erupted 1/3 of the total global lava output and the country itself has arisen because of volcanic activity on the Mid-Atlantic ridge, where divergent plate movement occurs of about 1-10 cm per year between the North-American and the Eurasian plate (United Kingdom's National Weather Service, Met Office, *www.metoffice.gov.uk*). Frequent earthquakes push magma from deep underground toward the surface, and make volcanic eruptions common. On Iceland there are about 30 active volcanic systems that are split into three volcanic zones; the west (W), the east (E) and the north (N) (see figure 2.10). On average, an eruption occurs every four to five years. Most of the Icelandic magma has low silica content resulting in effusive eruptions (see section 2.1).

Together with Eyjafjallajökull and Hekla, one of the best well-known volcanoes on Iceland is Grímsvötn. The Grímsvötn volcano is located at an elevation of 1725 m above sea level (a.s.l) in the south-eastern (64.42°N, 17.33°W) part of Iceland, 220 km east-northeast of Iceland's capital Reykjavik. The Grímsvötn volcanic chamber is located beneath the Grímsvötn sub glacial lakes underneath the glacier Vatnajökull which is Europe's largest glacier in terms of glacial mass. Grímsvötn is categorized as a mafic volcano with phreatomagmatic eruptions (see section 2.1).

During the past centuries, Grímsvötn has had a frequency of about one eruption per decade with the last major eruptions occurring in 1934, 1983, 1996, 1998, 2004 and 2011.

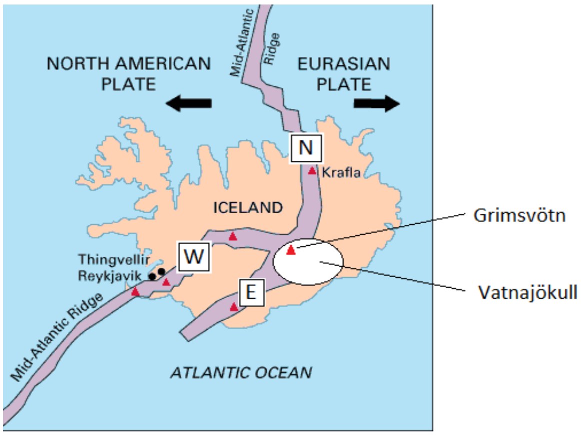

Figure 2.10: *An illustration showing the three different volcanic zones (W=west, E=east and N=north), the Mid-Atlantic ridge and the location of Grímsvötn. Figure adapted from: http://pubs.usgs.gov/gip/dynamic/understanding.html*

At 19:03 UTC on 21 May 2011, this message was sent from the Iceland Meteorological Office (IMO, *http://en.vedur.is*):

Volcanic tremor has been observed in Grímsvötn.
The eruption is expected to start within one hour (~20:00 UTC) and then the melting of the ice will take place and the volcanic plume might reach the surface after 2 to 3 hr (~21:00 to 22:00 UTC).
The plume height might go up to 11 km height.

And 9 minutes later:

The eruption in Mt. Grímsvötn has started, and a moisture plume has been observed.

A GPS-station on the rim of the Grímsvötn caldera had recorded continuous inflation of several centimeters per year since the last eruption of Grímsvötn in 2004. This was interpreted as inflow of magma to a shallow chamber. During the last months before the eruption other precursors such as increased seismicity, tremor, and increased geothermal activity were also reported. The eruption began during the late afternoon of 21 May 2011. Determining an exact starting time for an eruption is generally difficult. The London VAAC assumed the eruption started at 19:15 UTC in their forecast simulations while the Smithsonian Institution's Global Volcanism Program (GVP)[8] reported that the starting time was 16:30 UTC. GVP also estimated the rise speed in the first period of the eruption to be 10-25 m/s (see *http://www.volcano.si.edu/*). Radars observed strong pulsating activity on a timescale of about 20 minutes the first evening with a range in plume height from 3 to 20 km. Based on the

---

[8] The Smithsonian Institution's Global Volcanism Program (GVP) is housed in the Department of Mineral Sciences, part of the National Museum of Natural History, on the National Mall in Washington D.C. They are "devoted to a better understanding of Earth's active volcanoes and their eruptions during the last 10,000 years." Webpage: http://www.volcano.si.edu/

picture in figure 2.6 the troposphere was assumed to be located at 8.9 km. It is clearly visible how the plume spread horizontally when reaching the stable air in the tropopause. A tropopause level at about 8-9 km height also fits well with the observations presented in section 4.4.2.

The reports from the Institute of Earth Sciences at the University of Iceland and the Iceland Meteorological Office during the eruption indicate that the emission strength decreased rapidly and that the plume heights descend to 5-10 km on 22 to 23 May and further below 5 km on 24 May (reports located here: *http://en.vedur.is/earthquakes-and-volcanism/articles/nr/2180*). The eruption was officially declared over at 07:00 UTC on 28 May (Petersen et al., 2012). The eruption has not yet been classified on the VEI scale (see section 2.1), but based on the observed plume heights, it is likely a category VEI 4.

The main air traffic corridor between USA and continental Europe is located between 45-65° N and crosses the North Atlantic (called North Atlantic Tracks [NATs]) (Prata, 2008). If the meridional winds are weak and the zonal winds are northerly, volcanic material will be transported southwards from Iceland and may disrupt the NATs. At lower altitudes (<5 km) the winds tend to be southerly, keeping material from low-altitude eruption plumes away from Europe and main air routes. Some typical trajectories for volcanic clouds originating from Iceland have been documented. Carn et al. (2008) found that a typical transport path is eastwards with northward confinement and circumnavigation of the pole. This transport of volcanic clouds to higher latitudes is of much less threat to aviation. Witham et al. (2007) studied the Grímsvötn 2004 eruption and found rapid eastward and then southward transport.

The reports from the Institute of Earth Sciences at the University of Iceland and the Iceland Meteorological Office during the Grímsvötn May 2011 eruption, indicate that the ash from the lower part of the eruption plume drifted in a southerly direction. A few hours after the eruption began, ash fall covered an area south of the Vatnajökull ice cap, more than 50 km from the eruption site. Some parts of the lower ash also traveled south-west and affected farmers and their livestock. Most of the ash from higher altitudes was reported to drift easterly. Due to the south-easterly transported ash, 900 of total 90,000 planned flights in Europe in the period 23 to 25 May were cancelled, most of them in Scotland, Northern England, Germany and parts of Scandinavia (GVP reports, *http://www.volcano.si.edu/reports/*). Keflavik, the main airport on Iceland, closed on 22 May 2011 and did not open until 36 hours later. There were also short closures of airports in northern UK and northern Germany.

Chapter 3

Methodology

This chapter contains a short description of the dispersion model FLEXPART and how it handles particle transport and removal processes. The chapter continues with an explanation of the inversion method used for estimating the emissions of ash and SO_2 from the Grímsvötn eruption and thereafter a detailed description of the input needed in the inversion model and the specific setup used for the inversions for Grímsvötn. The chapter ends with a section about satellite sensitivities and assumptions on the ash particle size distribution.

3.1 FLEXPART

The numerical model used in this study is the Lagrangian particle dispersion model FLEXPART (Stohl et al., 1998, 2005). The model was first released in 1998 and was originally designed to calculate long-range and mesoscale dispersion of air pollutants from point sources (e.g. a nuclear power plant). Later it evolved into other fields of atmospheric transport such as exchanges between stratosphere and troposphere, global water cycles and emissions from volcanoes. FLEXPART can be run forward to simulate the movement of particles from a given source, or backward to determine possible sources contributing to a given concentration at a receptor. The model is off-line which means that the dynamic variables needed to drive the atmospheric transport are pre-calculated and used as input. In this study, Numerical Weather Prediction (NWP) model data from both the European Centre for Medium-Range Weather Forecasts (ECMWF) and the National Centers for Environmental Prediction (NCEP) Global Forecast System (GFS) are used as input. One advantage of the FLEXPART model is that it is computationally fast. The model has recently been used in several studies of volcanic eruptions (Prata et al., 2007, Stohl et al., 2011, Kristiansen et al., 2012) and it is now being used by a few hundred groups worldwide. FLEXPART's manual and source code are freely available and can be found and downloaded at: *www.flexpart.eu*

3.1.1 Particle transport

There exist two different ways to look at air motion, namely the Eulerian and the Lagrangian. In the Eulerian view, the observer is outside the domain and observes the air parcels fixed in space and affected by the air flows. In the Lagrangian view, the observer follows the air parcels as they move through the atmosphere over time. The paths that the air parcels follow are called trajectories and can be defined by (Stohl, 1998):

$$\frac{\partial \overrightarrow{X}}{\partial t} = \vec{v}\left[\overrightarrow{X}(t)\right] \quad (3.1)$$

where t is time, $\vec{X}$ is the position vector, and $\vec{v}$ is the wind velocity vector.

Aside from the simplest systems, this equation has no analytical solution and must be solved by numerical methods. More precisely, a finite difference approximation of equation (3.1) must be used. All "good" functions can be expanded in terms of a Taylor series. A good function is one where the function itself and all it derivatives exist and are continuous (Røed, 2011). By considering $\vec{X}(t)$ to be a good function, the function itself and all derivatives at a particular point in space, e.g. at $t=t_0$, are known. A Taylor series expansion can then be used to find the values of $\vec{X}(t)$ at all the neighboring points $t_0+\Delta t$. This can be written:

$$\overrightarrow{X}(t_0+\Delta t)=\overrightarrow{X}(t_0)+\frac{\partial\overrightarrow{X}(t_0)}{\partial t}\Delta t+\frac{1}{2}\frac{\partial^2\overrightarrow{X}(t_0)}{\partial t^2}\Delta t^2+.... \quad (3.2)$$

Approximating the solution to a first-order accuracy by removing terms of higher order, gives:

$$\overrightarrow{X}(t_0+\Delta t)\approx\overrightarrow{X}(t_0)+\frac{\partial\overrightarrow{X}(t_0)}{\partial t}\Delta t=\overrightarrow{X}(t_0)+\vec{v}\left(\overrightarrow{X},t_0\right)\Delta t \quad (3.3)$$

Equation 3.3 is called a zero acceleration solution and is computationally cheap. This solution might be sufficient in cases where the integration step is short.

However, a combination of two series can be used to make the approximation more accurate. First finding a Taylor series expansion around $t_0+\Delta t$ evaluated at $t=t_0$:

$$\overrightarrow{X}(t_0)=\overrightarrow{X}(t_0+\Delta t)-\frac{\partial\overrightarrow{X}(t_0+\Delta t)}{\partial t}\Delta t+\frac{1}{2}\frac{\partial^2\overrightarrow{X}(t_0+\Delta t)}{\partial t^2}\Delta t^2-..... \quad (3.4)$$

Combining equation 3.2 and 3.4 leads to:

$$2\overrightarrow{X}(t_0+\Delta t)=2\overrightarrow{X}(t_0)+\Delta t\left[\frac{\partial\overrightarrow{X}(t_0)}{\partial t}+\frac{\partial\overrightarrow{X}(t_0+\Delta t)}{\partial t}\right]+\frac{1}{2}\Delta t^2\left[\frac{\partial^2\overrightarrow{X}(t_0)}{\partial t^2}-\frac{\partial^2\overrightarrow{X}(t_0+\Delta t)}{\partial t^2}\right]+...$$

$$\rightarrow\quad\overrightarrow{X}(t_0+\Delta t)=\overrightarrow{X}(t_0)+\frac{1}{2}\Delta t\left[\frac{\partial\overrightarrow{X}(t_0)}{\partial t}+\frac{\partial\overrightarrow{X}(t_0+\Delta t)}{\partial t}\right]+\frac{1}{4}\Delta t^2\left[\frac{\partial^2\overrightarrow{X}(t_0)}{\partial t^2}-\frac{\partial^2\overrightarrow{X}(t_0+\Delta t)}{\partial t^2}\right]+... \quad (3.5)$$

Setting $t_1=t_0+\Delta t$ finally yields:

$$\overrightarrow{X}(t_1)=\overrightarrow{X}(t_0)+\frac{1}{2}\Delta t\left[\frac{\partial\overrightarrow{X}(t_0)}{\partial t}+\frac{\partial\overrightarrow{X}(t_1)}{\partial t}\right]+\frac{1}{4}\Delta t^2\left[\frac{\partial^2\overrightarrow{X}(t_0)}{\partial t^2}-\frac{\partial^2\overrightarrow{X}(t_1)}{\partial t^2}\right]+... \quad (3.6)$$

Keeping only the two first terms on the right hand side, the solution is called "the constant acceleration solution". By keeping all three terms, it is called the "variable acceleration method". By including terms of higher order, the accuracy of the solution increases but this is at the cost of increased computer time and memory.

FLEXPART generally uses the zero acceleration solution, but has from version 5.0 and on been improved by using one iteration of the constant acceleration solution whenever it is possible.

3.1.2 Removal processes

The concentration of a given species in the atmosphere can be illustrated with a box model as shown in figure 3.1.

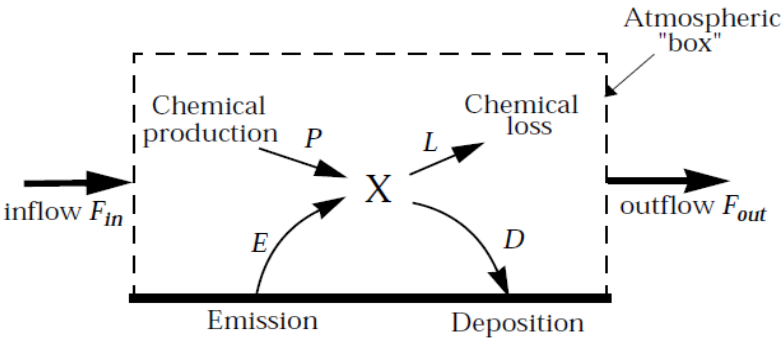

Figure 3.1: *An illustration of the box model. Taken from Jacob (1999).*

In a Lagrangian field of view, the inflow and outflow are equal to zero, so the mass balance equation can be written:

$$\frac{dm}{dt} = \sum \text{sorces} - \sum \text{sinks} = E + P - L - D \quad (3.7)$$

Specifying for SO_2 and ash further gives:

$$For\ SO_2 : \frac{d(SO_2)}{dt} = E + P - L - D \quad (3.8)$$

$$For\ ash : \frac{d(ash)}{dt} = E - D \quad \text{(assumed no chemical production or loss)} \quad (3.9)$$

As an example, the development of ash mass during transport is shown in figure 3.2. It is clearly seen that as the deposition (both wet and dry) increases, the mass of ash in the atmosphere decreases.

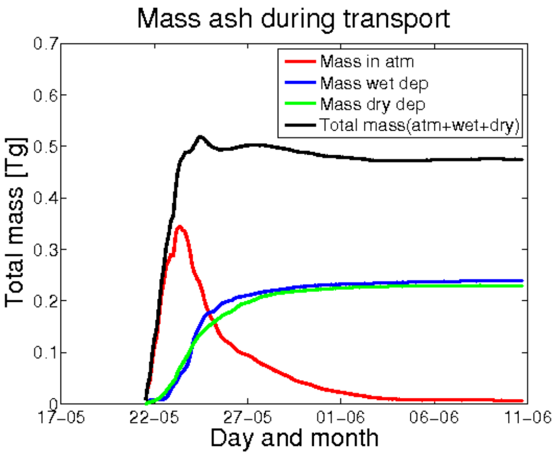

Figure 3.2: *An example of change in atmospheric and deposited ash mass over time during transport (red= total mass in the atmosphere, blue=deposited mass that has been exposed to wet deposition, green=deposited mass that has been exposed to dry deposition, black= total mass both in the atmosphere and deposited). Results are from a FLEXPART simulation.*

The FLEXPART model accounts for certain important physical and chemical properties of a species that are important for the species' removal from atmosphere. Details are found in Stohl et al. (2005) and summarized here.

Dry deposition is caused by impact between the species and surface, diffusion and turbulence, and is described by a dry deposition velocity v_d for each species. For gases (here SO_2), the dry deposition velocity is calculated by the resistance method (Wesely and Hicks, 1977) according to:

$$\left|v_d(z)\right| = \left[r_a(z) + r_b + r_c\right]^{-1}, \quad (3.10)$$

Where r_a is the aerodynamic resistance between height z and the surface, r_b is the sublayer resistance and r_c is the bulk surface resistance. Each of these three resistances is calculated by use of equations given in Stohl et al. (2005).

For ash, the dry deposition additionally includes gravitational settling and the dry deposition velocity is calculated according to

$$v_d(z) = \left[r_a(z) + r_b + r_a(z) r_b v_g\right]^{-1} + v_g, \quad (3.11)$$

where v_g is the gravitational settling velocity. The gravitational settling only leads to dry deposition for particles close to the ground, but it generally brings particles closer to the surface and thereby also enhances the other types of dry deposition.

Monthly averaged OH-concentrations fields are taken from a simulation with an external chemistry model named GEOS-CHEM (Bey et al., 2001). Using these fields, FLEXPART can account for the loss of SO_2 by chemical reaction with the OH-radical as given in equation 2.1-2.3. However, FLEXPART uses monthly averages of OH-concentrations for a given year, so the loss mechanism is somewhat simplified.

Wet deposition is for both gases and particles specified by scavenging coefficients and is separated in in-cloud (Hertel et al., 1995) and below-cloud scavenging (McMahon, 1979). The scavenging coefficients depend on precipitation intensity.

3.2 Inversion method

As previously elaborated, to run the FLEXPART model and simulate the transport of volcanic emissions, the source term, which describes the emissions as a function of height and time, has to be known or estimated. There are several methods to estimate this (see section 2.6). In this study, an inverse modelling technique based on Seibert (2000) is used. The method was adapted to find the vertical distribution of volcanic SO_2 emissions first by Eckhardt et al. (2008), and was extended to ash emissions both as a function of height and time by Stohl et al. (2011).

Inverse modelling is generally used to find a quantity that one cannot directly observe. Ganse (2007) described the inverse modelling problem as:

Observations=SomeFunction(TheUnknown)

In the case of estimating volcanic emissions the *SomeFunction* is the atmospheric transport model. *Observations* are the satellite observations and *TheUnknown* is the source term to be estimated. With information only from an atmospheric transport model and observations from satellite, the problem might be *ill-conditioned*, which means that the problem has many equally good solutions. The problem might also be *under-conditioned* if there are too few observations to solve the problem, but this is seldom the case for volcanic eruptions as the number of satellite observations is normally quite large. However, to make the problem better constrained, additional independent information called *a priori* information is included. This is a pre-defined suggestion for the source term. The goal of the solution (*a posteriori*[9]) is that it is as close as possible to the a priori while the resulting simulated quantities are as close as possible to the observations. This is done by use of a least-squares method that is based on the assumption that ash or SO_2 emitted to different heights above the volcano will move in different directions due to vertical wind shear. The wind might also vary in time, so emissions released at different times might experience different transport.

The inversion method needs three types of input to work: the model sensitivities, M, from a transport model, an a priori source term, x^a, and observations, y^o. A more detailed description of the inputs is given in the next sections. When all this is collected, the inversion can be run to find the unknown a posteriori source term, x. The procedure can be described by the equation:

$$M(x-x^a) \approx y^o - Mx^a \qquad (3.12)$$

And as an abbreviation:

$$M\tilde{x} \approx \tilde{y} \qquad (3.13)$$

By including the observation errors, σ_o (which are the uncertainties of the satellite observations *and* the uncertainties related to atmospheric transport model) and the a priori standard errors, σ_x and assuming that the errors are Gaussian distributed, equation (3.13) can be considered to be a least-square problem where the solution can be obtained by minimizing a cost function J. The uncertainties are normally based on subjective judgments, estimations and testing. There are three contributions to J, namely:

$$J_1 = \left(M\tilde{x} - \tilde{y}\right)^T \mathrm{diag}\left(\sigma_o^{-2}\right)\left(M\tilde{x} - \tilde{y}\right) \qquad (3.14)$$

$$J_2 = \tilde{x}^T \mathrm{diag}\left(\sigma_x^{-2}\right)\tilde{x} \qquad (3.15)$$

$$J_3 = \varepsilon\left(D\tilde{x}\right)^T D\tilde{x} \qquad (3.16)$$

---

[9] The terms “a priori” and “a posteriori” are originally used in philosophy to distinguish between two types of knowledge. A priori knowledge is independent of experience. An example is: “All bodies have extension”. A posteriori knowledge is based on experience. For example: “Some bodies are heavy”.

Equation (3.14) represents the deviation between the modeled and the observed column values of SO_2 or ash weighted with their uncertainty. The emissions with a transport route that matches the observations poorly, will thus be associated with a higher $J_{1.}$ Equation (3.15) is a regularization term including deviations from the a priori emission values weighted with their uncertainty and (3.16) is an additional optional regularization term that requires the solution to be smooth by penalizing “rough” solutions with an additional cost.

The minimizing of the cost function J leads to a linear system of equations that can be solved for the a posteriori source term, $\tilde{x}$ (Menke, 1984):

$$\tilde{x} = \left[\mathrm{diag}\left(\sigma_o^{-2}\right) M^T \tilde{y}\right] \Big/ \left[M^T \mathrm{diag}\left(\sigma_o^{-2}\right) M + \mathrm{diag}\left(\sigma_x^{-2}\right) + \varepsilon D^T D\right] \quad (3.17)$$

The optimized a posteriori source term does not necessarily represent the real emissions, rather the source term that FLEXPART needs to simulate and transport the emissions in best agreement with the satellite observations. Since a large fraction of mass (the large particles) falls out quickly and therefore will not be transported long distances, the a posteriori (and a priori) source term will in all cases contain significant lower amounts of the given species than the real source term for the eruption (including all particle sizes, also the large ones). So the total mass in the a posteriori source term is not equal to the total mass erupted from the volcano.

3.2.1 Input to the inversion method: A priori estimates

For ash, the a priori source term needed as input to the inversion method was first based on the equation from Mastin et al. (2009a) (see section 2.6). The density of the particles was assumed to be 2500kg/m^3. This is close to what was used by the London VAAC in their official forecast simulations during the eruption (Met Office Report 27 May 2011; Met Office Summary May 2011).

To obtain a source term estimate using the Mastin-relationship, the ash plume height is needed as input. During the Grímsvötn eruption, the plume top heights were measured by a fixed position C-band weather radar located 3 km north of the Keflavik airport and 257 km from the Grímsvötn volcano and a mobile X-band weather radar located close to Kirkjubaejarklaustur, about 75 km away from Grímsvötn volcano. The fixed radar started measuring ash plume heights 21 May 19:48 UTC, while the mobile radar did not start the measurements before 22 May 03:27 UTC and did not perform continuous measurements. Because of this, and for simplicity, only the radar heights from the fixed radar are used. They also fit well with the reports from Icelandic Met Office (IMO) during the eruption (reports are located here: *http://en.vedur.is/earthquakes-and-volcanism/articles/nr/2180*). The half-power beam width of this radar is 0.9 degrees and the lowest angle is at 0.5 degrees. This means that above the Grímsvötn volcano the beam width is 5.8 km and the altitude of the lowest beam is 6.2 km. There are no serious blockages even at the lowest angle. The radar gives estimates every fifth minute and a 3-hourly interpolation of these values was used to match the time resolution of the model sensitivities (see figure 3.3). For the times when the plume was below the radar’s minimum detection height, the plume heights were set to 5.5 km a.s.l. The plume heights were also set to 5.5 km a.s.l. for the times when no radar measurements were available, i.e. from 12 UTC on 21 May (the start of the model sensitivities) and until 19:48 UTC. This was done to allow for some early emissions in the a priori which should be constrained by the inversion if not present in the satellite observations.

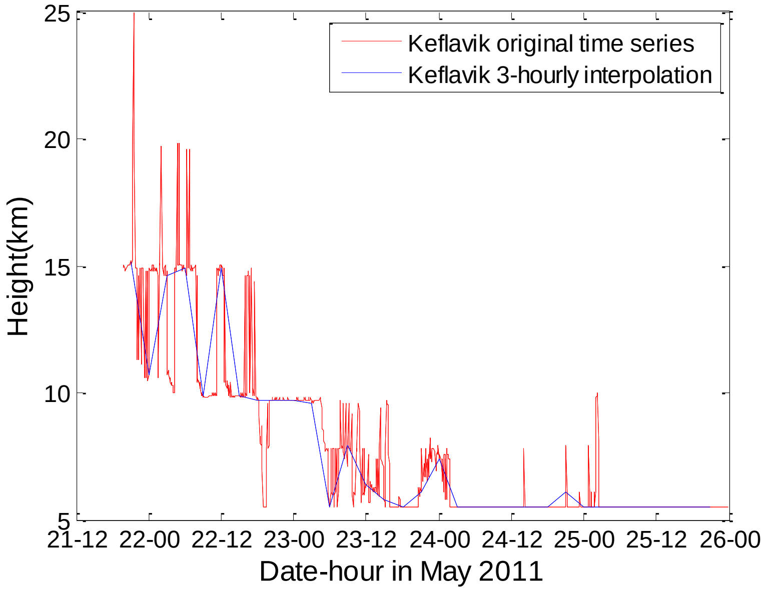

Figure 3.3: *The 5 min observed plume heights and 3-hourly interpolation of the plume height tops measured by the C-band weather radar at Keflavik airport, Iceland. Data taken from Petersen et al. (2012). Available from http://doi.pangaea.de/10.1594/PANGAEA.778390*

The Mastin's relationship gives the total erupted mass, while for the inversion-based source term, estimations are conducted only for the fine ash mass fraction (see introduction). Thus, a fine ash mass fraction must be assumed. Based on the standard emission values of Mastin et al. (2009) the fine ash fraction for Grímsvötn was set to 5 %. This fraction was also used by the London VAAC for the official ash forecast simulations during the eruption. During the later phases of the eruption, the fraction was reduced to 1 % (Met Office, Report 27 May 2011). Using equation 2.10 with the observed radar height, and scaling with a fine ash fraction of 5 % gives a total of about 20 Tg of fine ash released over the whole eruption period. This is much larger than the total amount of fine ash observed by the IASI satellite of about 0.4 Tg (L. Clarisse, personal communication). Thus, the fine ash mass fraction was likely much smaller than 5 %. In order to make the total mass in the a priori closer to the satellite observations, the a priori emissions from the Mastin's relationship were scaled so that the total fine ash mass was 0.4 Tg. The a priori uncertainties were set high (about 100 % of the highest emission values), and constant for all height and all times. This was done to give the inversion method the same opportunity to reduce/increase mass at all heights and for all times.

An appropriate a priori estimate for SO_2 is more difficult to obtain. Since the goal of this study is to investigate whether the method is able to separate the ash and SO_2, it would be preferable to use the same a priori distribution for SO_2 as for ash. The final solutions would thereby be easily comparable. As no radar heights for SO_2 exist, an independent a priori estimate for SO_2 is in any case difficult to find; to base the a priori for SO_2 on the ash a priori might in any case be the best approach. The SO_2 plume tops were kept the same as those for ash, but the total a priori SO_2 mass was scaled so that it was equal to the total amount of SO_2 observed by the IASI satellite, namely 0.4 Tg (Clarisse et al., 2012). This was also in the same order of magnitude as the 0.13Tg and 0.15 Tg observed by the AIRS and OMI instruments, respectively (Fred Prata, personal communication). The a priori uncertainties for SO_2 were set equal to the a priori uncertainties for ash.

3.2.2 Input to the inversion method: Model sensitivities

Source receptor relationships (Seibert and Frank, 2004) also called model sensitivities are used as input to the inversion method. This is in the form of forward dispersion modelling by the use of FLEXPART. Meteorological data (for ECMWF or GFS) is used to drive the model. The ECMWF data has 0.18° x 0.18° horizontal resolution and 91 vertical model levels and the GFS data has 0.5° x 0.5° resolution with 26 pressure levels. The meteorological data contains information on wind, temperature, specific humidity, pressure, snow depth, total cloud cover, dew point, precipitation, sensible heat flux, solar radiation, surface stress, orography, and land-sea mask.

The model simulations are set up as follows:

The height column above the volcano is divided into evenly spaced intervals with one unit mass of ash/SO_2 released in each of the layers (see figure 3.5). It is assumed that the released mass is evenly distributed within the given height interval. The distribution of the height intervals was determined from considering the height of the Grímsvötn volcano and the maximum reported eruption column height (roughly 20 km). The numerical model flattens the real topography. That means that the top of Grímsvötn which in reality is located at 1725 m a.s.l is lower (about 600m) in the model. The first height interval in the inversion method was therefore chosen to start at 500 m above sea level (a.s.l). The height interval step was set to 500 m, and it was assumed that all of the mass was emitted below 23 km.

The eruption period is divided into time intervals of 3 hours. The release of one unit of mass is considered for each of the time intervals (as well as the height intervals – making a 2-D “emission grid”). It is assumed that the released mass is evenly distributed within the time interval.

For SO_2, one species was released in each of the individual height and time intervals. For ash, nine different ash particle sizes with sizes from 4 to 25 µm (4, 6, 8, 10, 12, 14, 16, 18 and 25 µm) were released in each of the individual height and time intervals. Only the ash particle sizes up to 25 µm were considered as the larger particles fall out relatively quickly and larger particles are not observed by satellites. An appropriate ash particle size distribution of the nine particle sizes needs to be considered. An average distribution of two individual ash ground samples taken close to the volcano was used as a basis to determine the ash particle size distribution for the classes considered (see figure 3.4)

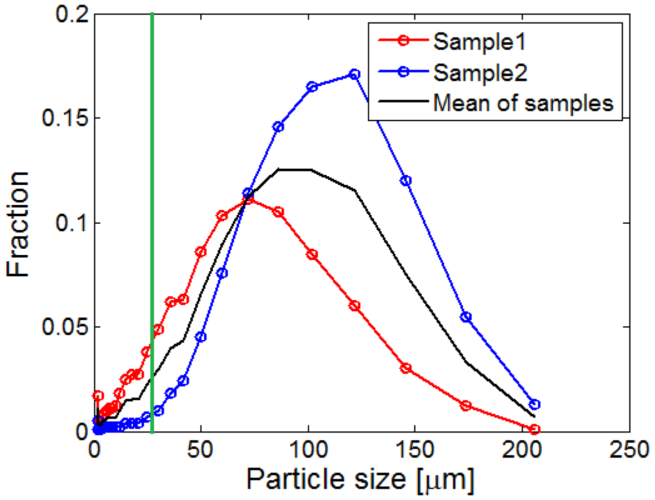

Figure 3.4: *The ground samples used to estimate the ash particle size distribution. Only the sizes smaller than 25µm (indicated by the green vertical line) were used. Data provided by T. Thorsteinsson, University of Iceland.*

Hourly averaged output is given for the release from one particular height level and one particular time step and for each of the species. Hourly averaged SO_2 concentrations (ng/m^3) are output. Vertical resolution in the output for SO_2 is needed for post-processing involving scaling with the satellite height sensitivity. For ash, hourly averaged total column values (ash mass loadings, ng/m^2) are output. No vertical resolution is needed in the ash output as there is no height sensitivity to ash retrievals (see section 3.2.4).

The FLEXPART simulations are split up in 83 different runs (the number of 3-hour intervals in the considered eruption period spanning 21 May 2011 12:00 UTC until 31 May 2011 18:00 UTC). Each FLEXPART simulation considers release from the 45 various height intervals and all relevant species for one particular time step (one 3-hour interval). Each simulation was run forward for 6 days from the start of the individual release. The first simulation (for the first time interval) started 12:00 UTC on 21 May 2011, some hours before the reported starting time of the eruption. The last simulation (time interval) started 18:00 UTC 31 May 2011, about two days after the official end of the eruption. The simulations were extended beyond the reported eruption time period in order to test the inversion for whether the start time and end time of the emissions could be successfully retrieved.

The model gives hourly averaged output for the release from one particular height level and one particular time step and for each of the species (1 for SO_2 and 9 for ash) in a grid on the size 0.25° x 0.25°. A summary of the input to the inversion method is given in table 4.

Parameter	**Value**
Name of transport model	FLEXPART
Meteorological data used	ECMWF and GFS
Number of simulations	83
Start time of first simulation	21 May 2011, 12:00 UTC
Start time of last simulation	31 May 2011, 18:00 UTC
Runtime for each simulation	6 days forward from start of each simulation
Number of height levels	45
Height interval of releases	500 – 23 000 m a.s.l
Height interval step	500 m
Number of particles in each height interval	Ash: 9000 (1000 of each 9 species) SO_2: 8000 (1 species)
Output time step	1 hour
Output grid resolution	0.25° x 0.25°
Grid size	560 x 160

Table 4: *A summary of the setup used as input to the inversion method.*

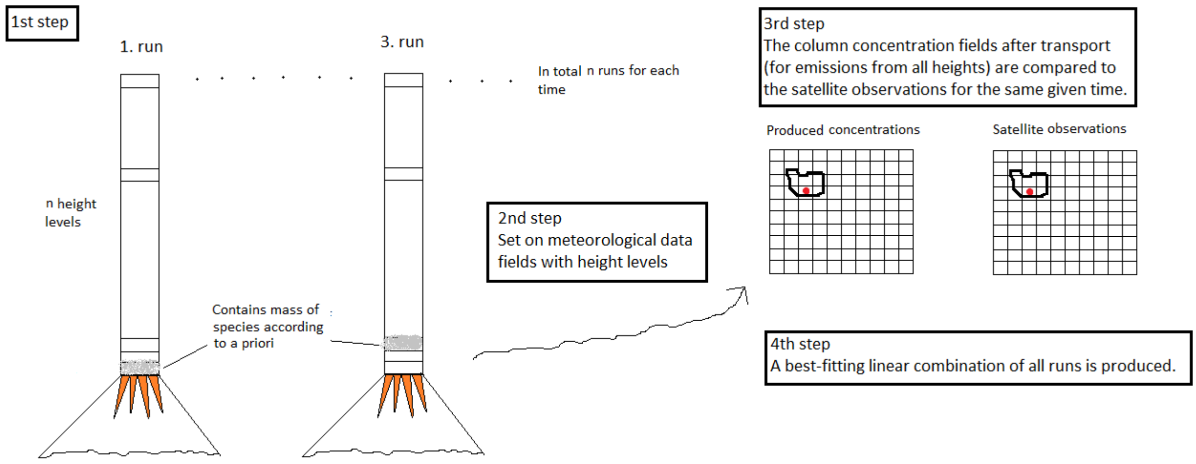

Figure 3.5: *An illustration of the basic principle in the inversion method. Remark that the contributions from J_2 (eq. 3.15) and J_3 (eq. 3.16) from the cost function are left out in the illustration.*

3.2.3 Input to the inversion method: Satellite observations

In this study the inversion method is run with three sets of research-mode satellite data: One set of satellite data for SO_2 (IASI) and two sets of satellite data for ash (IASI and SEVIRI). However, the SEVIRI ash data was from September 2012 made operational, but was not so during the Grímsvötn eruption in 2011.
*(*See *http://www.eumetsat.int/Home/Main/News/ProductServiceNews/821496?l=en)*

The SO_2 columns from IASI measurement were generated by the algorithm of Clarisse et al. (2012). The algorithm calculates SO_2 total columns but needs to make an assumption on the altitude for the SO_2 layer. Several SO_2 products were available assuming 6 different altitudes: 5, 7, 13, 16, 19 and 25 km. Only the measurements using the 13 km height assumption were used. This was based on trial-to-error analysis technique (see section 2.6) that estimates the emissions to most likely be located at this height. However, the total mass when assuming the 6 different altitudes did not differ by more than 10 %. Based on this the uncertainties in the retrievals were set to 20 % or 0.2 times the value of each retrieval. Also included in the retrieval sets are observations from times when the satellite did not cover the volcanic cloud at all, but was still inside the domain of computation. These zero observations values give valuable information about areas where the volcanic cloud is not located and help constrain the solution of the inversion method.

The ash retrievals from the IASI measurements were conducted with a new retrieval algorithm developed by Lieven Clarisse (University of Brussels, ULB). The method consists of i) ash detection using the algorithm presented in Clarisse et al. (2013), ii) simulation of a large number of different IASI spectra with different ash loading, effective radius and height using the forward model presented in Clarisse et al. (2010) and iii) matching of the observed spectra found in (i), with the spectra simulated in (ii) to obtain the mass, radius and height (Lieven Clarisse, personal communication). Every retrieval must assume a certain height of the ash cloud. In this case, 5 km height was assumed. The retrieval errors were set to 1 g/m^2 plus 0.5 times the value of each retrieval

The inversions for ash were also performed with satellite data from the SEVIRI instrument. The SEVIRI instrument is, in contrast to IASI, located on a geostationary satellite. This gives a larger number of satellite observations available in the same time (i.e. no explicit "over pass time"). SEVIRI provides data each 15 minute, and an hourly average was used as input to the inversion method to match the one-hourly averaged output of the model sensitivities. The ash SEVIRI retrievals were based on a reversed split window technique, supported by checks in the other IR channels and two VIS channels (Fred Prata, personal communication). A rather conservative ash cloud detection scheme is used which identifies satellite pixels affected with volcanic ash. Only pixels with a rather high confidence of containing ash are considered. Once the ash pixels are detected, these are passed to the retrieval which estimates the ash mass loading in each of the pixels. Detections and retrievals over land are more difficult than observations over sea due to the different temperature of the land and sea. Since the method is rather conservative, some pixels affected by ash might be undetected and the observed masses are likely to be too low rather than too high. On the other hand, the errors in the observations, which are calculated as a part of the method, are probably lower than for other retrievals which might be affected by false detections (pixels are identified as containing ash which in reality is not the case). Remark that SEVIRI is not able to detect ash when the concentrations are below 0.2 g/m^2 (Fred Prata, personal communication). This might be the reason why the ash cloud moving north suddenly disappears in the retrievals. SEVIRI does not either see anything further north than 70 degrees.

Some examples of the three set of retrievals described are shown in figure 3.6. The upper panel shows the SO_2 moving north-westward, while the middle and the lower panel shows the ash moving mostly south-eastward. Remark that both the IASI and SEVIRI ash retrievals also give some ash moving northward.

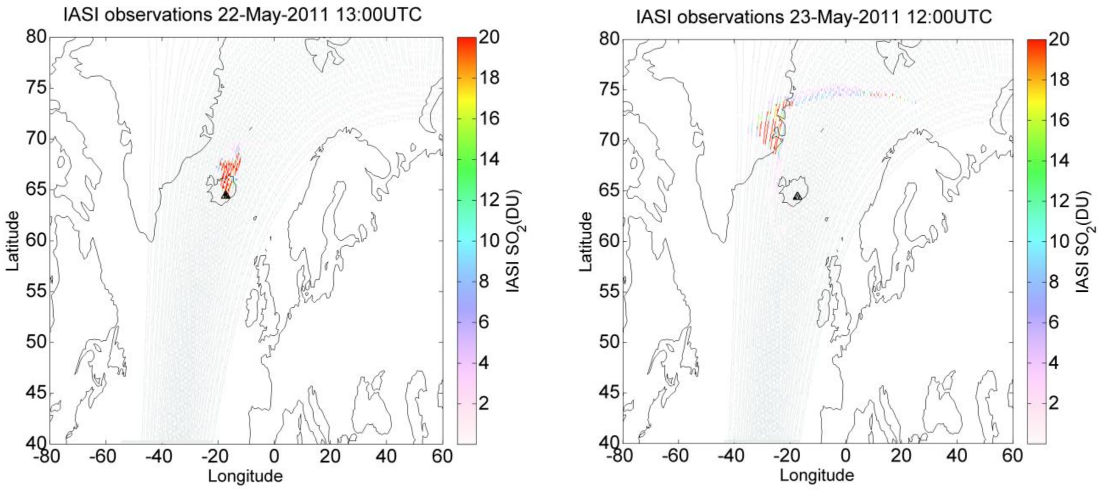

SO$_2$ satellite retrievals from IASI

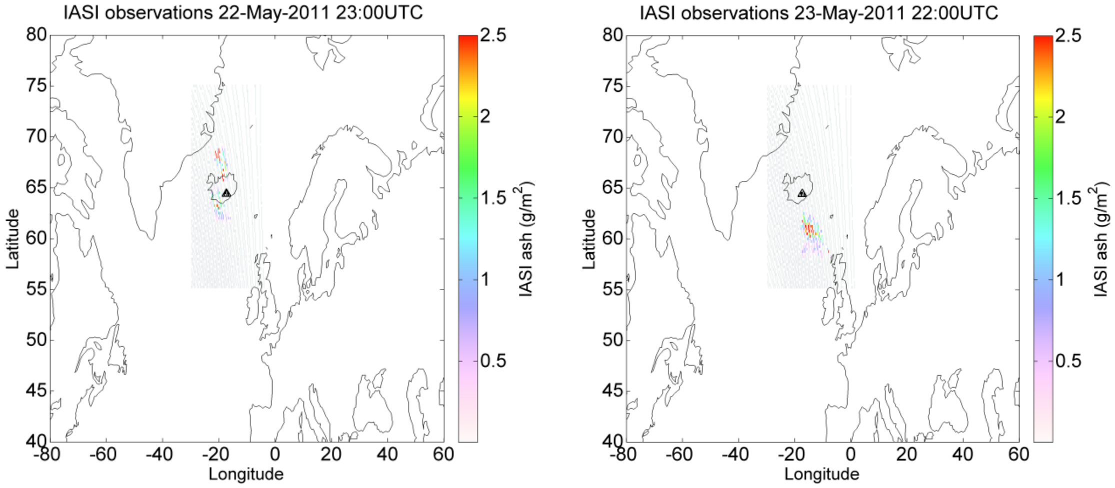

Ash satellite retrievals from IASI

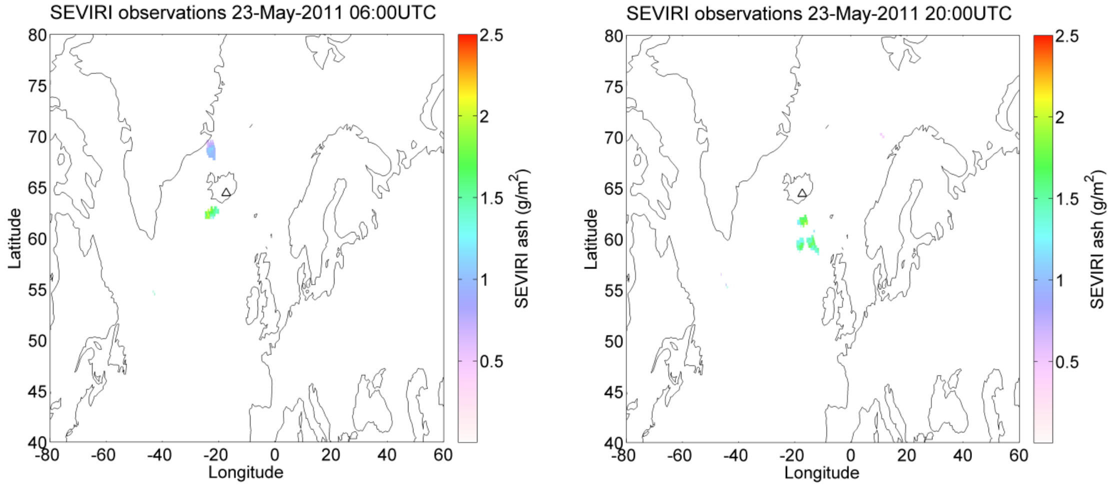

Ash satellite retrievals from SEVIRI

Figure 3.6: *Examples of satellite retrievals for some chosen times in the period from 22-23 May 2011. Upper panel: SO$_2$ retrievals from IASI, middle panel: ash retrievals from IASI, lower panel: ash retrievals from SEVIRI.*

3.2.4 Satellite sensitivity and ash size distribution

Satellite measurements are sensitive only to a limited size range of the ash particles and to the height of the SO_2 cloud. In other words, the satellite instrument can only detect a limited range of ash particle sizes and the retrieved column loadings of the observed SO_2 do not only depend on the total amount in the observing column, but also on the vertical distribution. Hence before comparing the modeled columns to the observed columns in the inversion method, the model output must be scaled with the appropriate sensitivity. There is no height sensitivity to ash retrievals (Fred Prata, personal communication).

3.2.4.1 Height sensitivity for SO_2

The weighting function represents the sensitivity of the radiance contribution from a given height level to the total radiance sensed by the satellite. The weighting function is technically defined as the derivative of the retrieved vertical column with respect to the partial column profile. Each type of instrument used to detect SO_2 has a given height sensitivity. This can be generalized to one sensitivity function for instruments using IR measurements and one for instruments measuring in the UV.

For retrievals in an IR band, the weighting functions depend mainly on the temperature profile of the atmosphere. By neglecting the effects of clouds and other absorbers in the atmosphere, the sensitivity to height can be assessed from the radiative transfer equation given by (Eckhardt et al., 2008)

$$I_v = \int_1^0 B_v[T]d\tau \quad (3.18)$$

where I_v is the radiance emerging at the top of the atmosphere at wave number v, B is the Planck function and τ is the transmittance. By changing variables this can be written

$$I_v = \int_0^\infty B_v[T(z)]\frac{d\tau_v(q,z)}{dz}dz = \int_0^\infty B_v[T(z)]Wdz \quad (3.19)$$

where W is the weighting function.

As one of the absorbing channels used for SO_2 IR retrievals (7.3µm, see section 2.3.1.1) is also sensitive to water vapor, the transmittance of the atmosphere at this wavelength may be regarded as the product of the transmittances of SO_2 and water vapor. The weighting function can then be written

$$W_{SO_2,H_2O} = \tau_{SO_2}\frac{\partial\tau_{H_2O}}{\partial z} + \tau_{H_2O}\frac{\partial\tau_{SO_2}}{\partial z} \quad (3.20)$$

Detection in the IR channels is difficult for SO_2 located below 5 km altitude because the atmospheric content of water vapor is high. Therefore, the sensitivity for SO_2 from IR measurements is close to zero below 5 km (see red curve in figure 3.7).

Figure 3.7 also shows that the effect of altitude is modest in the stratosphere but critical in the troposphere due to a sharp temperature gradient. The thermal contrast between the plume and the backscattered radiation is highest in the tropopause, thus leading to the maximum value of the curve. The IR sensitivity curve can be related to the IASI measurements used in the inversions and to the AIRS measurements used in the validation.

Both the GOME-2 and SCIAMACHY use channels in the UV part of the electromagnetic spectrum to detect SO_2. In contrast to the IR measurements, the UV retrievals have no problems with competition from water vapor. This makes the UV measurements able to observe SO_2 located close to surface. The UV weighting function is given as the blue curve in figure 3.7 and shows that the values are almost constant in the lower stratosphere and upper troposphere before they decrease below about 10 km height. The decrease is mostly due to increased Rayleigh scattering in the troposphere.

An example of the weighting functions applied to the SO_2 emissions from a volcanic eruption is shown in figure 3.8. It is seen that when applying the IR weighting function, all mass below 5 km is gone. A reduction of the masses at lower altitudes is also visible when applying the UV weighting function, but the reduction is much smaller than with the IR weighting function.

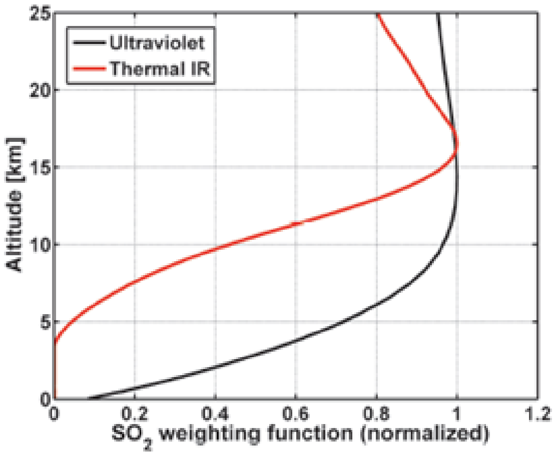

Figure 3.7: *The satellite height sensitivity for SO_2 for instruments using IR-measurements and for instruments using UV-measurements. Figure taken from Theys et al. (2012)*

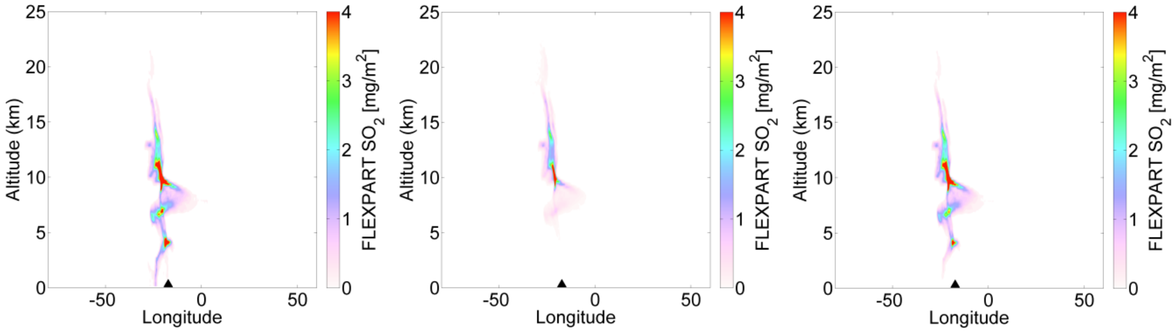

a) No weight **b) IR weight** **c) UV weight**

Figure 3.8: *Plots showing the effect of the IR and UV weighting functions given in figure 3.7 when applied to the simulated SO_2 concentrations emitted by a volcanic eruption.*

3.2.4.2 Size sensitivity for ash

For the volcanic ash, the SEVIRI and IASI satellite instruments can only detect ash particles at the size range about 4-25 µm (Stohl et al., 2011). This lead to the sensitivity function to the left in figure 3.9 which was considered for the nine ash particle sizes used in the simulation, namely 4, 6, 8, 10, 12, 14, 16, 18 and 25 µm. The figure shows maximum sensitivity for an ash particle size around 10 µm and lowest sensitivity to the smallest (=4 µm) and the largest ash particles (=25 µm). Notice that the size range with high sensitivity covers the fine ash that is transported across long distances. The size sensitivity function was used to scale the output from the sensitivity runs before comparing with the satellite observations in the inversion method. The effect of applying the sensitivity function to the a priori ash size distribution is shown to the right in figure 3.9. It is evident that the concentrations in the upper classes, specially 25 µm, are strongly reduced. The sensitivity function is also used when comparing the output from the FLEXPART forward runs to satellite observations. The effect is shown in figure 3.10 where it is seen that the concentrations are somewhat reduced when applying the sensitivity function.

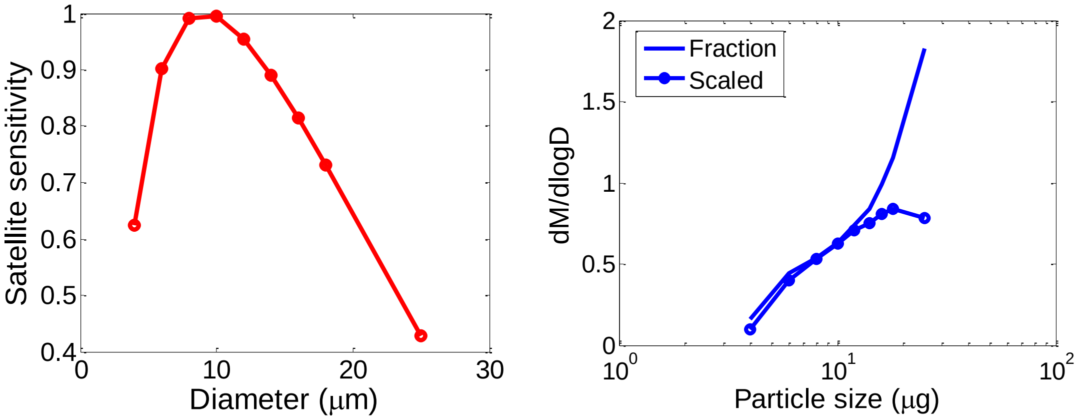

Figure 3.9: *Left: Ash sensitivity function for the SEVIRI and IASI measurements. Taken from Stohl et al. (2011). Right: The fraction from the mean sample in figure 3.4 and the fraction scaled with the satellite ash sensitivity function.*

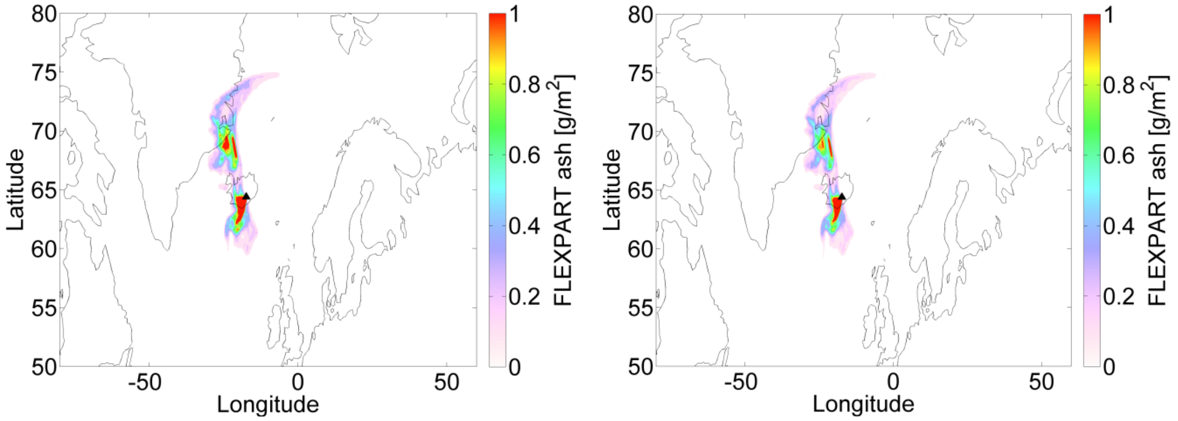

a) No sensitivity **b) Size dist. sensitivity added**

Figure 3.10: *Plots showing the effect of the satellite ash size sensitivity given in figure 3.9 when applied to the ash concentrations from a volcanic eruption.*

Chapter 4

Results and discussion

This chapter begins with a presentation of the inversion results and a consistency check of the results. Thereafter, sensitivity studies for the source term regarding the number of satellite observations used, the starting time and the shape and size of a priori source term are carried out. The chapter continues with an elaboration on the wind conditions during the eruption. Then the transport of the SO_2 and ash masses given in the a posteriori source terms is presented. The results are validated against independent satellite data, surface and LIDAR measurements and the ash results are compared to the ash mass estimations from London VAAC. The chapter ends with a discussion around the different errors and uncertainties that might affect the results.

4.1 Inversion results

The inversion method was run for three cases with the two sets of meteorological data described in section 3.2.2 (ECMWF and GFS), leading to a total of six source term estimations summarized in table 5.

With ECMWF data:	**With GFS data:**
SO_2 with IASI satellite retrievals	SO_2 with IASI satellite retrievals
Ash with IASI satellite retrievals	Ash with IASI satellite retrievals
Ash with SEVIRI satellite retrievals	Ash with SEVIRI satellite retrievals

Table 5: *An overview of the different inversion runs performed in this study.*

The reason for doing the inversions for two types of meteorological data is to reduce the probability of errors in the solution based on errors or deficiencies in the input meteorological data. The source terms that the inversion method produces in the six cases above are given in figure 4.1, 4.2 and 4.3.

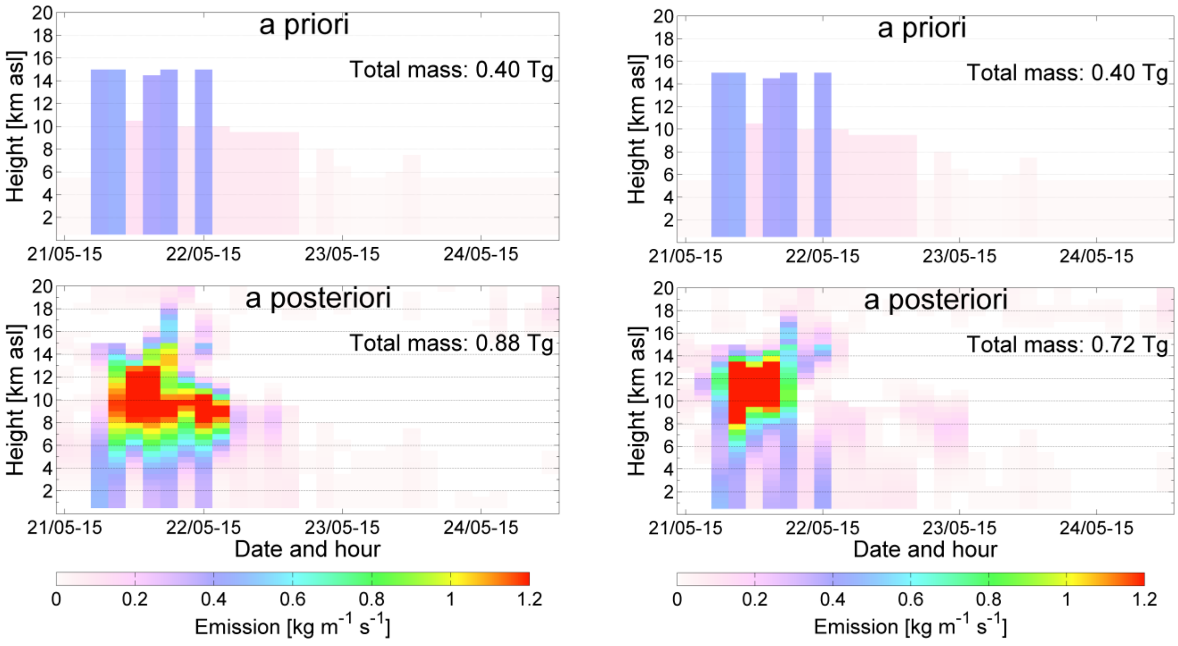

(i) SO$_2$ and ECMWF data **(ii) SO$_2$ and GFS data**

Figure 4.1: *The source terms from the inversion method using the same a priori, IASI SO$_2$ satellite data and two types of meteorological input data, namely ECMWF data(left) and GFS data(right). The source terms are only plotted until 03 UTC on 25 May since no emissions were observed after this time.*

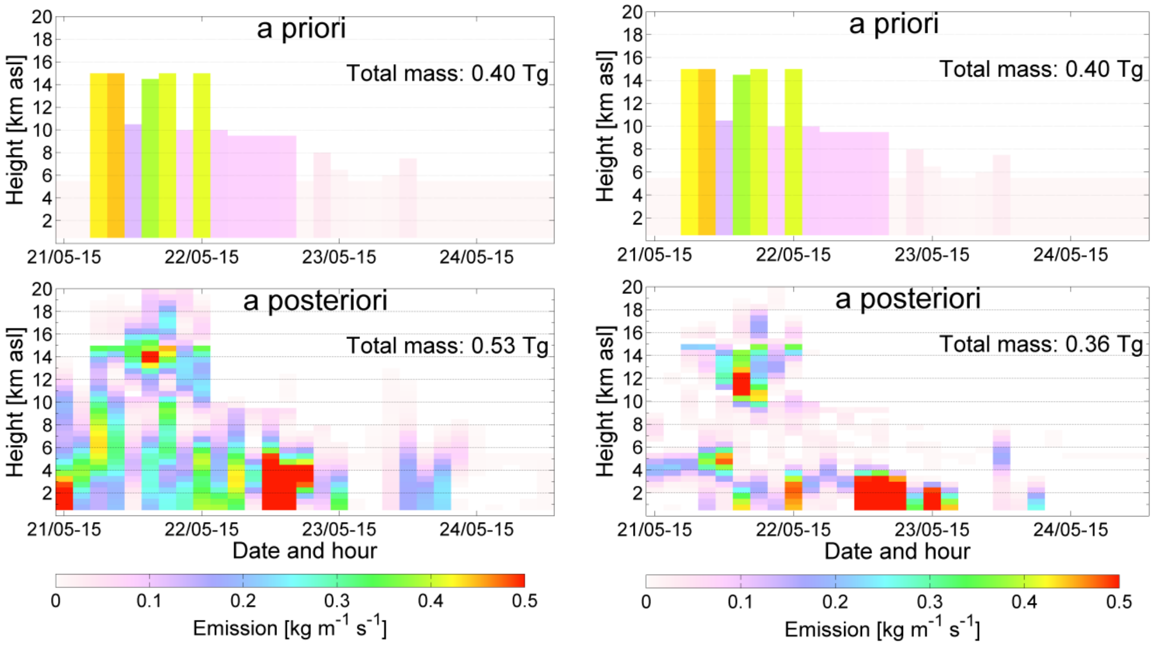

(i) Ash IASI and ECMWF data **(ii) Ash IASI and GFS data**

Figure 4.2: *Same setup as in figure 4.1, but using IASI ash satellite data.*

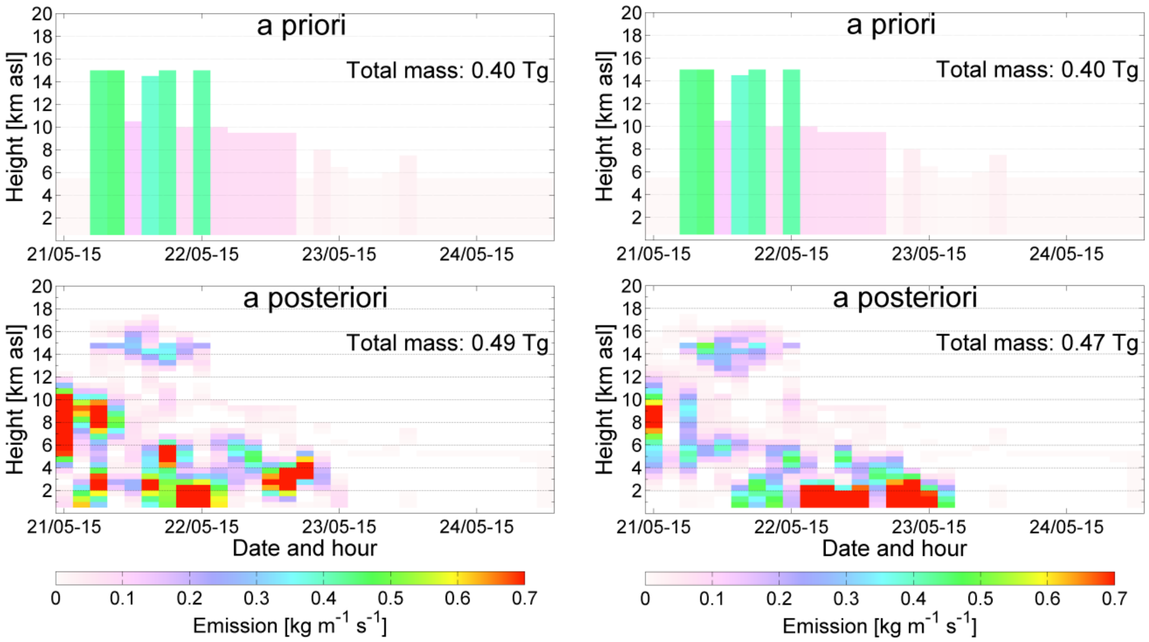

(i) Ash SEVIRI and ECMWF data **(ii) Ash SEVIRI and GFS data**

Figure 4.3: *Same setup as in figure 4.1, but using SEVIRI ash satellite data.*

The SO_2 source terms produced by the inversion method are given in figure 4.1. The SO_2 is emitted to heights from about 8 to 14 km in both cases. The time period of major emissions of SO_2 is from 22 May 00 UTC to 22 May 18 UTC in the ECMWF case and from 22 May 00 UTC to 22 May 09 UTC in the GFS case. The time of maximum SO_2 eruption is thus shorter in the GFS case. The time period of major a posteriori emissions agree roughly to the time periods of major emissions in the apriori. However, in both the ECMWF and the GFS case, the total a posteriori mass is doubled compared to the total a priori ending up with 0.88 Tg in the ECMWF case and 0.72 Tg in the GFS case. The doubling of total mass in the a posteriori source term may be because the whole domain (and thus the whole SO_2 cloud) is not covered with one satellite overpass. Then the total observed SO_2 mass of 0.4 Tg (see section 3.2.1) might be a too low a priori estimate. It may also be that since SO_2 is converted to sulfate aerosols, this loss is not observed by the satellite instrument, and thus the total emitted SO_2 might be higher than the total observed SO_2. This should not, however be critical in the first days of the eruption since the conversion to sulfate aerosols usually takes a few days to give a significant reduction in the SO_2 concentrations (Kristiansen, 2008). The increase in a posteriori mass may also be due to errors in the satellite data or in the meteorological data. Remark that the total mass is somewhat lower when using GFS data. Taking into account that the IASI instrument is not able to detect SO_2 below 5 km height (see section 3.2.4.1), it cannot be concluded that no SO_2 at all was emitted below 5 km height. It can however be concluded that no SO_2 below 5 km height was transported upwards, because such an emission should have been eventually detected by the satellite. An extended discussion of the reliability of the SO_2 source term is given in section 4.4.3.

The ash source terms based on IASI satellite data (figure 4.2) show that most of the ash was emitted ending up at heights below 4-5 km from 12 UTC on 21 May to 12 UTC on 23 May for both the ECMWF and GFS cases. A small maximum around 12 km height from 22 May 00 UTC to 22 May 09 UTC is also seen. This maximum is located around the same height and in the same time period as the maximum SO_2 emissions. The inversion with ECMWF also gives some ash emission below 4 km height around 03 UTC on 24 May. These emissions are also seen in the source term with GFS, though somewhat reduced. The time periods of major a posteriori emissions differ rather largely to the time periods of major emissions in the a priori. Compared to the total a priori emissions (0.4 Tg), the total a posteriori mass increased by approximately 30 % in the ECMWF case (0.53 Tg) and reduced by 10 % in the GFS case (0.36 Tg). The inversion with ECMWF data gives stronger emissions very early in the time period of the simulated eruption, i.e. in the first 3-hourly time period from 12 UTC to 15 UTC on 21 May. The ash emitted in the first time period was about 0.027 Tg or ~5 % of the total 0.53 Tg ash emitted. This 3-hourly time interval is before any reports say the eruption has started (GVP reported the earliest starting time at 16:30 UTC). It seems possible that these early emissions are an inversion artifact likely caused by discrepancies, limitations or errors in the ECMWF meteorological data. This theory can be checked in more detail by looking at the ash results with SEVIRI data.

The ash source terms given by the inversion method using SEVIRI ash data are shown in figure 4.3. Much of the ash emitted ends up at heights below 4 km height, similar to the ash source terms based on IASI data. The maximum emissions at 12 km height from 22 May 00 UTC to 22 May 09 UTC as seen in the IASI ash results are seen also here using SEVIRI data. Compared to the total a priori mass, the total a posteriori mass is increased by about 20 % in both the ECMWF and GFS case. A significant amount of ash (0.054 Tg or ~11% of the total 0.49 Tg) is in the ECMWF case emitted very early, as also seen in the source term based on IASI data. However, now the masses emitted are ending up at higher altitudes i.e. from 4-10 km height. In the SEVIRI case, also the inversion with GFS data retrieves some ash emissions before the reported start of the eruption. It is therefore still unclear how these early emissions come about. It is possible that a combination of errors in the meteorological data, the satellite retrievals and the inversion itself produces these artifacts. These potential errors are discussed in more detail in section 4.6.

However, apart from the early emissions, the main period and heights with ash emissions are quite consistent in all four ash inversions. The fact that the retrieved emissions are quite noisy and that the details vary between the different inversions can probably be traced back to the fact that also the satellite retrievals are quite noisy and details of the ash column loading maps from IASI and SEVIRI are, at times, very different (see fig. 3.6).

All over, figure 4.1, 4.2 and 4.3 show that the main results are not dependent on the meteorological input data as the results are very similar in the three cases ($SO_{2,}$ ash IASI and ash SEVIRI) with both the ECMWF and GFS data. This was expected since Stohl et al. (2011) and Kristiansen et al. (2012) have shown that the inversion is not very sensitive to the model meteorological data input.

Since the inversion results are quite consistent using ECMWF and GFS data, it is chosen to only consider one of them further in the presentation and testing of the results. To decide which of the meteorological data sets that gives the most reliable result for this actual case, is difficult. However, Kristiansen et al. (2012) found that the results with the ECMWF data were shown to provide somewhat better results in the ash simulations of the Eyjafjallajökull volcanic eruption which was close in time (one year before) to the Grímsvötn eruption in 2011 and close in space (located in the same geographical area) to the location of Grímsvötn volcano. Based on this, the results with ECMWF data are chosen to be presented further.

4.2 Consistency check

In this section, so-called consistency checks are performed to see if the inversion algorithm is basically working. In the figures 4.4, 4.5 and 4.6 satellite measurements used in the inversion method are presented together with the FLEXPART forward simulations using the a priori and a posteriori source terms from figure 4.1, 4.2 and 4.3 based on ECMWF meteorological input data. A clear improvement in the agreement between the satellite data and the model data is expected when comparing simulations with a posteriori emissions over the model data using the a priori emissions. However, since many more satellite overpasses are used in the inversion method, and due to errors in simulated transport even with perfect emissions, a perfect match between the satellite observations and the transport of the a posteriori source term is not expected.

Figure 4.4 shows the consistency check for SO_2. The checks are performed at 14 UTC on 23 May and 00 UTC on 25 May. It is generally seen that to obtain a better fit to the satellite observations, the a posteriori masses in nearly the entire SO_2 cloud are increased compared to the a priori. In the check from 23 May, the SO_2 mass on the eastern coast of Greenland is increased in the a posteriori and in closer agreement with the satellite observations. Also the SO_2 mass in the filament transported towards Svalbard is increased to better match the satellite data. However, there seems to be too much mass in the a posteriori in the southern part of the SO_2 cloud closer to the volcano. In the check from 25 May, it is seen that the inversion increases the mass in the SO_2 cloud seen over the Labrador Sea stretching over Alaska, which produces a better match with the satellite data. SO_2 masses around 68 degrees North over Greenland are not observed by the satellite. It is therefore likely that the inversion produces those unobserved masses based on errors in the meteorological data, or from other satellite data than the one shown in figure 4.4. It is likely that it is these unobserved parts of the SO_2 cloud that increases the total SO_2 mass so it does not exactly fit with total mass observed (see section 4.1). Since the mass is also increased in GFS case (though not by that much), it is likely that this is not only due to errors in the meteorological data, but emerges from some other parts of the satellite data.

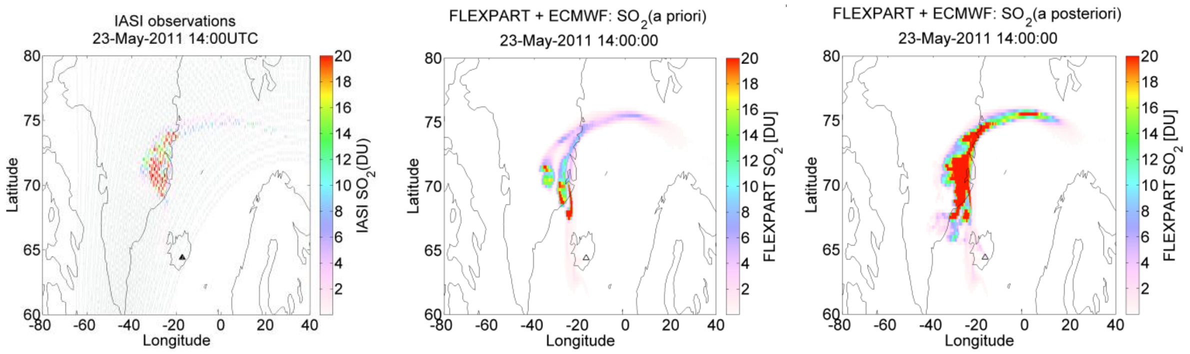

(i) SO_2 IASI **(ii) a priori** **(iii) a posteriori**

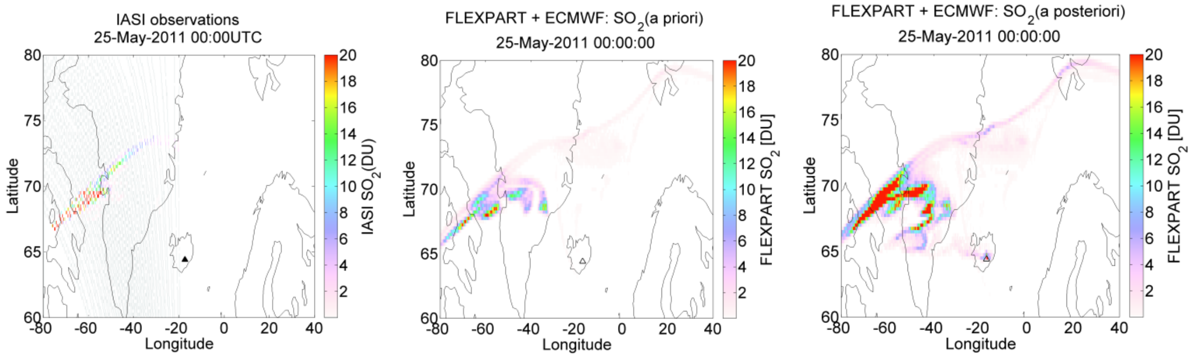

(i) SO_2 IASI **(ii) a priori** **(iii) a posteriori**

Figure 4.4: *Comparison of i) SO2 IASI satellite observations used in the inversion method, ii) the FLEXPART simulations using the SO_2 a priori source term and iii) FLEXPART simulation using the SO_2 a posteriori source term for two times: 23 May 13-14 UTC (upper panel) and 24 May 23 to 25 May 00 UTC (lower panel). The IR weighting function from section 3.2.4.1 is applied both to the a priori and a posteriori FLEXPART data.*

The consistency check of ash with IASI satellite data is shown in figure 4.5. In the upper panel, the observed and modeled ash clouds at 12 UTC on 23 May are illustrated. Here it is clearly seen that the inversion increases the masses in the cloud transported southwards from Iceland in better agreement with the satellite data than for the a priori ash clouds. The ash masses in the cloud moving northwards are decreased in the a posteriori case, which fits with the fact that these satellite data do not show any as moving north. However, some satellite retrievals for other times than the two given in figure 4.5 show some ash moving north (see figure 3.6), but it seems to fall out faster than what is simulated by FLEXPART. In the lower panel, a check for the time 10 UTC on 24 May is performed. Here it is again seen that the inversion increases the (now) east-moving a posteriori cloud moving towards Norway and decreases the cloud over Greenland. It can also be seen that the location of the main part of the east-moving cloud in the a priori simulations is found west of Denmark while it is moved to north of Great Britain in the a posteriori simulation. It looks, however, that the a posteriori ash masses of the main ash cloud in the FLEXPART simulations are a bit too low compared to the IASI satellite observations.

Remark that the masses shown in the source term below 4 km height around 03 UTC on 24 May (see fig. 4.2, left) are seen as a “second” independent cloud still connected to the volcano in the a posteriori plot for 10 UTC on 24 May.

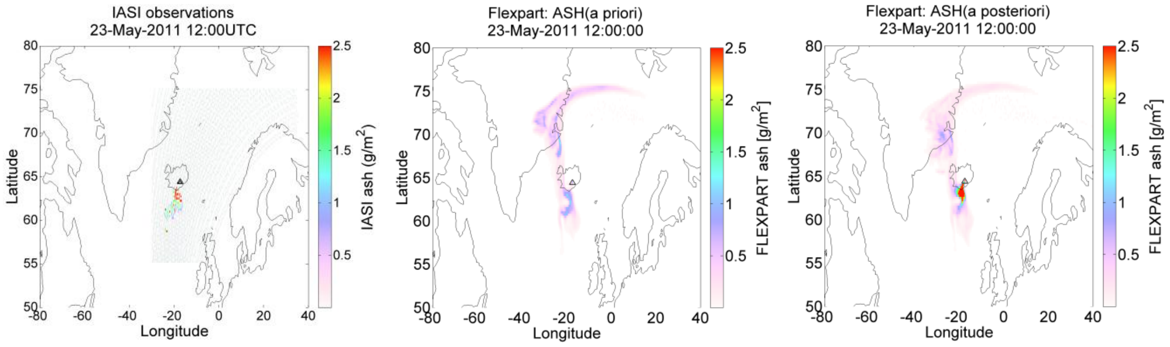

(i) Ash IASI **(ii) a priori** **(iii) a posteriori**

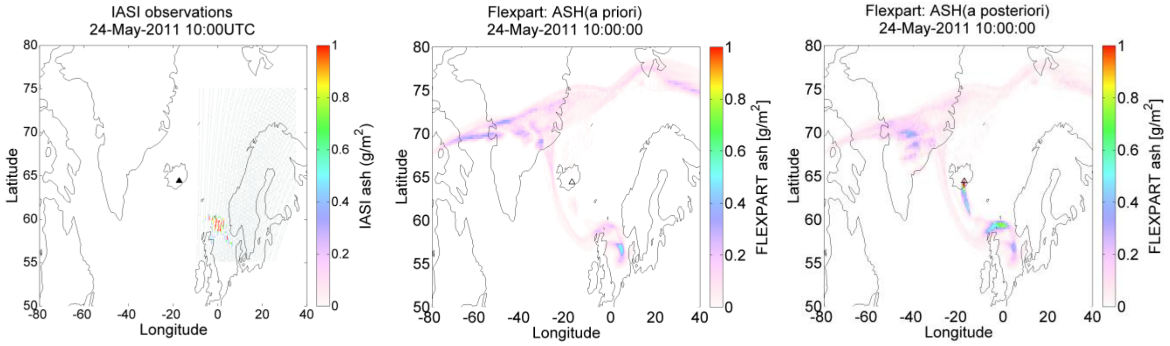

(i) Ash IASI **(ii) a priori** **(iii) a posteriori**

Figure 4.5: *Comparison of i) ash IASI satellite observations used in the inversion method, ii) the FLEXPART simulations using the ash a priori source term and iii) FLEXPART simulation using the a posteriori source term for two times: 23 May 11-12 UTC (upper panel) and 24 May 09-10 UTC (lower panel). The satellite size sensitivity from section 3.2.4.2 is applied both to the a priori and a posteriori FLEXPART ash data.*

The consistency check for ash with SEVIRI satellite data is given in figure 4.6. In the upper panel, the observed and modeled ash clouds at 03 UTC on 23 May are shown. The simulated a posteriori ash clouds are generally in closer agreement with the SEVIRI satellite data than the simulated a priori ash clouds. As in the IASI case the a posteriori mass in the ash cloud on the southern side of Iceland is increased compared to the a priori case, while the mass in the cloud heading north is decreased. In the lower panel, a check for the time 22 UTC on 23 May is illustrated. Like in the IASI case, the inversion method increases the (now) east moving ash cloud towards Norway, in closer agreement with the SEVIRI satellite data, and decreases the ash cloud over Greenland (not observed by SEVIRI). However, as in the IASI ash case, it seems like the inversion and the a posteriori FLEXPART simulation still under-estimate the ash masses for the ash cloud transported eastward, compared to the SEVIRI satellite data.

Since the ash masses seem to be of the same size as the satellite observations near the volcano, but too low after some time of transport, it is likely that estimates of removal processes in the model simulations are somewhat biased. Too high assumed deposition in the model will, for example, reduce the mass so it does not fit with satellite observations.

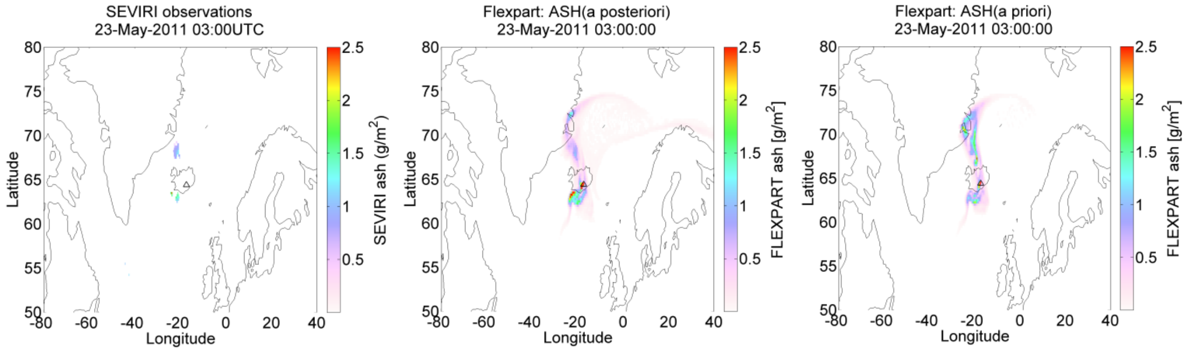

(i) Ash SEVIRI **(ii) a priori** **(iii) a posteriori**

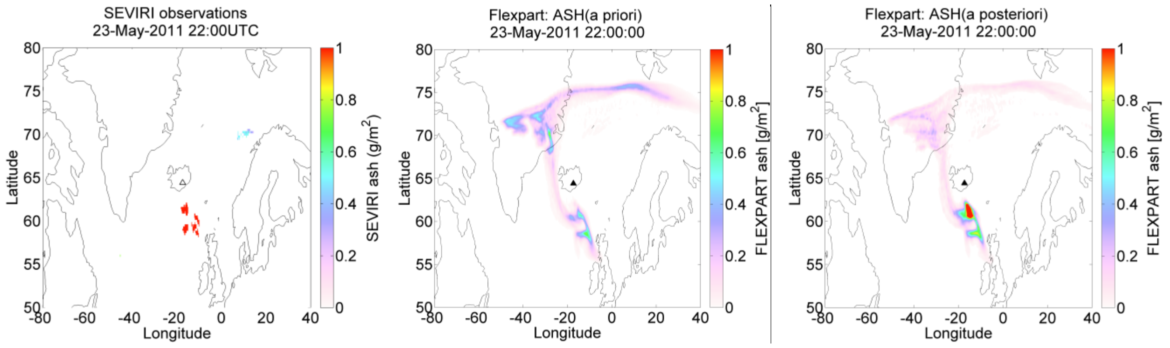

(i) Ash SEVIRI **(ii) a priori** **(iii) a posteriori**

Figure 4.6: *Comparison of i) ash SEVIRI satellite observations used in the inversion method, ii) the FLEXPART simulations using the ash a priori source term and iii) FLEXPART simulation using the a posteriori source term for two times: 23 May 02-03 UTC (upper panel) and 23 May 21-22 UTC (lower panel). The satellite size sensitivity from section 3.2.4.2 is applied to both the a priori and a posteriori FLEXPART ash data.*

Overall, the a posteriori simulations produce SO_2 and ash clouds in better agreement with the satellite data than the simulations using the a priori source terms. This illustrates that the inversion is doing what is expected.

4.3 Sensitivity tests of the source term

The inversion results might be sensitive to factors such as

- The number of satellite observations used.
- The starting time of the inversion.
-The shape and magnitude of the a priori.

Some tests checking the sensitivity to these factors are given in this section. The tests are conducted with the ECMWF meteorological data.

4.3.1 Sensitivity to the number of satellite observations

If the inversion method is to be used as a part of an operational setting, i.e. providing estimates of the source term and thereby forecast the transport patterns during an ongoing eruption, the method has to provide appropriate results when using a limited number of satellite observations, i.e. only from the first day(s) after the eruption. An overpass cannot constrain emissions of the days after the actual overpass, so for eruptions lasting for a longer time period, data from new satellite overpasses has to be continuously added. In this operational setting, operational measurements have to be used. One disadvantage with operational measurements is that they normally have larger errors than the research-mode retrievals. It is likely to think that it would be preferable to use measurements from an instrument on a geostationary satellite since this can give more information faster (every 15th minute from, for example, the SEVIRI instrument).

For less time critical applications, such as determining the injection height and magnitude of emissions for climate purposes, later satellite data can be used. However, using satellite data for too long after the eruption should always be conducted with caution since this can yield errors from removal processes (Kristiansen , 2008).

Tests are here conducted on the research-mode satellite retrievals used in this study. The tests are conducted for the three cases:

With ECMWF data:
SO_2 with IASI satellite retrievals
Ash with IASI satellite retrievals
Ash with SEVIRI satellite retrievals

Table 6: *The cases that the sensitivity tests in this section are performed on (selection of table 5).*

4.3.1.1 SO_2 IASI

The first time when the IASI satellite instrument captures the SO_2 plume from Grímsvötn is on 22 May 13 UTC, i.e. less than a day after the start of the eruption. The satellite observations and source term when using only this single overpass is given in figure 4.7 (bottom, left). The source term shows an emission peak around 09 UTC on 22 May when the emissions reach 18 km height. This peak is not seen in the source term using all the satellite over passes used (bottom, right). However, except for this high emission, the source term from the inversion method using only the single overpass, is not very different from the source term using satellite observations for the whole period. Remark that the a priori emissions are not changed after 22 May 13 UTC since the inversion cannot optimize the emissions for the times after the satellite overpass. These results are in good agreement with what is found in earlier studies (Kristiansen 2008) when testing the sensitivity to the amount of satellite data used in the inversion.

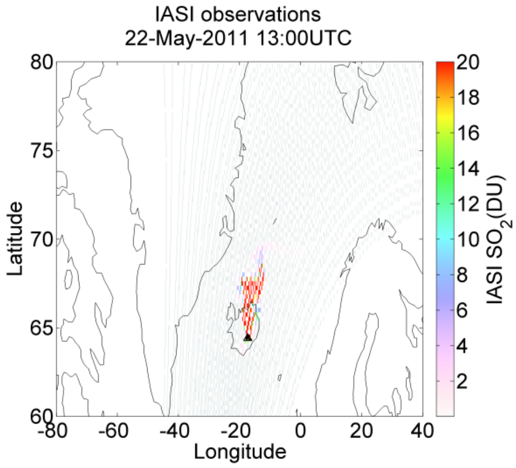

IASI SO_2

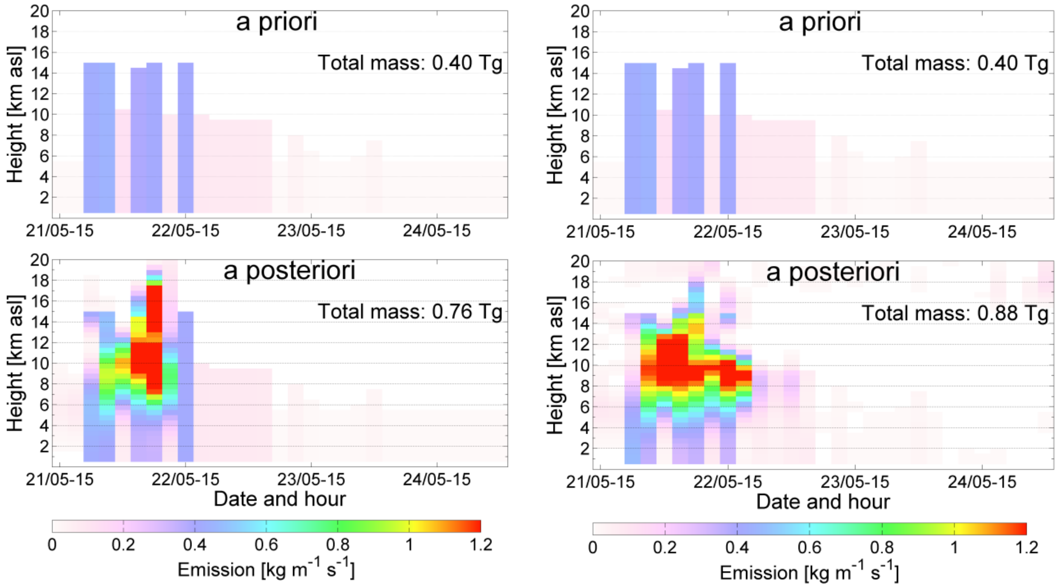

One overpass **All overpasses**

Figure 4.7: *One IASI overpass (22 May 13 UTC) of the SO_2 cloud (top), and the resulting SO_2 source term from the inversion using only this overpass (bottom left) (mark that a posteriori emissions are calculated only until the single overpass time), compared to the SO_2 source term using all satellite overpasses from the whole eruption period (bottom right).*

4.3.1.2 Ash IASI

The first overpass where IASI observes ash is the same as the first observations of SO_2, namely 22 May 13 UTC (figure 4.8, top). Using only this overpass gives the source term shown in figure 4.8 (bottom left). This source term is quite similar to the one when using all satellite observations (figure 4.8, bottom right). The a priori emissions are again not changed after 22 May 13 UTC since this is after the time of the used satellite overpass. Another visible feature is that the early emissions in the source term using all satellite observations are not that strong in the source term only using this one overpass. Thus, the significant early emissions in the source term with all observations used are likely to be produced by errors in the satellite retrievals or meteorological data for the time after 22 May 13 UTC.

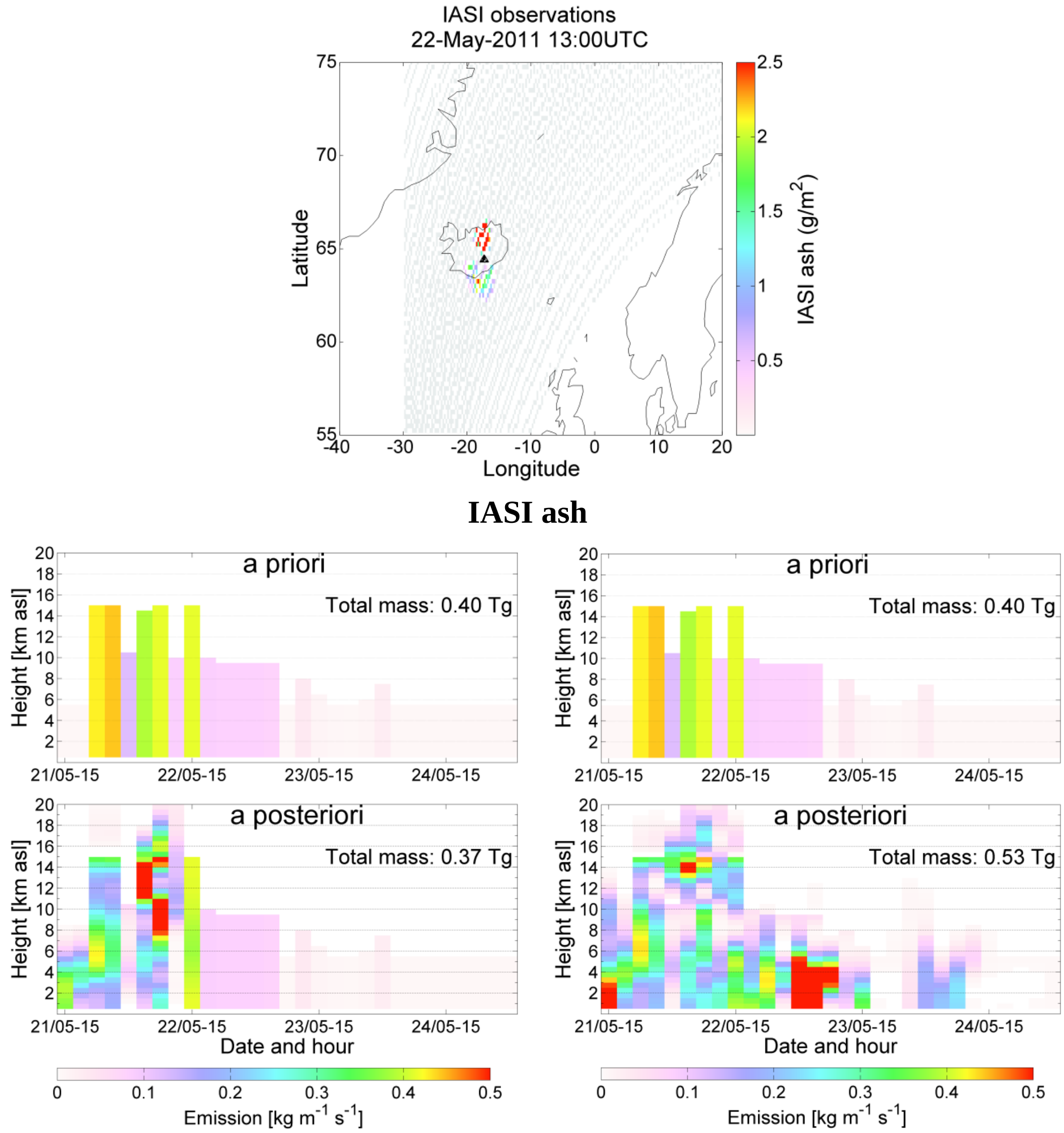

One overpass **All overpasses**

Figure 4.8: *One IASI overpass (22 May 13 UTC) of the ash cloud (top), and the resulting ash source term from the inversion using only this overpass (bottom left) (mark that a posteriori emissions are calculated only until the single overpass time), compared to the ash source term using all satellite overpasses from the whole eruption period (bottom right).*

4.3.1.3 Ash SEVIRI

The SEVIRI instrument is, in contrast to the IASI instrument, located on a geostationary satellite. This yields a larger number of satellite observations available per time (i.e. no explicit "over pass time"). The first time where the whole ash plume is clearly visible from SEVIRI is on 22 May 17 UTC. Using only satellite data up to this time gives a number of about 45 000 observations used which is about 35 times larger than the number of observations used in the IASI inversion with the one overpass. The resulting source term with these ~45 000 observations used is shown in figure 4.9 (bottom left). Compared to the source term with all satellite observations used (bottom right), the emissions at higher altitudes are the same while the emissions at lower altitude are completely gone. Again, remark that the a priori emissions are not changed after 22 May 17 UTC since the inversion cannot optimize the emissions for the times after the last overpass used in the inversion. Looking at the observations from the last satellite overpass used (figure 4.9, upper panel) makes it clear that the south-going ash plume has not yet been detected. This is due to the conservative detection method which seems to not detect any ash over land. So it is likely that there is some ash moving southward over land at this time, even though it is not yet retrieved. This is the reason for the lower altitude emissions missing in the source term using only the limited number of satellite observations. Another clearly seen feature is that, as also found in the IASI ash case (section 4.3.1.2), the early emissions are reduced. This might also be ash moving south and therefore not detected yet, or it might show that the early emissions are not real and are due to errors in later satellite or meteorological data.

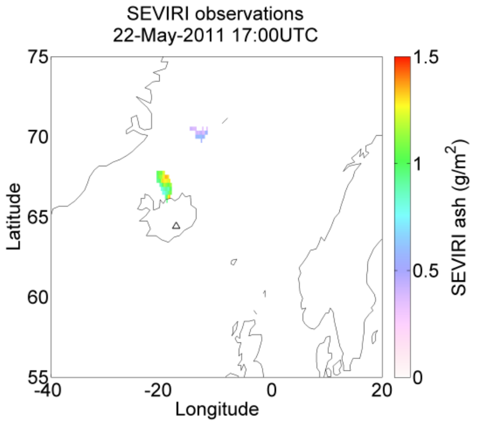

SEVIRI ash

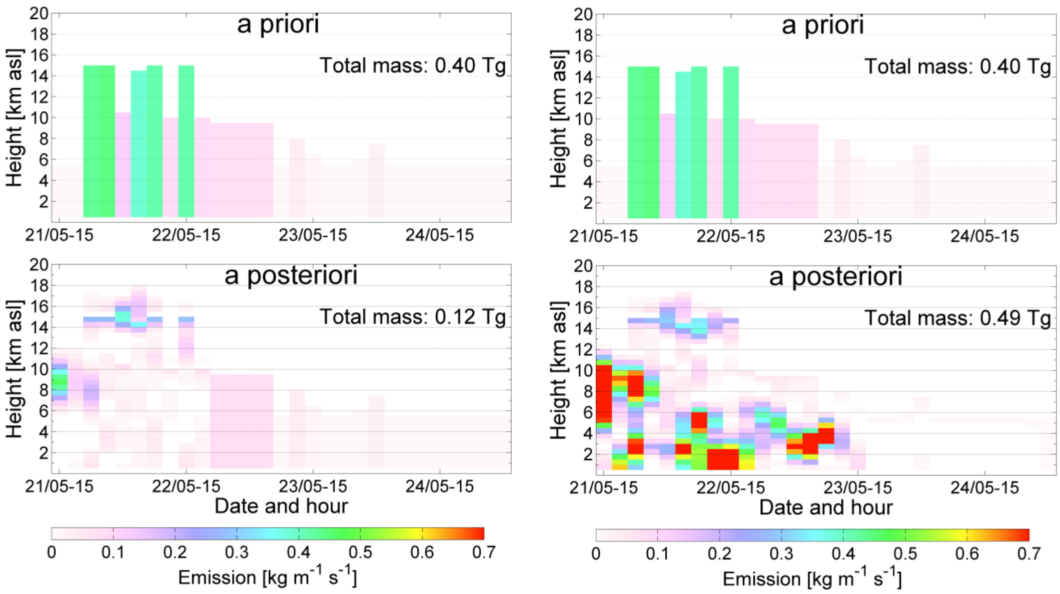

One overpass **All overpasses**

Figure 4.9: *SEVIRI ash observations on 22 May 17 UTC (top) and the ash source term from the inversion method using only the SEVIRI observations from 22 May 00 UTC to 22 May 17 UTC (bottom left) (mark that a posteriori emissions are calculated only until the last observation time used in the inversion). The source term using all satellite observations from the whole eruption period is also shown for comparison (bottom right). Note that SEVIRI does not observe above 70 degrees north, thus the observed ash cloud around 71 degrees north is most likely an artifact.*

4.3.2 Sensitivity to the starting time

The results shown until now were all produced by inversions with starting time 21 May 12 UTC. However, the London VAAC, for example, reported that the eruption started at 19:15 UTC. The simulations were started somewhat earlier than the reported start time for the eruption to see if the inversion could successfully estimate the starting time of the emissions. Also there might have been emissions earlier than the reported start time of the eruption. Adding degrees of freedom through the use of earlier time periods will always reduce the error in the comparison between the model results and the observations since it gives more flexibility for the inversion to adjust. If there were no emissions at these earlier times, the inversion would simply reduce the a priori emissions for these time periods. However, this requires that there are no errors in the meteorological or satellite data. As shown in section 4.1, the inversion puts significant amounts of mass in the first time interval (from 12-15 UTC on 21 May). If assumed that this is all artifacts, the choice of adding the early time interval may add more “unreal” mass and increase the error in the total mass in the source term. Regardless of whether this is artifacts or not, it would be interesting to see if starting the inversions earlier than the reported eruption start increases the total mass or if it only smoothes out the early emissions over an extended time period.

Displayed in the left column of figure 4.10 are the source terms produced with the original setup of the inversions, i.e. with starting time of 12 UTC (the source term (i) in figure 4.1, 4.2 and 4.3) for SO_2 (upper panel), IASI ash (middle panel) and SEVIRI ash (lower panel). The source terms in the right column are the corresponding source terms resulting from the inversions with starting time six hours later, namely 18 UTC, which is closer to the reported start time of the eruption.

As already seen, the inversion does not produce any significant amounts of SO_2 emissions before around midnight on 22 May. The total SO_2 a posteriori mass in the source term with starting time 12 and 18 UTC is more or less the same. Therefore it would not have been necessary to start the SO_2 inversions as early as 12 UTC. On the other hand there are no disadvantages by doing this, and it demonstrates that the inversion in this case successfully can estimate the starting time of the SO_2 emissions.

When it comes to ash, as already elaborated, the inversion produces some ash in the first time periods with starting time 12 UTC, especially for the IASI ash case. With starting time 18 UTC, the total a posteriori mass in the IASI case decreases with about 6 % (from 0.53 to 0.50 Tg). Thus, by starting at 12 UTC, the inversion adds 6 % extra mass compared to starting at 18 UTC. For the SEVIRI case, the total a posteriori mass decreases with 12 % (from 0.49 Tg to 0.43 Tg) when starting at 18 UTC compared to 12 UTC. This extra mass added in both cases by using starting time 12:00 UTC will increase the transported mass and thereby change the agreement between the satellite data and the a posteriori simulations. It is therefore shown that in some cases (here for ash) the start of the eruption is an important a priori constraint that needs to be carefully considered.

Starting time 12:00 UTC **Starting time 18:00 UTC**

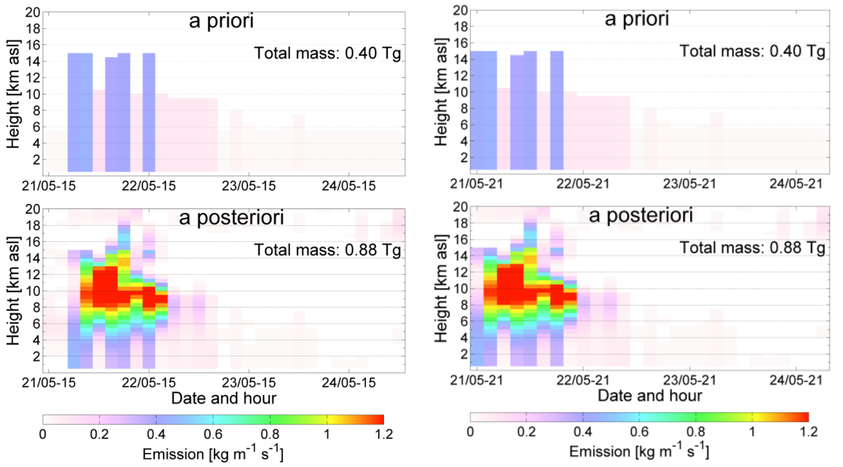

SO₂

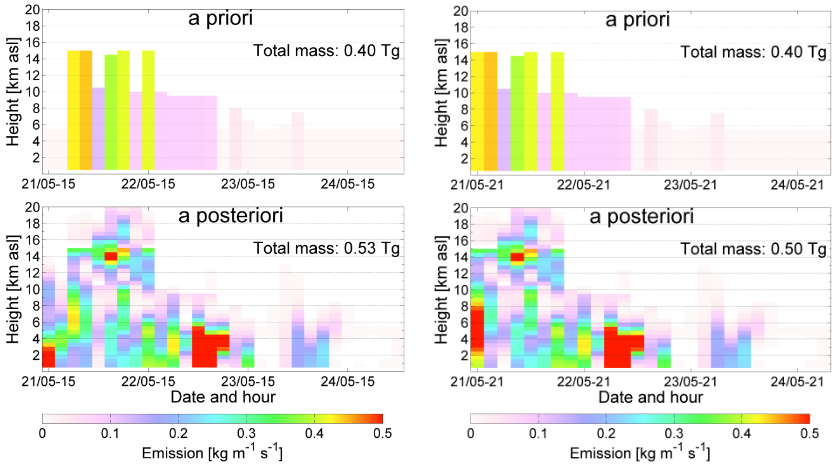

Ash IASI

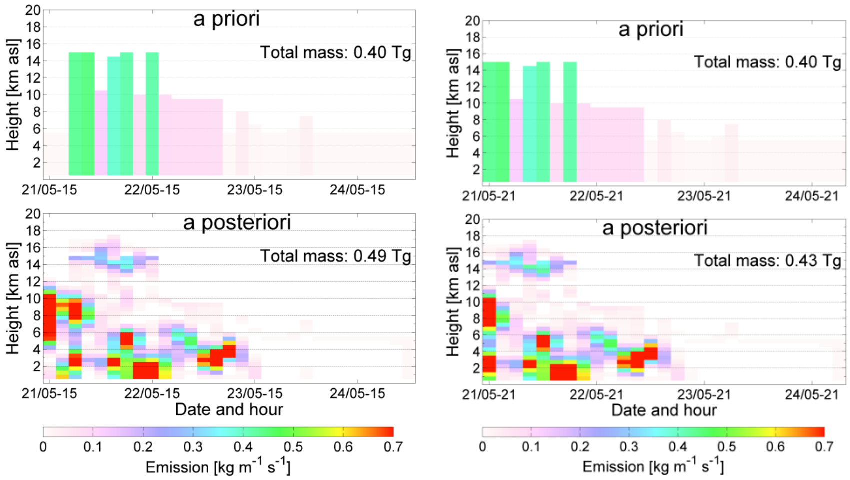

Ash SEVIRI

Figure 4.10: *Given in the left column are the source terms produced with starting time 12 UTC for SO_2 (upper panel), IASI ash (middle panel) and SEVIRI ash (lower panel). The source terms in the right column are the corresponding source terms resulting from the inversion runs with starting time 6 hours later than in the final setup, namely 18 UTC, and closer to the reported start time of the eruption.*

4.3.3 Sensitivity to the shape and size of a priori source term

The a priori emissions are based on plume top heights observed by radar (see section 3.2.1). This was used both for SO_2 and ash. While the plume top is normally relatively well observed, the magnitude and the vertical distribution of the emissions are highly uncertain. Furthermore, on 24 May (about 2 days after the start of the eruption), the plume was not visible on radar most of the night and in the early morning due to weather conditions (reports from Icelandic Meteorological Office [IMO] and Institute of Earth Sciences, University of Iceland, found at: *http://en.vedur.is*). The estimated height for these periods was below 5 km since this was the height of the cloud cover and no material was detected above it. The same problem occurred on 25 May. The plume top height is therefore quite uncertain on these days.
It is therefore interesting to check how sensitive the inversion results are to different a priori source terms. Below, the inversion runs have been performed for two other types of a priori, namely:

- An a priori with only zero values.
- A uniformly distributed a priori in both height (up to 20 km) and time (until the time of no more reported observed emissions, i.e. 25 May 03:00 UTC, *http://en.vedur.is*).

The source terms are given to the left (zero a priori) and middle column (uniform a priori) of figure 4.11. The source terms produced with the standard a priori (the one based on plume heights observed by radar, presented to the left in figure 4.1, 4.2 and 4.3) are re-plotted in the right column of figure 4.11 to compare.

Zero a priori **Uniform a priori** **A priori based on radar heights**

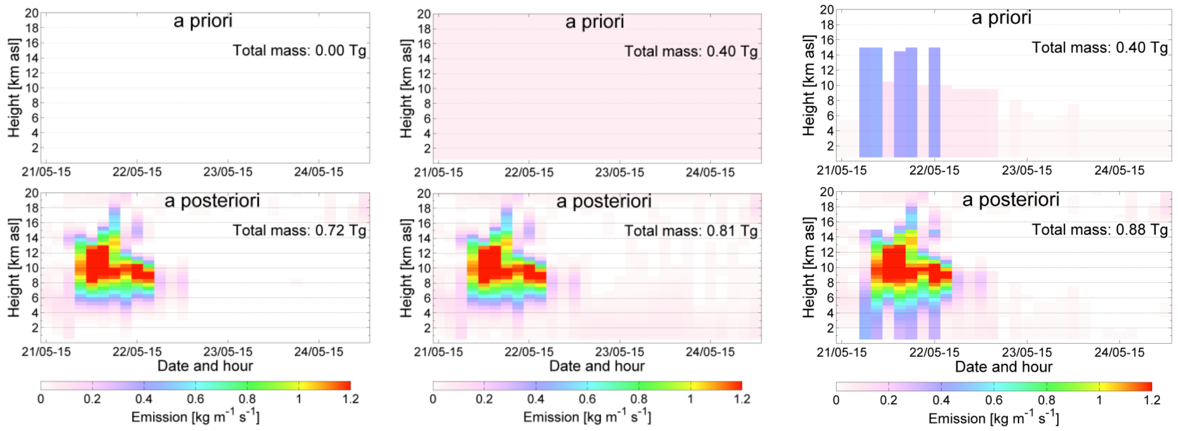

SO_2 IASI

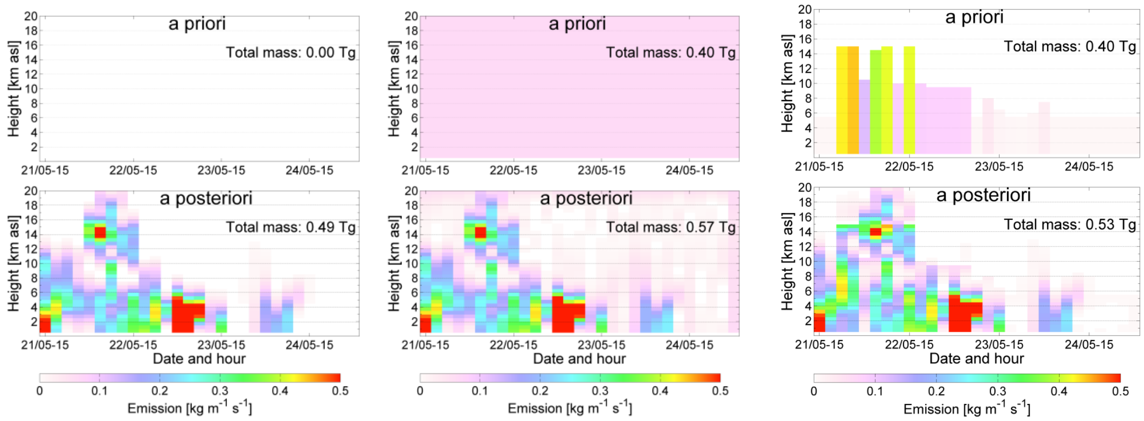

Ash IASI

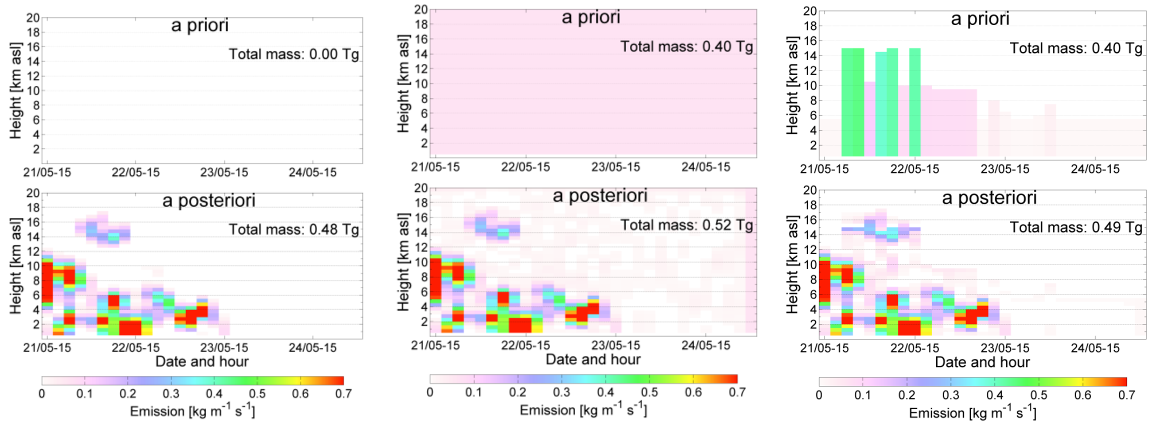

Ash SEVIRI

Figure 4.11: *The a posteriori source terms from inversion runs using three different types of a priori. From the right: Zero a priori, uniform a priori and a priori based on radar heights. Upper panel: results for* SO_2*, middle panel: results for ash with IASI satellite observations, lower panel: results for ash with SEVIRI satellite observations.*

In all three cases (one for SO_2 and two for ash), the a posteriori source terms seems quite stable to changes in the a priori. The total mass for SO_2 is 0.72 Tg, 0.81 Tg and 0.88 Tg in the cases with zero a priori, uniform a priori and a priori based on ash radar heights, respectively. For ash IASI the respective total masses are 0.49 Tg, 0.57 Tg and 0.53 Tg, while in the ash SEVIRI case, the masses are 0.48 Tg, 0.52 Tg and 0.49 Tg. This gives a maximum difference of 22 %, 16 % and 8 % for SO_2, IASI ash and SEVIRI ash, respectively. The fact that the inversion results are to a large degree stabile to changes in the a priori emissions is in good agreement with earlier studies (Kristiansen et al., 2012). This shows that this problem is so called well-constrained, meaning that there are a sufficient amount of satellite measurements to solve the problem without any absolute need for additional information from an a priori estimate. However, it also means that the inversion does not really use the a priori information.

Another way to look at this is to compare the number of unknowns to the number of observations. For the three cases investigated in this study (with all available satellite data used in each case), the number of unknowns and observations are given in table 7.

	Number of unknowns	**Number of observations used**
SO_2	1305	723 437*
IASI ash	1305	34 593
SEVIRI ash	1305	575 109

Table 7: *An overview of the number of unknowns and number of observations for the three cases SO_2, IASI ash and SEVIRI ash. *The large number of observations is a result of all the zero observation values used for the period after the major emissions. See section 3.2.3.*

The number of available observations in all cases is much larger than the number of unknowns. However, in reality the observations are not all truly independent. One satellite pixel is somehow dependent on the satellite pixels surrounding it, while the inversion assumes all three satellite pixels as independent from each other. Many available observations is quite common in volcanic eruptions and stands in contrast to, for example, inversions of radionuclide emissions from Fukushima (Stohl et al., 2012) where the a priori information is more critical.

4.4 Wind and transport

As explained in section 2.5, the transport of the material emitted by the eruption is strongly dependent on the wind direction and wind speed. In this section, an investigation of the wind direction and speed during the eruption is given. The description is based on written reports published during the eruption, the observations from a weather station and the information in the ECMWF meteorological data. Afterwards, a discussion of the reliability of the source term for SO_2 based on the wind patterns is described. The section ends with a presentation of the transport for SO_2 and ash. Since the overall distribution of the mass in the source terms with IASI ash and SEVIRI ash is the same, only the transport of the IASI ash is presented here.

4.4.1 Actual conditions

During the eruption in May 2011, the Icelandic Meteorological Office (IMO) and Institute of Earth Sciences, University of Iceland, continuously published written reports containing information of the eruption plume (height, heading, color, tephra fallout, lightning, noise) and the conditions at the eruption site (seismic tremor, earthquakes, GPS deformation, melt water). The reports were based on seismic monitoring, GPS monitoring, hydrological data, information from flights, weather radar, ashfall reports and satellite images from the Moderate-Resolution Imaging Spectroradiometer (MODIS). The reports are still available from this website: *http://en.vedur.is/earthquakes-and-volcanism/articles/nr/2180*

Identifying information regarding wind speed and direction from these reports, gives the following:

Time	**Direction and speed of wind**
22 May, 17 UTC	Most of the ash cloud heads to the south. Lower and scattered clouds head southwest and travel over the eastern part of the South Iceland Lowlands.
23 May, 17 UTC	Most of the ash cloud heads to the south. At altitudes of 8 km and higher, part of the plume heads to the west.
23 May, 19 UTC	In the last hours, the plume has reached heights of 5-9 km, but northerly winds have been very strong which can affect the height.
24 May, 16 UTC	A large part of the ash heads to the south.
25 May, 16 UTC	Light north-easterly winds, but calm winds last night and today. Southeast and southerly winds above 4 km.

Table 8: *Information on wind direction and speed from the reports generated by IMO and the Institute of Earth Sciences during the Grímsvötn 2011 eruption.*

Some information on actual conditions can also be taken from skew-T log –p charts based on observations at Keflavik weather station located about 250 km west of Grímsvötn volcano. The charts give information on temperature and dew point temperature, but also on wind direction and speed and are issued every 12 hour. Regarding the a posteriori source terms for SO_2, and ash with IASI satellite data (to the left and right of figure 4.12, respectively), it would be of particular interest to know the wind conditions at the times and heights for some of the estimated emission pulses:

i) below 4 km on 21 May 12 UTC (ash, possibly artificial emissions)
ii) below 5 km (the location of ash emissions) and from 8-12 km (the location of the mainly SO_2 emissions) height on 22 May 03 UTC
iii) below 4 km on 23 May 03 UTC (the location of ash emissions)

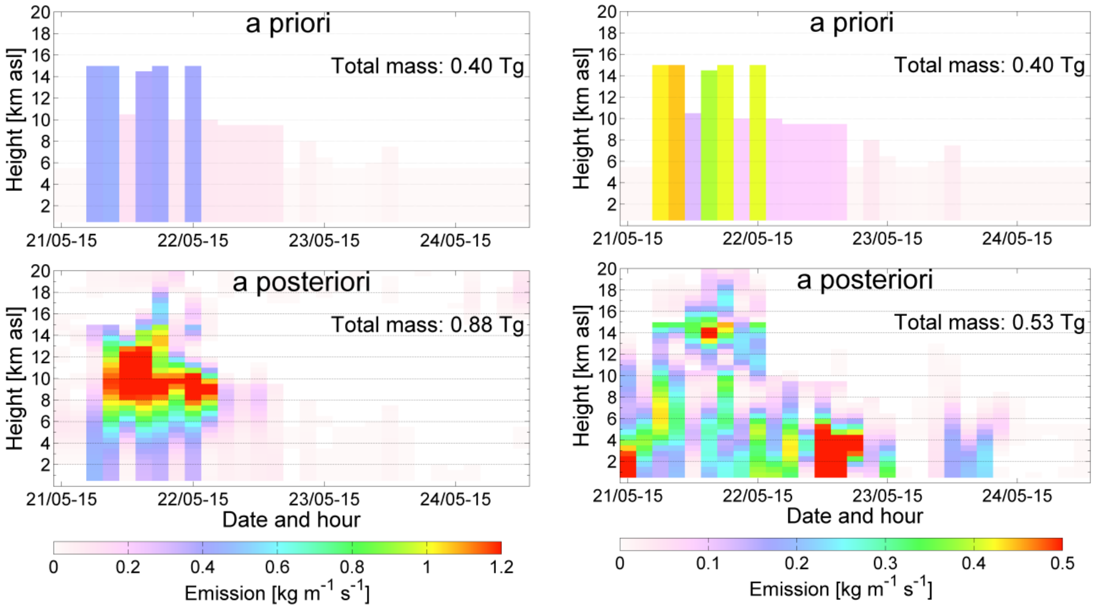

Figure 4.12: *The source terms based on inversion with* SO_2 *IASI satellite data (left) and ash IASI satellite data (right). The source terms are the same as (i) in figure 4.1 and 4.2, respectively.*

In figure 4.13(i) the skew-T log-p chart for 21 May 12 UTC is shown. The heights are given in meters above ground level, unlike the emissions in the source term that are given in meters above sea level. However, since the model flattens the topography (see section 3.2.2), the volcano is “located” 600 m above sea level, so there should not be too large errors related to directly comparing of the heights. The temperature as a function of height is shown as the thick line to the right in vertical direction. Except from in the boundary layer, the temperature is decreasing with height up to about 8.7 km where an inversion starts. This is likely the level of the tropopause. The ash emitted at this time (artifacts or not), is located too far below the height of the tropopause (see figure 4.12, right) to indicate if the emitted material reaching these heights will be slowed (and stopped) or be able to penetrate the tropopause. Information on the wind is given along the right edge of the plot. It can be seen that the wind below 4 km height is easterly (from east to west) with wind speeds decreasing from 10 m/s near the surface to 0.3 m/s or nearly calm around 4 km height.

In figure 4.13(ii) the chart for 22 May 00 UTC is given. The temperature profile is more or less the same as for the previous given time with the tropopause located around 8.7 km. As seen in figure 4.12, both the SO_2 and ash emitted at this time seem to be able to penetrate the tropopause ending up at heights above 8.7 km. The wind below 5 km is still blowing easterly, however changing direction to westerly around 5 km height. The wind is strongest closest to the ground (about 10 m/s) decreasing with height ending up nearly calm around 4-5 km height. From 8-12 km height, the wind is southerly (from south to north) with a speed of 3-5 m/s.

In figure 4.13(iii) the chart for 23 May 00 UTC is shown. The tropopause seems to have descended a few hundred meters compared to the previous time steps. A small temperature inversion around 3 km height is also seen. The a posteriori ash source term (figure 4.12, right) shows that the rather large ash masses emitted at this time is located from the ground up to about 4 km. The transport of the emissions to higher altitudes might have been slowed when the emissions reached the temperature inversion around 3 km height. The wind below 4 km height is still easterly with a speed of about 10 m/s. This shows that all in all, the wind at the different heights was more or less stationary during the three first days after the eruption onset.

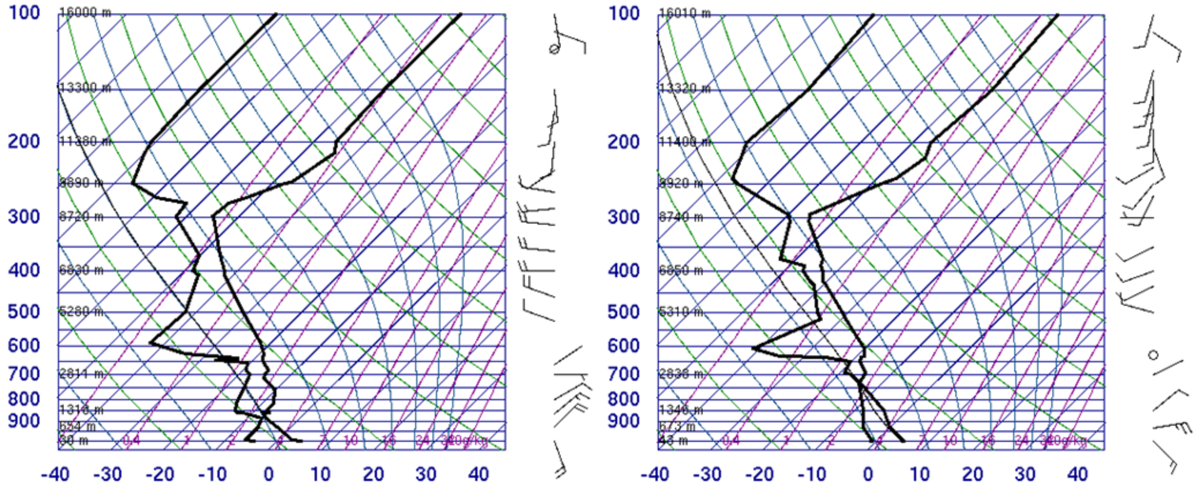

(i) 21 May 12 UTC **(ii) 22 May 00 UTC**

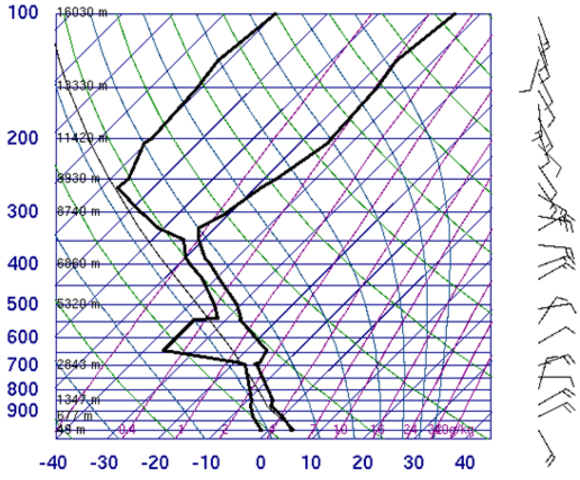

(iii) 23 May 00 UTC

Figure 4.13: *Skew –T log – p charts for Keflavik weather station located 250 km west of Grímsvötn volcano. The charts are taken from the webpage:* http://weather.uwyo.edu/upperair/sounding.html *and are provided by University of Wyoming, College of Engineering, Department of Atmospheric Science.*

The wind data shown above is, however, not the one used in the computation of the source terms. A quick check of the wind fields in the meteorological data used in the simulations can be done by plotting the results from the sensitivity runs (see section 3.2.2) for each source height. This will give the direction of transport for the material emitted at a given height level. The output is not scaled with any satellite sensitivity and is based on a uniform distribution of mass in height and time, so the figures only show the direction of transport of the mass, not concentrations. The output presented here is for ECMWF data, but testing shows the directions are more or less the same for GFS data.

Figure 4.14 shows that the mass transport for emissions at altitudes below 4 km height on 21 May 12 UTC is mainly towards south. The figure further shows that for altitudes below 5 km on 22 May 03 UTC the mass transport is towards south. Close to 6 km it seems like some of the mass transport is shifting towards the north. The northwards transport continues up to (at least) 12 km height. For emissions below 4 km height around 23 May 03 UTC the mass transport is to the south-east.

Release time: 21 May 12 UTC

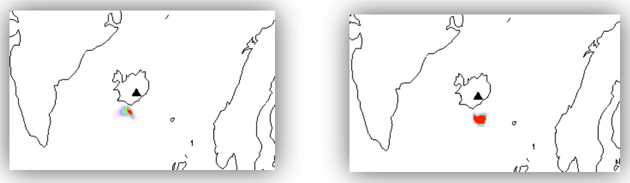

1000-1500 m a.g.l **3500-4000 m a.g.l**

Release time: 22 May 03 UTC

3500-4000 m a.g.l **5500-6000 m a.g.l** **8000-8500 m a.g.l** **10 500-11 000 m a.g.l**

Release time: 23 May 03 UTC

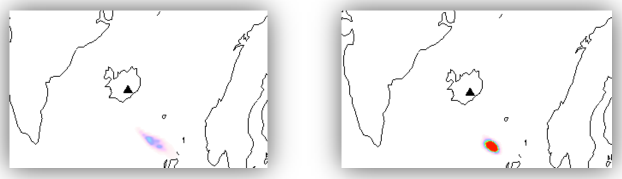

1500-2000 m a.g.l **3000-3500 m a.g.l**

Figure 4.14: *The results from the sensitivity runs illustrated for each source height. The output is for ECMWF meteorological data.*

To summarize, each of the three types of information regarding wind direction and speed (i.e. reports from IMO, skew-T log-p charts and plots of sensitivity runs) evidence that the mass emitted to heights from 6 km and higher is transported to the north. For the masses below 4 km, the IMO reports indicate that the transport is somewhat to the west near the coast, but mostly to the south. The skew-T log-p charts show wind to the west while the plots of the sensitivity runs shows that the transport is to the south. The differences in the wind direction below 4 km height might be due to the fact that the weather station is located 250 km away from Grímsvötn, and therefore might observe different wind than is the reality at the location of Grímsvötn.

4.4.2 SO_2 emissions into the stratosphere

It is interesting to evaluate the emissions of SO_2 from Grímsvötn to see whether they reached the stratosphere and could have an impact on the climate (see section 2.2). As given by the skew-T log-p charts (figure 4.13) the tropopause over Iceland in the actual period of the eruption time seems to be located around 8.5 km height. This also fits with the photo of the eruption column and the level of horizontal spread shown in figure 2.6. The a posteriori source term in figure 4.12 (left) gives that 0.5 Tg of the total 0.8 Tg SO_2 is emitted to heights above 8 km, i.e. into the lower stratosphere. No studies have been performed to directly calculate the potential climate effect from the Grímsvötn SO_2 emissions, but Kravitz et al. (2010) did model simulations to estimate the potential climate effects of the Kasatochi (Alaska) eruption on 8 August 2008. The total emissions from the Kasatochi eruption were estimated to 1.7 Tg with ~1 Tg reaching the stratosphere (Kristiansen et al. 2010). Kravitz et al. (2010) did simulations with 1.5, 3 and 5 Tg SO_2 emitted into the lower stratosphere. The simulations showed changes in the shortwave radiative forcing, and that the effect increased linearly with atmospheric loading of SO_2. However, the radiative forcing was still small due to the location of the volcano (52° N) and the timing of the eruption with little insolation by the time the sulphate aerosols would form. The timescale for formation of sulphate aerosols from SO_2 is generally about 1-2 weeks (see section 2.2) but strongly dependent on the amount of sunlight available. In the Kasatochi case the sulphate aerosol loading would be on its maximum during fall and start of winter. At this time the insolation at the actual latitude would be low. The magnitude of the eruption (i.e. the height and amount of the emissions) was also found to be insufficient to provide sulphate aerosols persisting in the stratosphere into the following spring.

Grímsvötn erupted in May, so the sulphate aerosols mass loading was on its maximum during spring and summer i.e. in the period with maximum solar insolation at this latitude (64°N). Even though the total SO_2 mass was lower than the Kasatochi eruption and below the lowest value used in the simulations for Kasatochi, the climate effects may be different due to the much larger insolation in the Grímsvötn case. Even though the total SO_2 emitted by Grímsvötn was not so large compared to other eruptions, simulations to investigate potential climate effects of the Grímsvötn eruption would be of great interest, but is not yet performed. The same is for the eruption of NABRO volcano (Eritrea) in June 2011 where about 1.5-4.5 Tg SO_2 was emitted to heights at tropopause level (Clarisse et al., 2012; Theys et al., 2012).

However, the SO_2 mass injected into the stratosphere in all the three cases mentioned here is much lower than the 20 Tg injected in the famous eruption of Mt. Pinatubo (Philippines) in June 1991 which lead to climate effects detected in many studies, e.g. decreased surface temperature (IPCC Assessment report, found here *http://www.ipcc.ch/publications_and_data/ar4/wg1/en/ch2s2-7-2.html*)

4.4.3 Evaluation of the SO_2 source term below 5 km height

With the information about the wind directions given in the previous section, it is possible to say more about the reliability of the SO_2 source terms from figure 4.1((i) and (ii)). As pointed out in section 4.1 conclusions regarding the mass below 5 km height cannot be taken only based on an inversion with IR measurements.

To check if the SO_2 source term is reliable below 5 km height a check with observations from GOME-2 and SCIAMACHY is performed. As explained in section 2.3.1.3 and 2.3.1.4, GOME-2 and SCIAMACHY observe in the UV channels, thus having higher sensitivity to SO_2 also below 5 km height. Observations by GOME-2 and SCIAMACHY on 22 and 23 May are shown in figure 4.15.

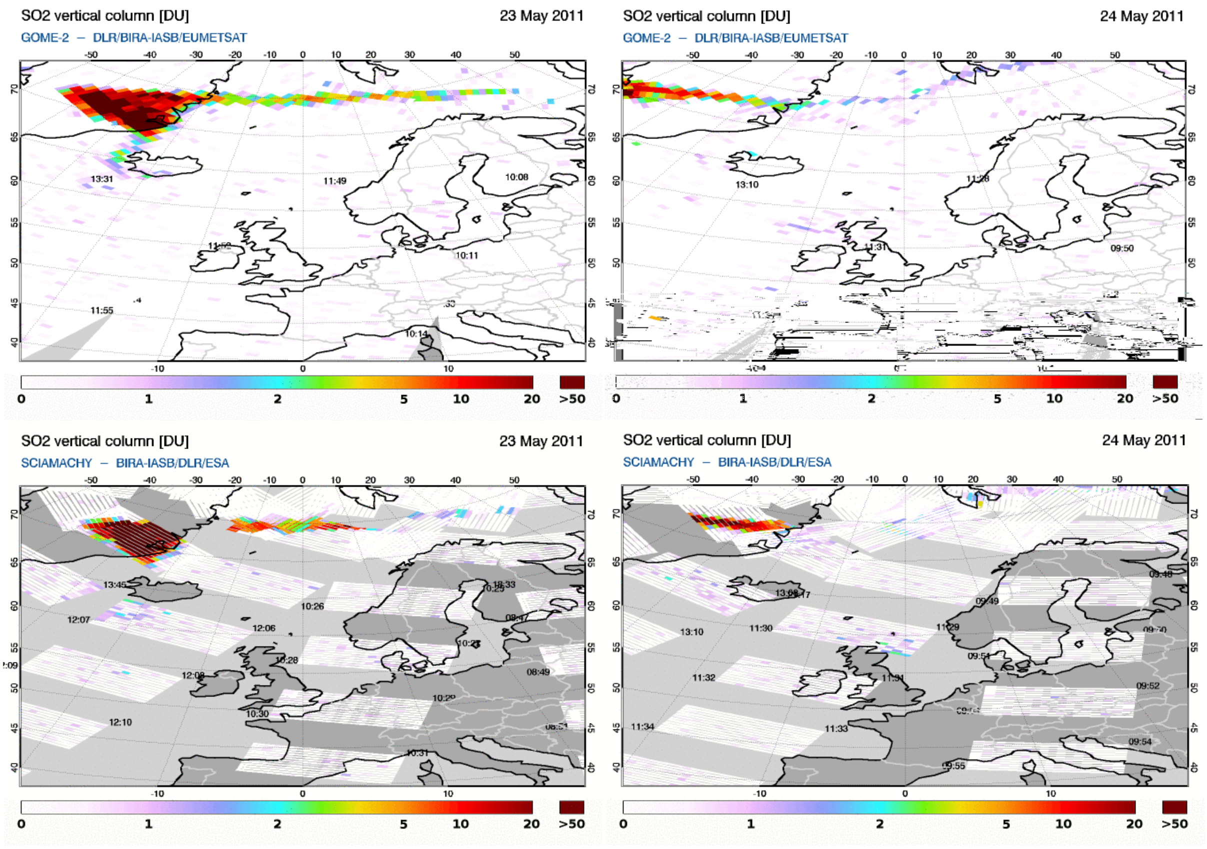

Figure 4.15: *Observations by GOME-2 (upper panel) and SCIAMACHY (lower panel) on 22 and 23 May 2011. Source:* http://sacs.aeronomie.be/archive/index.php

If SO_2 mass was emitted to heights below 5 km, it should due to the prevailing winds outlined in previous section, has been transported towards south(-west) and then south-east, together with the ash. Since neither GOME-2 nor SCIAMACHY observe significant masses of SO_2 moving in these directions, it is indeed likely that there was little SO_2 emitted to heights below 5 km. Thus, the SO_2 a posteriori source terms in figure 4.1((i) and (ii)) are seen to be reliable even for low altitudes.

The fact that the SO_2 was mostly emitted to high altitudes also fits well with measurements from AIRS and OMI instrument. Estimation of total SO_2 emissions based on AIRS data was 0.13 Tg on 23 May, while the estimation based on OMI data was 0.15 Tg on 22 May (Fred Prata, personal communication). Since OMI observes in the UV-channels, it can like GOME-2 and SCIAMACHY provide better observations from lower altitudes than AIRS that like IASI and SEVIRI observes in the IR-channels. The consistent number obtained from OMI and AIRS sounders show that the IR-sounder has not missed substantial amounts of low-altitude SO_2, and thus, most of the SO_2 was likely emitted to high altitudes.

4.4.4 Transport and separation of SO_2 and ash

Now when the source terms are evaluated and shown to be reliable in most cases, they are fed into FLEXPART and the model is run forward to simulate where the masses are transported. In figure 4.16-4.19 the horizontal dispersion and vertical zonal plots for some chosen time are shown. Only the transport of the SO_2 source term and the source term based on IASI ash is presented here. The position of the volcano is marked with a black triangle, ▲.

Already for the first illustrated time, **22 May 06:00 UTC** (figure 4.16), it is possible to detect that most of the SO_2 is transported northward. The vertical zonal plot shows the SO_2 is mostly emitted to heights from 8-14 km as given by the source term in fig. 4.12 (left). Most of the ash mass is located in the southern part of Iceland. The ash is mostly emitted to heights from 3-4 km and from 10-15 km.

On **23 May 06:00 UTC** (figure 4.17) it is visible that the SO_2 cloud moving north in the previous time step now is drifting more to the east. Also a small part of the SO_2 cloud is transported south-eastward together with the ash. The mass of the earlier emitted ash seems to be the same both for the south and north moving cloud. However, the ash is now emitted to heights below 5 km, and seems to move to the south.

On **24 May 06:00 UTC** (figure 4.18) most of the SO_2 is transported westward at an altitude of 6-11 km, located as a cloud over Greenland. The part of the SO_2 cloud heading east is transported lower, at around 5 km height. Most of the ash is now in the east moving cloud travelling along the northern shore of Great Britain with a height of about 2-3 km. The earlier north going ash has been transported west and is now located above Greenland at a height of about 10 km.

For the last time step shown here, namely **25 May 06:00 UTC** (figure 4.19), the SO_2 is transported further west and it seems like the masses increase their altitude now being located mainly around 9-12 km height. The SO_2 transported east on the other hand, seems to descend in altitude. The low altitude ash cloud is now moving further east passing the southern parts of Norway and Sweden. The height of the cloud is still 2-3 km, but the total mass has lowered since last time step. The cloud above Greenland is on the other hand, stationary in location and also quite stabile in mass. This is likely because of calmer wind and less effect from removal processes (no/small wet deposition above tropopause) than in the east going cloud at low altitudes.

Overall, there seems to be a clear separation of SO_2 and ash with SO_2 first moving north and then westward and most of the ash first moving south and then eastward. However, there is also some ash being transported north and then westward together with the SO_2. The concentrations of this ash is however very low.

22 May 06:00 UTC

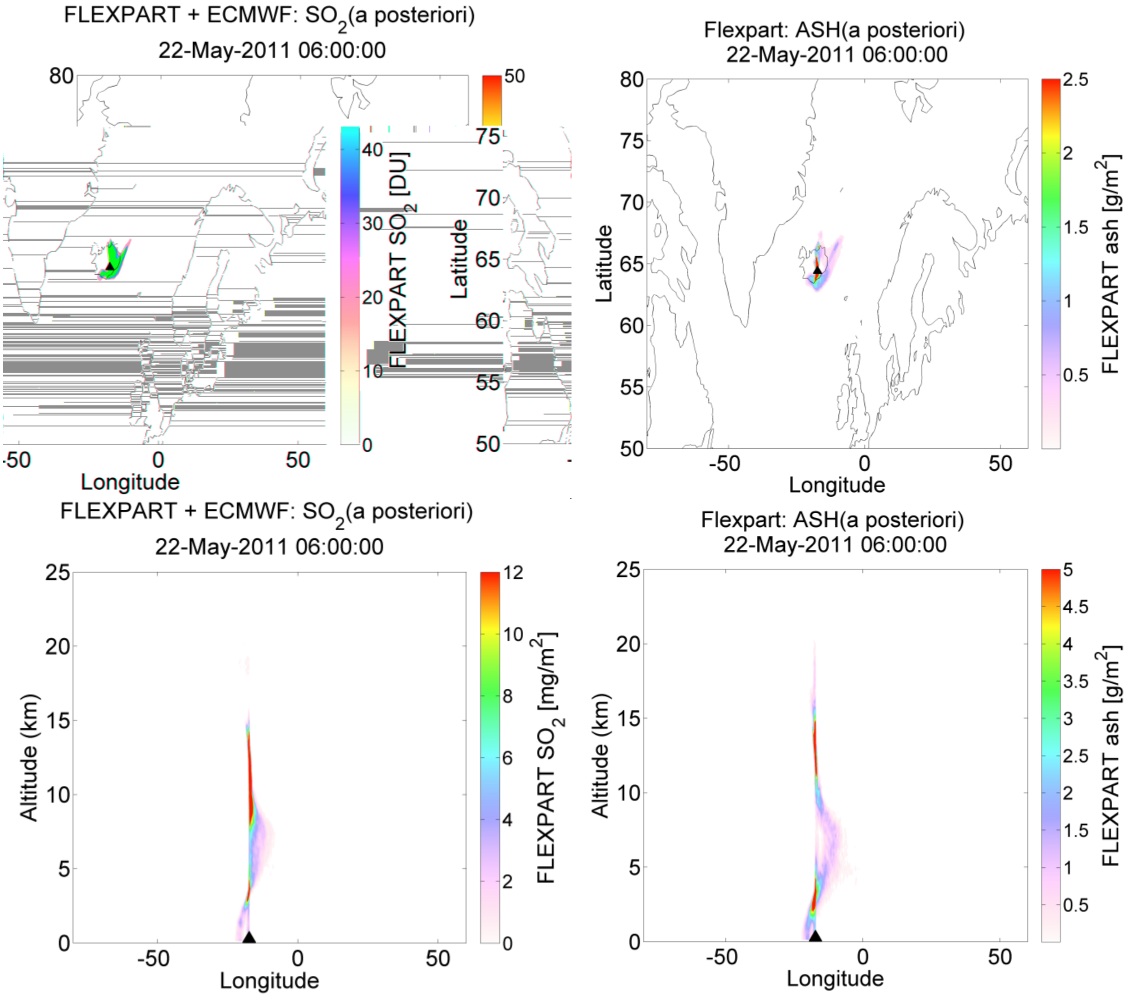

SO_2 **Ash IASI**

Figure 4.16: *Transport of the SO_2 and ash from Grímsvötn 22 May as simulated by FLEXPART using the source terms to the left (SO_2) and right (ash) of figure 4.12.The upper panel for each time step shows the horizontal dispersion while the lower panel shows the vertical zonal plots where mass is integrated over all latitudes. No weighting functions are applied to the output.*

23 May 06:00 UTC

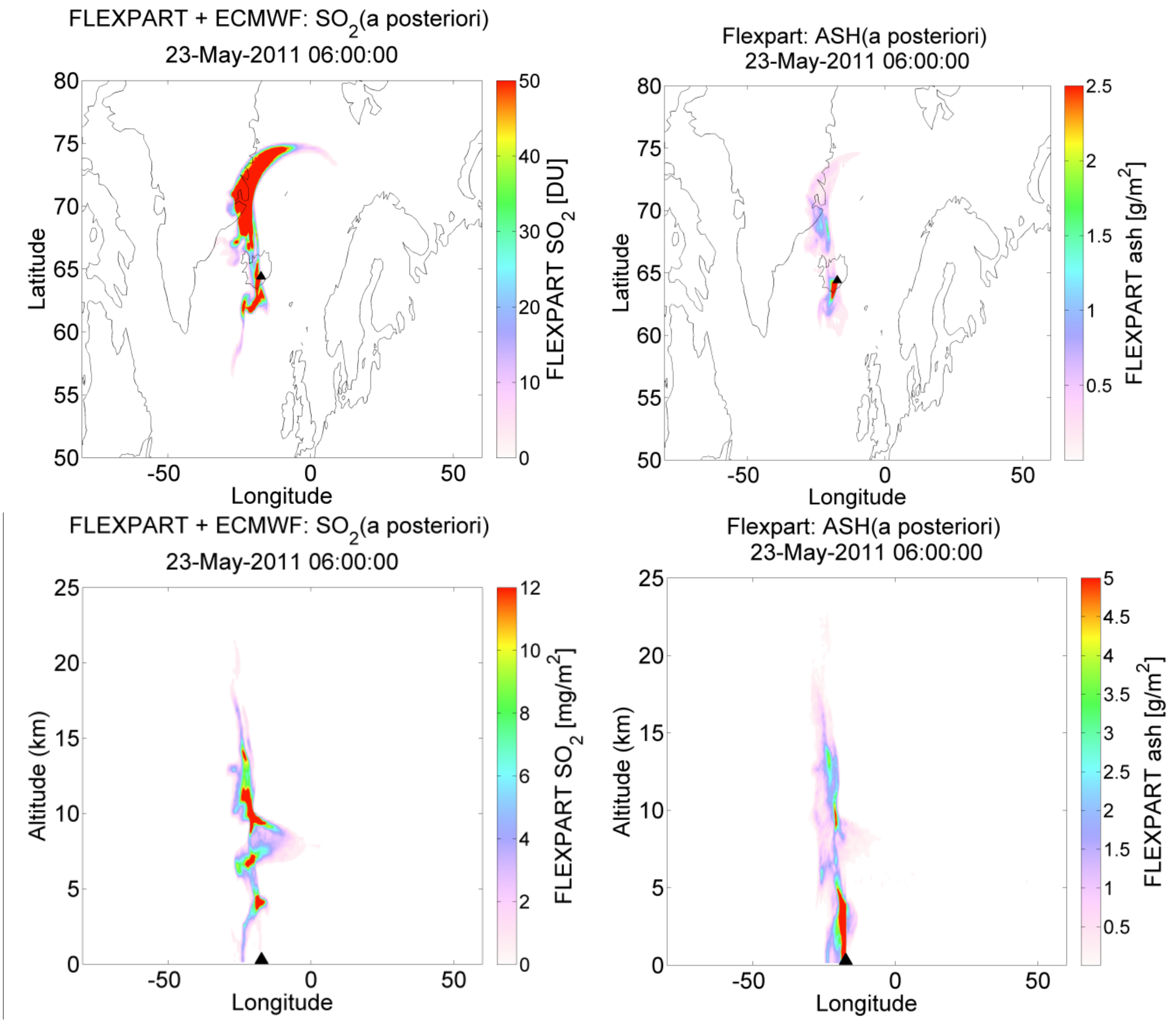

SO_2 IASI **Ash IASI**

Figure 4.17: *Transport of the SO_2 and ash from Grímsvötn 23 May as simulated by FLEXPART using the source terms to the left (SO_2) and right (ash) of figure 4.12.The upper panel for each time step shows the horizontal dispersion while the lower panel shows the vertical zonal plots where mass is integrated over all latitudes. No weighting functions are applied to the output.*

24 May 06:00 UTC

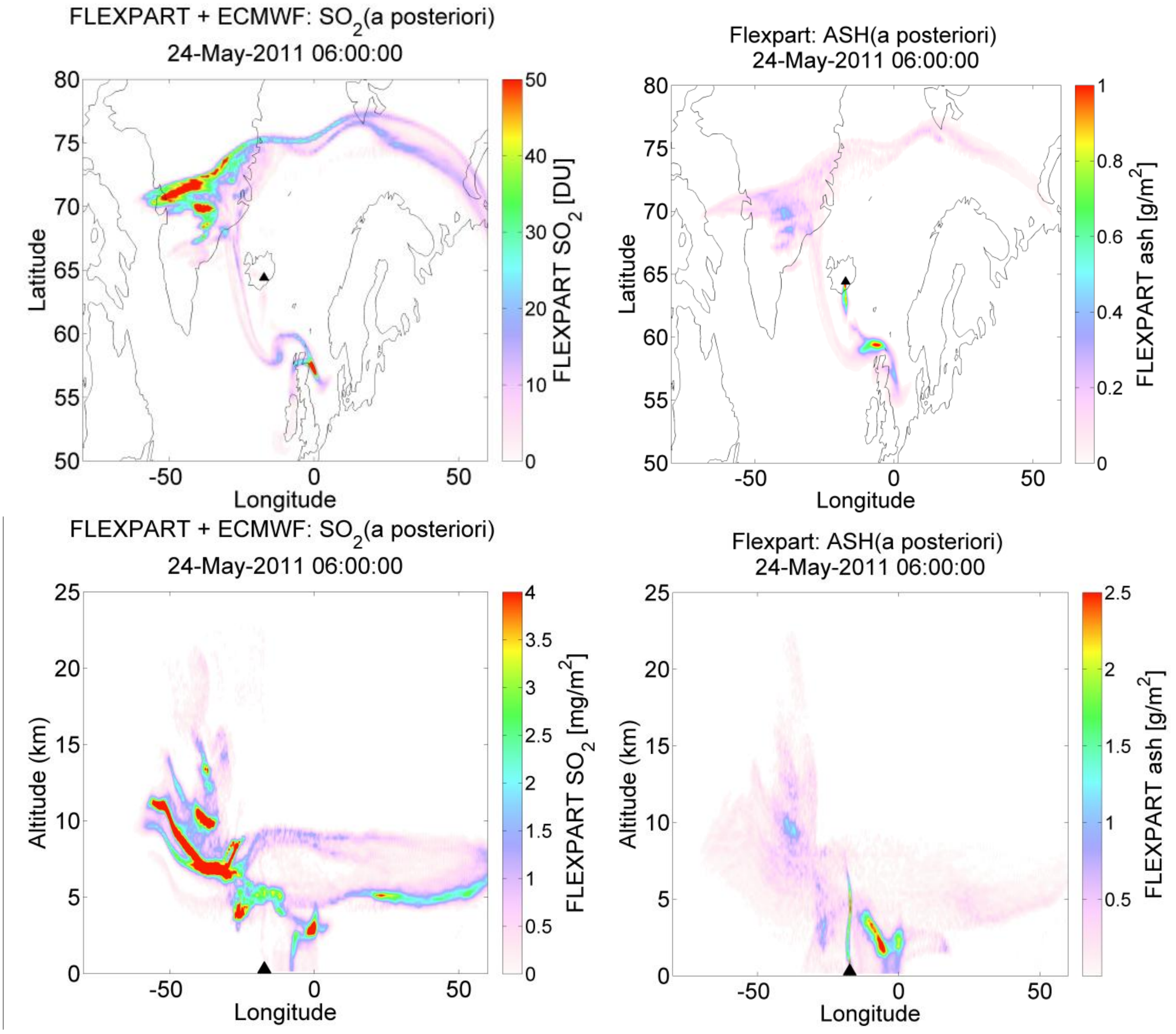

SO_2 IASI **Ash IASI**

Figure 4.18: *Transport of the SO_2 and ash from Grímsvötn 24 May as simulated by FLEXPART using the source terms to the left (SO_2) and right (ash) of figure 4.12. The upper panel for each time step shows the horizontal dispersion while the lower panel shows the vertical zonal plots where mass is integrated over all latitudes. No weighting functions are applied to the output.*

25 May 06:00 UTC

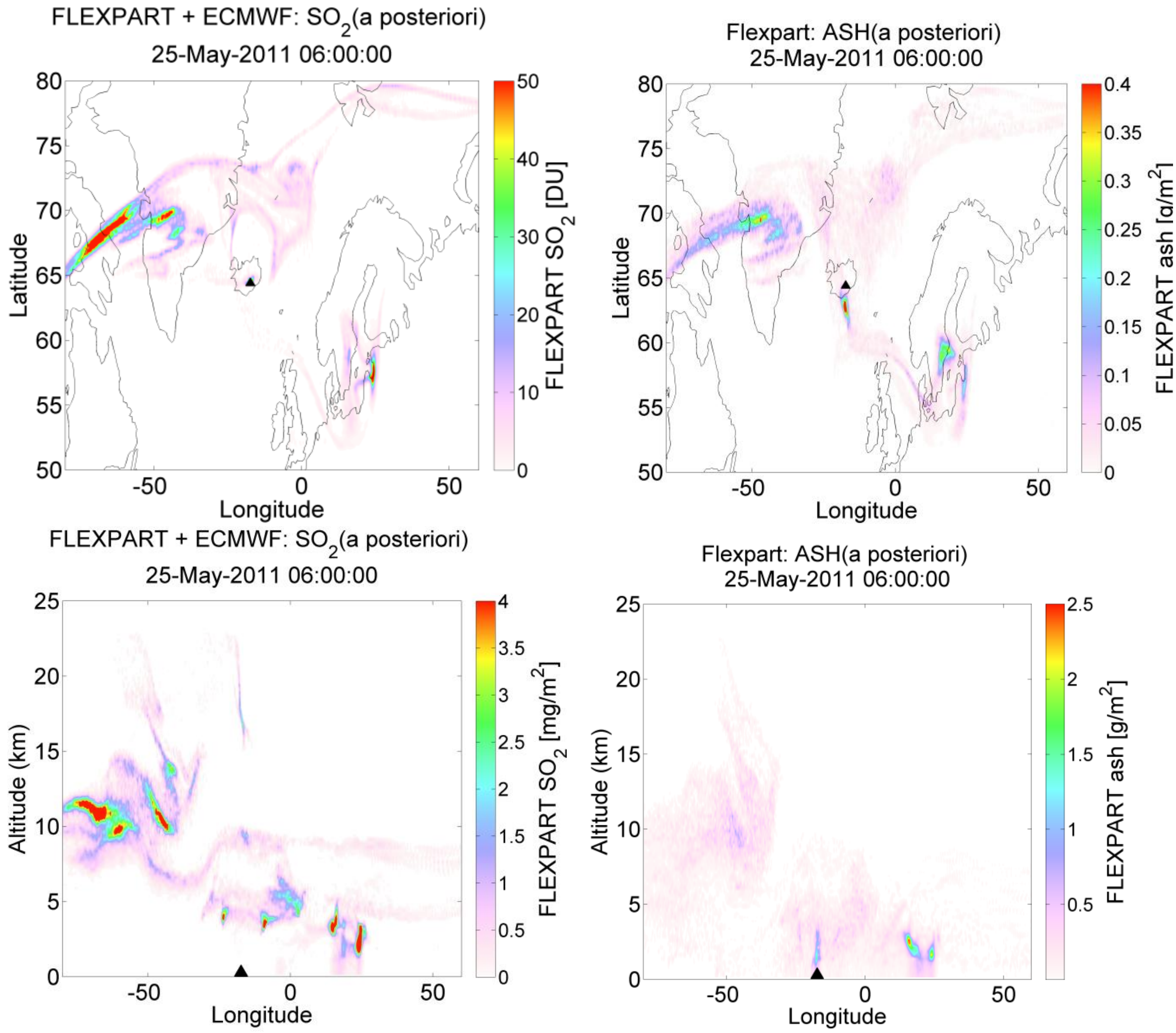

SO_2 IASI **Ash IASI**

Figure 4.19: *Transport of the SO_2 and ash from Grímsvötn 25 May as simulated by FLEXPART using the source terms to the left (SO_2) and right (ash) of figure 4.12.The upper panel for each time step shows the horizontal dispersion while the lower panel shows the vertical zonal plots where mass is integrated over all latitudes. No weighting functions are applied to the output.*

4.5. Validation

The results presented in section 4.4.4 (i.e. transport with source terms produced by SO_2 and IASI ash satellite measurements) are validated against independent data in this section. All data not used in the inversion can be considered independent. SO_2 results are validated by comparing a FLEXPART simulation using the source term from figure 4.12 (left) as input, with independent observations of the volcanic SO_2 clouds from the satellite instruments GOME-2, SCIAMACHY and AIRS. To validate the estimated ash source term in figure 4.12 (right) the a posteriori transport simulations were first compared to hourly ash mass concentrations at four air quality monitoring stations in Scandinavia. Further, the simulated a posteriori ash concentrations in the column above Stockholm were compared to vertically resolved LIDAR measurements. Finally a comparison of the ash source term produced in the inversion method was compared to the source term produced by London VAAC during the eruption.

4.5.1: SO_2 validation with independent satellite data

The FLEXPART simulations using the SO_2 source term from figure 4.12 (left) as input is first compared to independent data from GOME-2 and SCIAMACHY instruments (see section 2.3.1.3 and 2.3.1.4) which both use channels in the UV part of the electromagnetic spectrum. The FLEXPART output is scaled with the UV height sensitivity curve from figure 3.7 and then compared to the UV satellite observations. The result is shown in figure 4.20. GOME-2 and SCIAMACHY are both instruments onboard polar orbiting satellites, so some areas in the plots are without data. The grey stripes/dots show where satellite data are available, but zero concentrations values were measured.

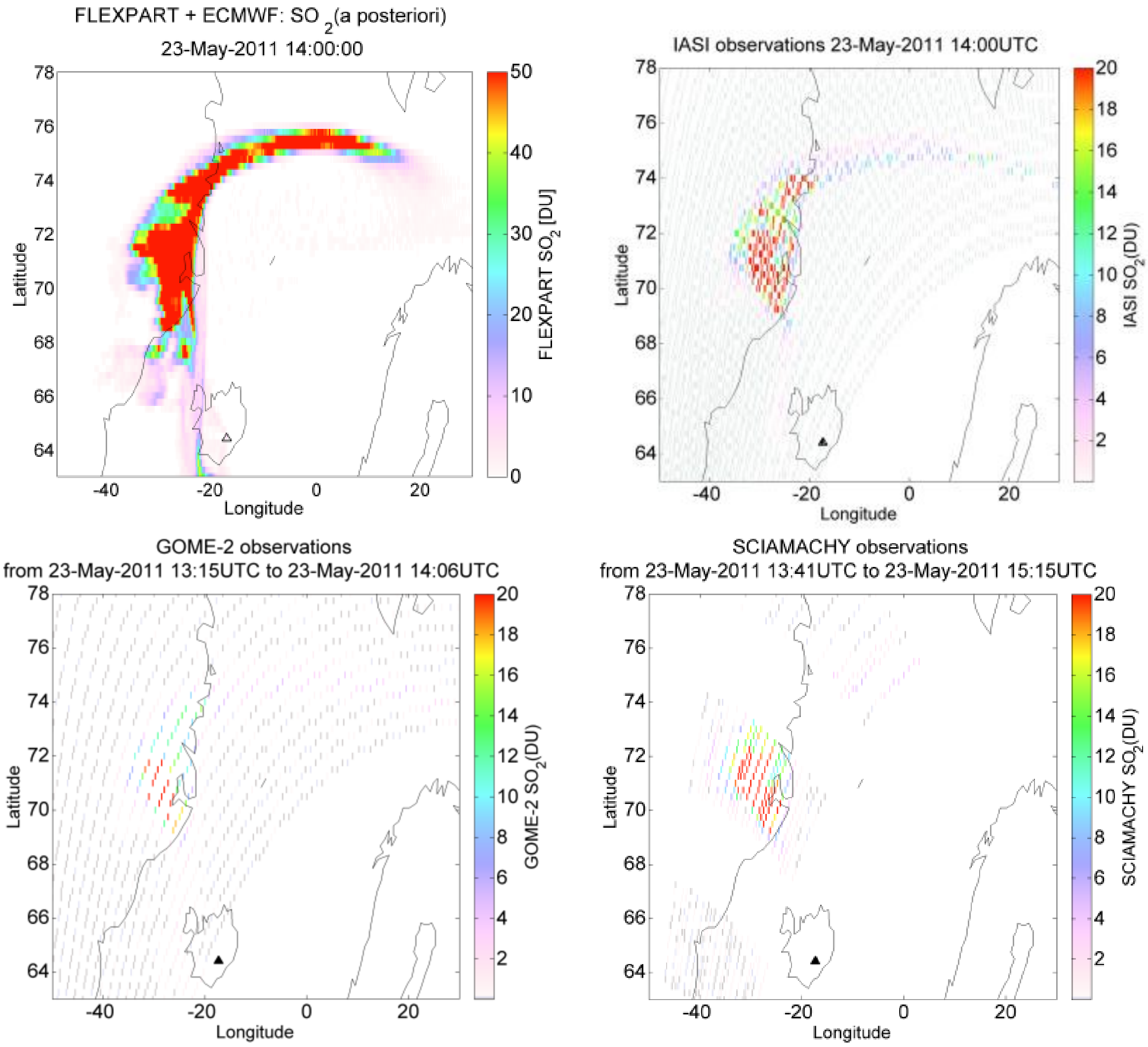

Figure 4.20: *Upper panel: The simulated SO_2 cloud using a posteriori source term from figure 4.12 (left) and one of the satellite overpasses used in the inversion to estimate the source term. Lower panel: Independent satellite data from GOME-2 and SCIAMACHY. All data are on the same spatial grid and given for the time around 13:00 to 15:00 on 23 May. The FLEXPART output is scaled with the UV satellite sensitivity given in figure 3.7.*

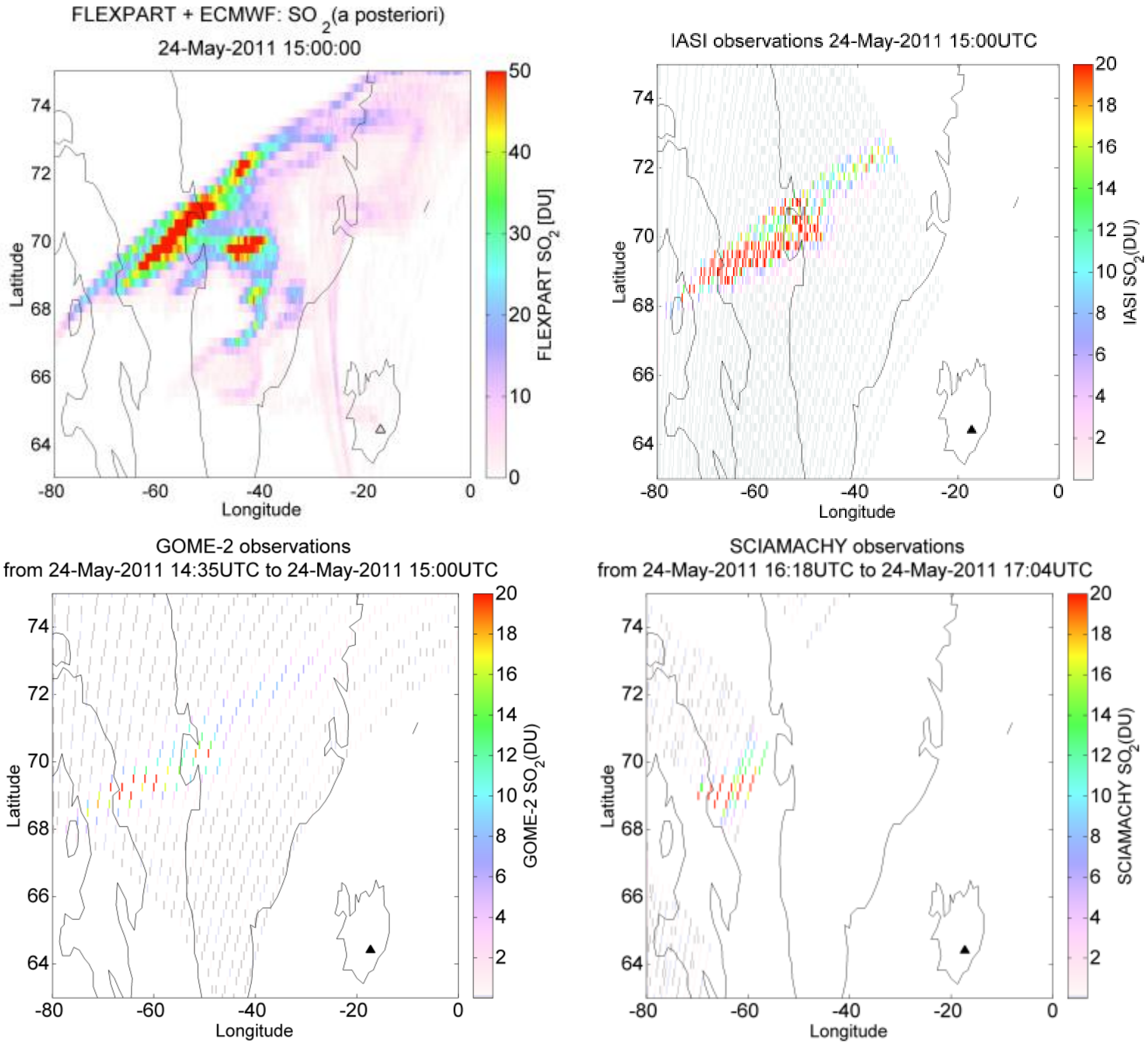

Figure 4.21: *Same as figure 4.20, but for the time around 14 to 17 UTC on 24 May.*

All over, figure 4.20 and 4.21 show good agreements between the a posteriori SO_2 masses estimated by FLEXPART and the observations by GOME-2 and SCIAMACHY. It seems that the masses over Greenland on 23 May (figure 4.20) are somewhat larger in the FLEXPART simulations than observed by GOME-2. However, it seems that SCIAMACHY gives masses on the same size as FLEXPART. On 24 May (figure 4.21) both GOME-2 and SCIAMACHY show the cloud over Greenland at nearly the same location and with the same masses as the FLEXPART simulations. As discussed in section 4.2 the part of the SO_2 cloud on the southern end of Greenland is not observed by the IASI satellite data and might be unreal. The GOME-2 instrument captures the actual area from 14:35 to 15:00 UTC on 24 May (figure 4.21, bottom left) and observes like IASI any SO_2 masses at the southern end of Greenland.

The SO_2 masses over Greenland are also compared to satellite data from AIRS. The result is given in figure 4.22. Since AIRS observes in the IR channels, the FLEXPART output is this time multiplied with the IR-weighting function from figure 3.7. AIRS shows a maximum in the SO_2 mass at the western part of the cloud over Greenland. This is to some extent also visible in the FLEXPART simulations, though at a somewhat lower magnitude. It can be concluded generally that the agreement between the FLEXPART simulations and the AIRS observations is quite good. The thin SO_2 cloud on the southern part of Greenland is by AIRS, like by GOME-2, not observed. Thus, it can be concluded with rather high certainty that the masses located in this area in the FLEXPART simulations are unreal and due to artifacts in the meteorological and/or IASI satellite data.

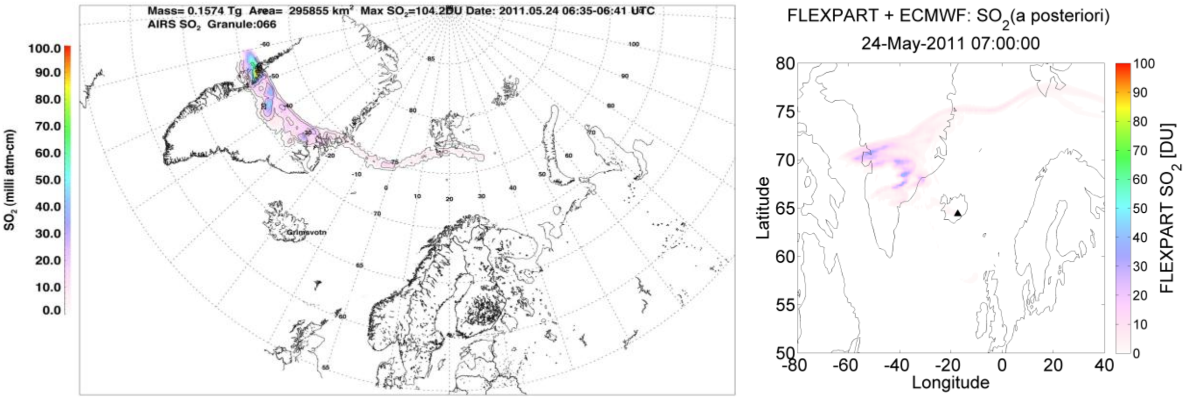

Figure 4.22: *To the left the SO_2 masses retrieved from AIRS data on 24 May 06:35-06.41. Courtesy: Fred Prata (NILU). To the right are the masses as simulated by FLEXPART scaled with the IR-weighting function from figure 3.7. Remark that the masses are on different spatial grids.*

4.5.2 Ash validation with surface and LIDAR measurements

To validate the estimated ash source terms and the ash a posteriori FLEXPART simulations, the PM10 concentrations from the model output (i.e. only taking the particles with size 4, 6 and 8 µm) were compared to hourly PM10 concentrations at air quality monitoring stations at given sites in Scandinavia presented in Tesche et al. (2012). The sites used for comparison are Oslo (Norway), Gothenburg and Stockholm (Sweden) and Helsinki (Finland) (see figure 4.23 for locations). It is important to take into consideration that these surface measurements also include other types of particles such as and dust, thus not only volcanic ash from Grímsvötn. The upper panel of figure 4.24 shows that this *background concentration* is of the order of 10-30 µg/m^3. The background concentration is not included in the FLEXPART simulation output, so to be able to compare observed and simulated PM10 values a background concentration of 20 µg/m^3 has been added to the FLEXPART PM10 concentrations. Additionally, only the PM10 concentrations from the lowest layer (i.e. 0-250 m above ground level [a.g.l]) in the FLEXPART output were used.

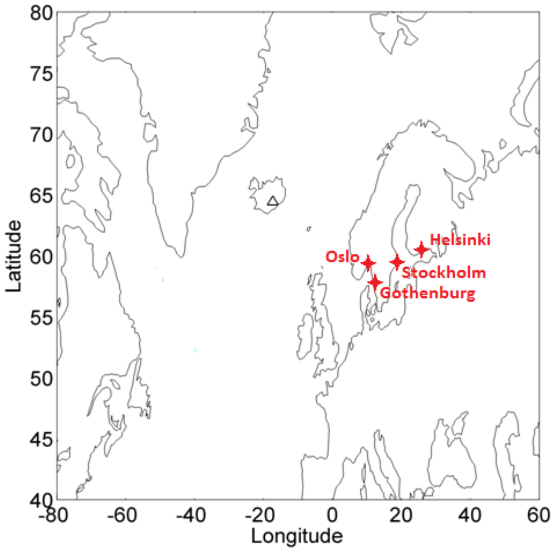

Figure 4.23: *Map showing the location of the measurements sites used for validation of the estimated a posteriori source terms and the ash a posteriori FLEXPART simulations.*

The middle panel of figure 4.24 shows the FLEXPART simulated PM10 concentrations using the a posteriori source term estimated from IASI ash satellite data (4.12, right). The time of the maximum concentrations in the simulation is showing up about the same time as the observations for Gothenburg and Oslo measurement sites while there is a small delay of about 6 hours for the modeled maximum concentrations over Stockholm and Helsinki. However, lower PM10 concentrations are simulated to reach the two latter stations at exactly the same time as the first significant observed increase in the PM10 values.

The absolute values of the concentrations are from about a factor of 1.5 to 3 smaller in the FLEXPART simulation compared to the measurements. However, to take the values from the lowest output layer and compare them to the surface measurements is not completely correct. The surface measurements are taken close to the surface while the lowest output layer is from 0-250 m a.g.l. and the modelled concentrations are averaged over this height layer. It is however most likely that the total simulated mass, and then also the PM10 fraction in the surface layer really is too low since this was seen to some extent in the consistency checks in section 4.2 where it was shown that FLEXPART gives lower concentrations than the satellite observations, probably due to errors in removal processes. Another suggestion is that the too low PM10 concentrations are due to incorrect initial ash particle size distribution, i.e. that a too small fraction of the total mass is putted into the PM10 size classes (4, 6 and 8 µm). However, all in all, the comparison shows that the simulated and observed PM10 concentrations are quite similar.

The lower panel of figure 4.24 shows the FLEXPART simulated PM10 concentrations using the a priori source term estimated from IASI ash satellite data (figure 4.12, right). The maximum concentrations in Gothenburg and Oslo are not that clear as in the a posteriori emissions and they are also lower than the in the simulations with the a posteriori source term. In Stockholm and Helsinki it is almost no increase in the concentrations during the simulation.

All over, the concentrations in the simulations with the a posteriori source term are much closer to the surface measurements than the concentrations in the simulations with the a priori source term. This illustrates that the inversion is working as expected, producing a posteriori emissions that are more similar to the observations, and therefore likely closer to reality, than the a priori emissions.

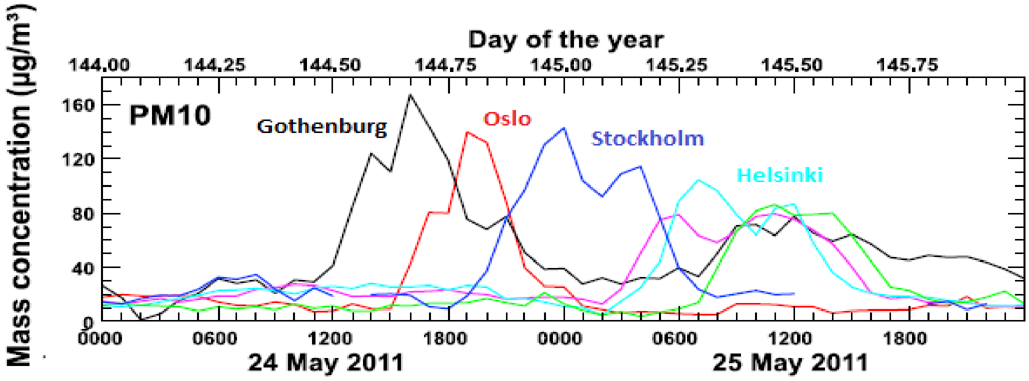

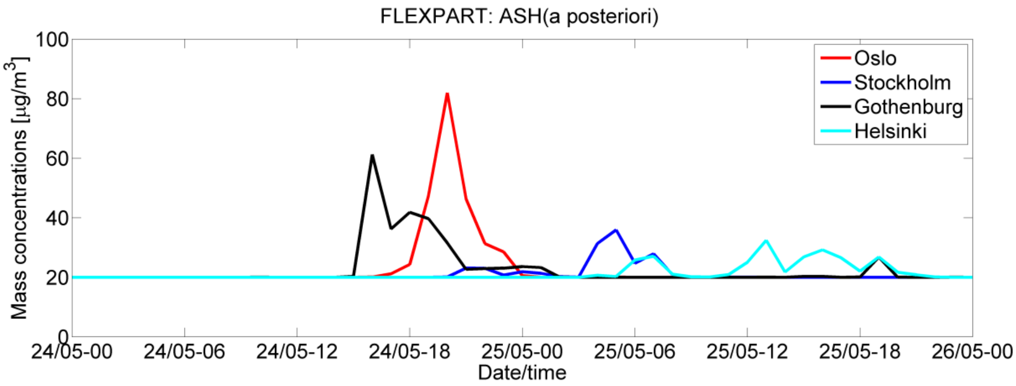

FLEXPART a posteriori

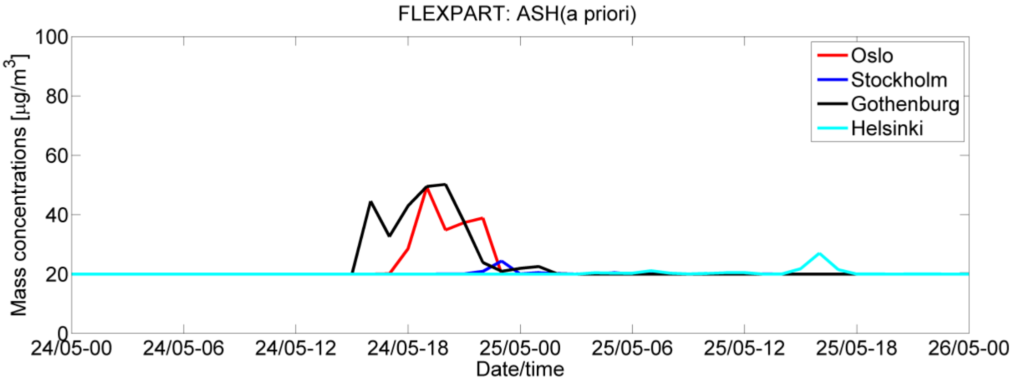

FLEXPART a prori

Figure 4.24: *Upper panel: The hourly PM10 concentrations observed at air quality monitoring stations at four sites in Scandinavia. The colored lines not labeled belong to other measurement sites not taken into consideration here. Figure adapted from Tesche et al. (2012). Middle panel: The FLEXPART simulated PM10 a concentrations of ash in the lowest model output layer (0-250 m a.g.l) from the simulation using the a posteriori source term to the right in figure 4.12. Lower panel: The FLEXPART simulated PM10 concentrations of ash in the lowest model output layer (0-250 m a.g.l) from the simulation using the a priori source term to the right in figure 4.12.*

Tesche et al. (2012) also present LIDAR measurements above Stockholm. The LIDAR observes the backscattered signals and the ash mass is then estimated based on different assumptions about ash extinction and coarse mode fraction. The upper panel of figure 4.25 shows the ash mass concentrations estimated from 30 min mean LIDAR profiles between 03:00 and 07:30 on 25 May 2011 at Stockholm. The grey area represents the range between estimated minimum and maximum values based on the different assumptions in the estimates. The peaks around 1 km height are caused by swollen aerosols and unscreened thin clouds and are therefore not ash to be compared to the FLEXPART model output. The lower panel shows the PM10 concentrations above Stockholm as simulated by FLEXPART between 03:00 and 07:00 on 25 May 2011 with the a posteriori source term to the right in figure 4.12.

The LIDAR measurements show maximum mass concentration around 2.5 km height and the maximum observed concentrations are for the time around 03:00-04:00 UTC. Measurements for times before 03:00 UTC are not shown in figure 4.25, but given in Tesche et al. (2012). This corresponds well to the second peak in the surface measurements for Stockholm given in upper panel of figure 4.24. The modelled ash concentrations have a maximum around 2 km height, in very good agreement with the measurements. However, the maximum simulated concentrations at 2 km height seem to occur at a slightly later time than the measurements which agrees with the surface data in figure 4.24. The simulated ash mass seems also to decrease slower than the measurements, thus leading to somewhat too large masses for the times after the maximum.

Taking into account that the mass concentrations derived from LIDAR measurements are assumed to have an uncertainty of a factor of 2 (Tesche et al., 2012), the matching agreement between the LIDAR measurements and the FLEXPART output can still be concluded to be very good.

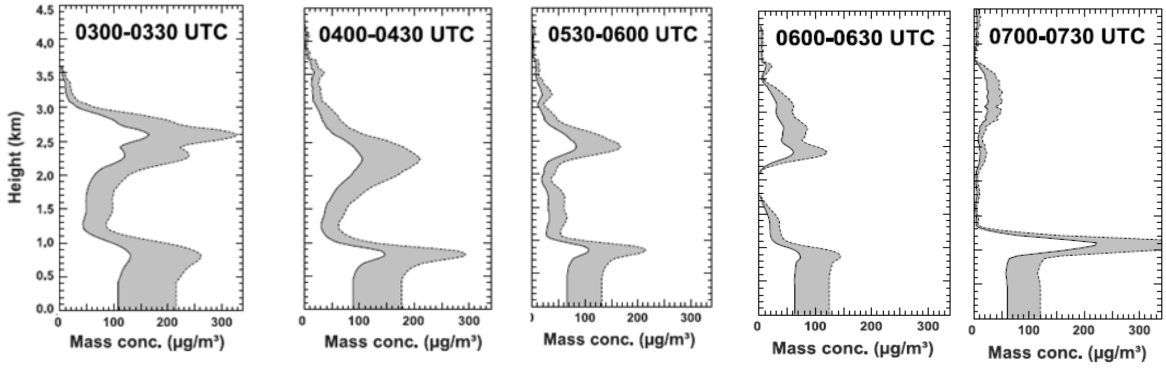

LIDAR

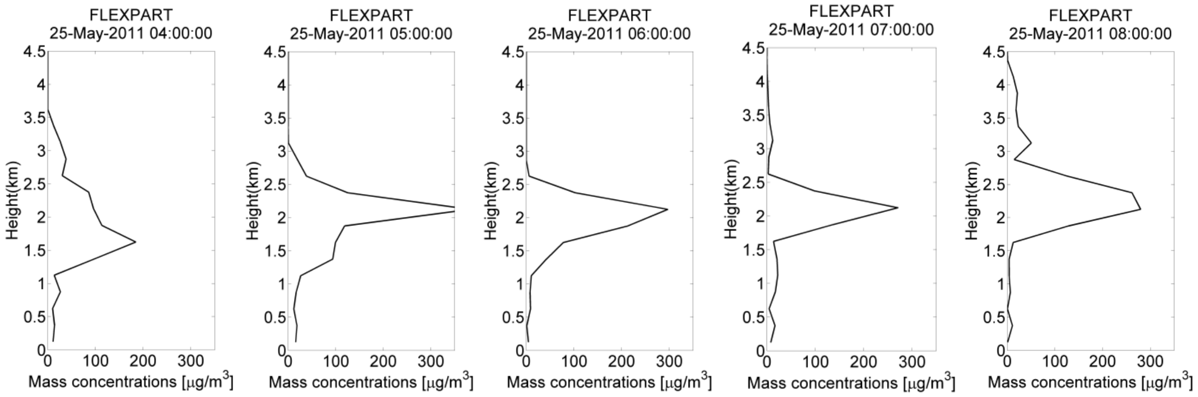

FLEXPART PM10 (IASI)

Figure 4.25: *Upper panel: Mass concentrations estimated from 30 min mean LIDAR profiles between 03:00 and 07:30 on 25 May 2011 at Stockholm. The grey area represents the range between estimated minimum and maximum values based on the different assumptions. The peaks around 1 km height are caused by swollen aerosols and unscreened thin clouds.*
Figure adapted from Tesche et al. (2012).
Lower panel: The PM10 concentrations above Stockholm as simulated by FLEXPART for hours between 03:00 and 08:00 on 25 May 2011 with the source term to the right in figure 4.12. NB: Remark that FLEXPART output dated 04:00 UTC is the hourly-mean output from 03:00 to 04:00 UTC.

4.5.3 Comparison with the London VAAC ash source term

Besides the climate impacts and health hazards of volcanic emissions, volcanic ash is also a threat to air traffic (see section 2.2). During the eruption of Grímsvötn, London VAAC produced an ash source term based on the Mastin et al. (2009) plume height versus eruption rate relationship (see section 2.6.2) using information on eruption plume heights and the timing of the different activity stages from the Icelandic Met Office, through both telephone conversations and their volcanic ash status (Met Office Report 27 May 2011). The source term estimate used an assumption on the fine ash fraction of 1 % for emissions up to and including 12 UTC on 25 May 2011 and from then and until 02:30 on 25 May a 5% fine ash mass fraction was used. This source term gave a total amount of fine ash of 15 Tg emitted during the eruption. Forward runs using the computer model called Numerical Atmospheric-dispersion Modelling Environment (NAME) with this source term using particles in the size range 1-100 µm produced the official ash mass forecasts used to guide aviation during the eruption. It is interesting to compare the ash emissions provided by the source term found in this study (the one given to the right of figure 4.12) to the ash emissions given by VAAC to see which method that produces the results closest to satellite observations. To do this, FLEXPART was run forward with the two different source terms. The upper panel of figure 4.26 shows the results for the time 10 UTC on 24 May. The satellite observations from IASI and SEVIRI instrument are given in the lower panel. Remark that the IASI observations are used to produce the source term in the inversion method and are thus not independent of the simulations with the source term produced by the inversion method.

Figure 4.26 further shows that the ash cloud located north of Great Britain is seen in both the two sets of satellite observations (upper panel) and in the two simulations (lower panel). However, the masses in the case using the VAAC source term are about a factor of 8 higher than in the simulations with the source term produced by the inversion method and a factor of 2-5 higher than what observed by the two satellite instruments (remark different color scales). The ash cloud simulated at the western coast of Denmark is not seen by any of the satellite instruments, so this is likely not true. The cloud located partly over Greenland, stretching over the North Atlantic is seen in both the simulations, but the masses are up to about a factor of 25 higher in the simulation with the VAAC source term than in the simulations with the source term produced by the inversion method. The IASI instrument is not observing the area over Greenland at this time, but SEVIRI should have been able to capture the masses in the southern part (i.e. below 70°N) of the cloud if there were any.

In summary, the VAAC ash source term seems to give an overestimating of the ash masses from a factor of 2-5 (for the south-east going cloud) to a factor of 25 (north-west going cloud over Greenland). Even though the inversion method seems to, after some time of transport, underestimate the ash masses heading south and then east of Iceland (see section 4.2) (in figure 4.26 the cloud is seen north of Great Britain), and overestimate the ash cloud over Greenland, a forecast using this source term would have provided ash masses in better agreement with observations. This could have led to fewer cancellations of air traffic (see section 2.7) and less economic costs for the aviation industry. However, it is recognized that the conservative approach taken by the VAACs is in many cases sensible, i.e. it is better to forecast too much ash than too little when alerting the aircrafts. But the approach should also consider that the forecasts should be in agreement with observations.

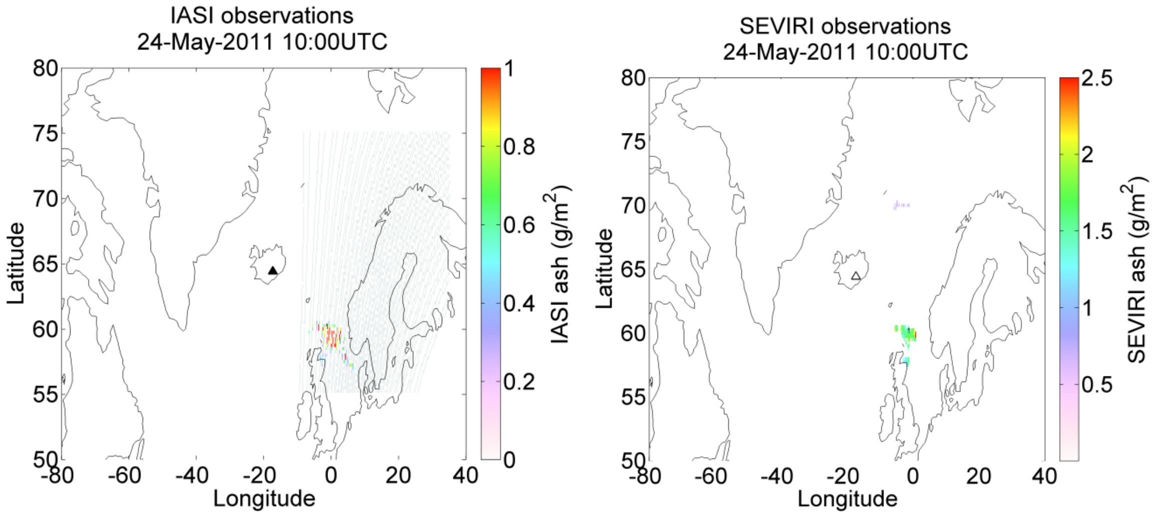

IASI observations **SEVIRI observations**

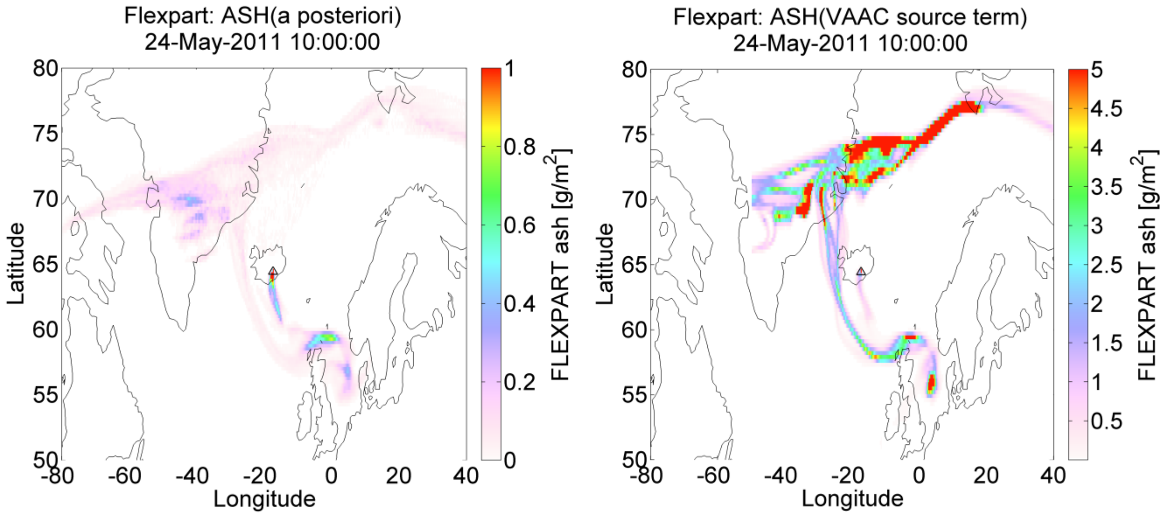

FLEXPART + source term in fig. 4.10 (left) **FLEXPART + VAAC**

Figure 4.26: Upper panel: The ash observations from IASI (left) and SEVIRI (right) on 10 UTC 24 May. Lower panel: Output from FLEXPART forward simulations on 10 UTC 24 May using the a posteriori source term produced by the inversion method (figure 4.12, right) (left) and the source term produced by London VAAC (right). Remark the differences in color scale. The FLEXPART output is scaled with the satellite size sensitivity given in figure 3.9(left).

4.6 Errors and uncertainties

All the various steps, from retrieving SO_2 and ash from the satellite measurement, to the assumptions made in the inversion method and further using the model to predict the SO_2 and ash concentrations, include uncertainties and possible errors that might affect the results. In this section, an overview of the most important uncertainties and errors is given.

First, satellite data are not perfect observations. No satellite instruments observe the SO_2 or ash directly but the quantities are estimated from the observed radiation using retrievals that are based on many assumptions. Therefore, the satellite data has to be given an error for use in the inversion method. The errors given to the satellite retrievals (see section 3.2.3), is followed by large uncertainties. Another feature is that the ash emissions of Grímsvötn 2011 eruption were much smaller than in the eruption of for example Eyjafjallajökull in 2010. This pushes the satellite retrieval algorithms to a limit something that might produce errors in the satellite data and make them look noisy.

Additionally, the satellite retrievals have certain sensitivities (see section 3.2.4) for the height of the SO_2 layer and the size of the ash particles which also affects the uncertainties when comparing to other data. In this study the SO_2 height sensitivity functions is generalized to one for IR and one for UV measurements. In fact, each instrument for measuring SO_2 has its own individual height sensitivity function.

The inversion method assumes that the errors in the satellite data are uncorrelated in time and space. This is not true since the error in one satellite pixel is much correlated to the one in adjacent pixels. Also observations done within a short time period is certainly somewhat correlated.

For the model data, the errors comes from the fact that the transport model uses input data from numerical weather prediction models which are not perfect, and also parameterizations of physical processes which are simplified in the transport model. The model error was in the inversion set to a fixed value which is a simplified approach. The model errors are also assumed to be uncorrelated in space and time.

The uncertainty of the a priori emissions can be quite large due to the large variations in the volcanic emissions which are likely too properly depicted in the a priori. In the inversion method the a priori uncertainty was set to a constant value which allowed to reduce or increase the a priori value in all parts of the source term. Using observed plume heights of ash to estimate the a priori source term might also lead to errors because of a phenomenon called “column collapse”. This is of common occurrence in explosive eruptions and happens when parts of the eruption column has a density that is greater than the surrounding air (Ishimine, 2006). Then the column cannot be lifted higher by convection, and instead falls down quickly close to the volcano. This phenomenon was observed during the Grímsvötn eruption. This means that a priori estimates using observed plume height might overestimate the emissions something that might be the reason why the Mastin’s relationship (see section 2.6.2) using the radar plume heights for this eruption gives very high emission values.

The ratio between the a priori uncertainties, the uncertainties in the satellite data and the model uncertainties is important for obtaining the most reliable a posteriori source term. If using too low a priori uncertainties, the a posteriori source term will follow the a priori source term too closely. Too low uncertainties in the satellite data will allow the a posteriori source term to rely too much on the satellite data. Too low model uncertainties will allow the solution to rely too much on the model sensitivities. A balance between the three uncertainties must be found so that all pieces of information (a priori, satellite data and model data) are used in the best way. Some testing with different uncertainties for the three has to be done to converge to a final solution.

The time resolution of the satellite data and model output sometimes needs to be approximated. For example, the SEVIRI satellite data which are available every 15 min was averaged to 1-hourly means to compare with the 1-hourly averaged model data in the inversion method. This might also lead to small errors if the volcanic clouds are transported quickly within one hour. Similarly, the choice of horizontal (0.25° x 0.25°) and vertical resolution (250 m) in the model output might affect the uncertainties.

The time resolution of the estimated source term will also not reflect the highly changing emissions. Here 3-hourly time resolution is used. This could in theory be increased to 1-hourly or even shorter, but on the cost of substantial more computation time. The reports from IMO (*http://en.vedur.is/earthquakes-and-volcanism/articles/nr/2180*) published during the eruption indicate that the Grímsvötn eruption was quite pulsating. “Radars observed a lot of pulsating activity on a timescale of about 20 minutes the first evening with a range in plume height from 3 to 20 km.” This pulsating effect will not be covered in the 3-hourly a posteriori source term.

The assumed initial particle size distribution needed in the model simulations might lead to uncertainties. Especially, using a size distribution from an ash ground sample might cause problems if not considered correctly. A ground sample taken close to the volcano will include all the large particles that fell out of the ash cloud very quickly. But for the model simulation the size distribution for the particles that are considered to take part in the long-range-transport, i.e. the smaller particles is needed. The most accurate distribution is achieved by taking measurements from appropriate instruments on an aircraft flying into the ash cloud during or right after the eruption. However, due to weather conditions and the risk of flying into very thick ash clouds, such measurements are usually not possible to achieve. Then more inaccurate ground samples can be used, but one needs to consider that this size distribution is shifted to larger particles. Only the smaller particles of the sampled size distribution can be used. In the simulations, it is also assumed that the initial particle size distribution stays the same throughout the whole eruption period which is probably not realistic considering the complexity of dynamic eruptions.

There are also physical processes for volcanic ash that affect the airborne concentrations. Aggregation is caused by collision of ash particles and their ability to adhere, and can result in efficient removal of ash from the atmosphere. At the moment the FLEXPART model does not account for ash aggregation something that may lead to overestimating of the ash concentrations in the transport simulations. However, for long range transport it might be assumed that using the fine ash fraction to some extent accounts for the loss by this effect since aggregation mainly is a near-source process (Webster et al., 2012).

Chapter 5

Summary and conclusion

For the first time an inversion method was used to estimate the individual source terms for SO_2 and ash from a volcanic eruption. This was done by using total column measurements of SO_2 and ash from satellite instruments and a Lagrangian dispersion model, FLEXPART as well as some a priori estimates for the source term. The method was applied to the eruption of Grímsvötn volcano in May 2011. Summary and concluding remarks from the study are given in the following.

The source term for SO_2 was obtained by using observations from the IASI satellite instrument from 0-13 days after the eruption onset. As a priori estimate a distribution based on ash radar heights and scaled to contain a total SO_2 mass of 0.4 Tg (equal to the total observed SO_2 mass from IASI) was used. The inversion method optimizes the emissions and estimates the a posteriori source term which showed that SO_2 was emitted mostly to 8-14 km altitude during 22 May. The total SO_2 a posteriori mass was about 0.8 Tg which was a doubling of the a priori estimate. As the IASI measurements cannot detect SO_2 below 5 km height, any conclusions regarding the mass below this height could not be taken directly. However, comparing with other satellite instruments able to detect low altitude SO_2 suggest that very little SO_2 was present at low altitudes.

For ash, the inversion method was run using two different sets of satellite observations, one from IASI (using observations from 1-4 days after the eruption) and one from the SEVIRI instrument (with observations from 1-3 days after the eruption onset). The a priori source terms were also here based on ash radar heights and scaled to an estimate of the total observed fine ash mass, namely 0.4 Tg. The a posteriori source terms from the two inversions based on different satellite data were quite similar and showed that the ash was mostly emitted below 4 km height during the three first days of the eruption (from 21-23 May). Some ash was emitted to higher altitudes, to the same height and in the same time period as $SO_{2.}$ The total mass in the a posteriori source term is similar to the a priori with a maximum of 30 % increase in one of the cases.

Furthermore, some sensitivity tests were performed for the source term estimations:

- To reduce the probability of errors, two different sets of meteorological input data (ECMWF and GFS) was used for the FLEXPART model simulations used as input to the inversion. For the SO_2 inversions the results were not sensitive to the meteorological input data but for the ash inversions some differences were notable but mostly only for the very early emissions.

- The start time of the simulated eruption period was further evaluated. This was performed to check whether the inversion successfully could estimate the start time of the emissions even when considering time intervals earlier than the reported eruption start (where emissions might have happened). For SO_2 the source term estimates were independent of the starting time of the simulated eruption period while for the ash case a significant amount of ash was released in the first 6 hours of the simulated eruption period (12-18 UTC on 21 May) which was before the reported start of the eruption. These early emissions were dependent on the starting time, i.e. they changed when the simulated eruption period was changed. They also changed between the two inversions based on different satellite data, and when the meteorological input data changed (in the previous sensitivity test). It was therefore suggested that these early ash emissions were probably largely unrealistic. In the ash case the emission start was a required a priori constraint while for SO_2 this constraint was not needed and the inversion could well estimate the starting time of the SO_2 emissions.

- The amount of satellite data used to estimate the source terms was evaluated. This test showed that even with only one satellite overpass from less than one day after the start of the eruption both the SO_2 and ash source terms could be well reproduced. Only for the ash case later satellite data was required to estimate the low altitude emissions which were observed only somewhat later.

- The shape and magnitude of the a priori estimate was changed to test the results. Both the SO_2 and ash inversions were run with the “original” a priori based on ash radar heights, a zero a priori and an a priori with mass uniformly distributed up to 20 km height. The a posteriori seems to be very stabile to changes in the a priori. This is preferable since it means that the problem is well constrained with satellite observations, but on the other hand it shows that the a priori, which might help the solution getting closer to real results, is nearly not used.

The transport of SO_2 and ash was simulated with FLEXPART using the a posteriori source terms. The model simulated a clear separation of SO_2 and ash with the SO_2 first moving north and then westward and most of the ash first moving south and the eastward. There is also some ash being transported north and then westward together with the SO_2.

The SO_2 model simulations were validated against independent satellite observations from the GOME-2, SCIAMACHY and AIRS instruments. The simulated SO_2 clouds were quite similar to those observed by the different satellite instruments. However, the simulated masses located at the southern part of Greenland seem to be somewhat overestimated probably due to errors in the meteorological and/or satellite data.

The SO_2 mass emitted into the stratosphere was estimated to 0.5 Tg. This was not a major stratospheric injection compared to other eruptions, but on the other hand the time of the eruption was at the beginning of the period with the most insolation (i.e. in spring), thus the stratospheric sulphate aerosols that were formed from the SO_2 emissions would have the possibility to alter the radiative transmission in the atmosphere when a lot of sunlight was present. Simulations to investigate the potential climate effects of the Grímsvötn eruption would be of great interest, but is not yet performed.

The ash model simulations were validated with surface and LIDAR measurements at stations in Sweden and southern part of Norway and Finland. The simulated ash cloud arrived at the measurement sites at exactly the same time as significant increases in the surface observations were seen. But the simulated concentrations were generally somewhat lower than the observations. This was suggested to be because of too effective removal processes implemented in the FLEXPART method. The height of the simulated ash cloud over Stockholm fitted quite well to the observation by a LIDAR.

The ash source terms produced by the inversion method was compared to the source term produced by London VAAC during the eruption. While the ash masses are strongly overestimated in the VAAC source term, the inversion method seems to produce masses in better agreement with observations, though a bit too low after some time of transport which might be due to the removal processes in the model.

The inversion method can be implemented as a part of an operational setting, and by that provide estimates of source term and thereby transport patterns during an ongoing eruption. The critical part is the need of satellite data quite fast after the eruption onset. It would be preferable to use observations from an instrument on a geostationary satellite since this can give more information faster (every 15th minute from for example the SEVIRI instrument). In an operational setting, the satellite retrievals could be produced continuously and then implemented into the inversion method. The inversion method is fast and can theoretically be re-run every 15 minute when new retrievals arrive from a geostationary satellite. If using retrievals from polar orbiting satellites, the inversion method can be re-run for example every six hour. This study has shown that the method is able to distinguish between SO_2 and ash. This can help to make both the SO_2 and ash forecasts more precise which is especially important in the cases when SO_2 is used as an approximation for ash.

The improved ash and SO_2 forecasts based on the estimated source term can more correctly define the area needed to be closed for air traffic during and after an eruption. During large eruptions with large amounts of ash emitted, the concentrations of ash in the planetary boundary layer can be given more precisely helping to evaluate potential air quality problems affecting humans and the environment. The method can also be used for less time critical applications, such as determining the source term and particularly the injection height and masses for climate purposes.

Bibliography

Aguado, E. and J.E Burt. (1998), Understanding Weather and Climate, 5th ed., Pearson Education, Inc, p. 229-231.

Ansmann, A., P. Seifert, M. Tesche, and U. Wandinger. (2012) Profiling of fine ash and coarse particle mass: case studies of Saharan dust and Eyjafjallajökull/Grímsvötn volcanic plumes, Atmospheric Chemistry and Physics, Vol. 12, p. 9399-9415. doi: 10.5194/acp-12-9399-2012.

Bernard, A. and W.I Rose. (1984) The injection of sulfuric acid aerosols in the stratosphere by the El Chichon volcano and its related hazards to the international air traffic, Natural Hazards, Vol 3(1), p. 59–67. doi:10.1007/BF00144974.

Bey I, D. J. Jacob, R.M. Yantosca, et al. (2001) Asian chemical outflow to the Pacific in spring: Origins, pathways, and budgets, Journal of Geophysical Research, Vol. 106(19), p. 23073-23095.

Brasseur, G.P, J.J Orlando, and G.S Tyndall (1999), Atmospheric Chemistry and Global Change, Oxford University Press, p. 508-509.

Carn, S.A, A.J Prata, S. Karlsdottir. (2008) Circumpolar of a volcanic cloud from Hekla(Iceland), Journal of Geophysical Research, Vol 113. doi: 10.1029/2008JD009878.

Cas, R.A.F. and J.V. Wright. (1987) Volcanic Successions, Unwin Hyman Inc. 528p. ISBN 0-04-552022-4

Clarisse, L., P.F Coheur, A.J Prata, D. Hurtmans, A. Razavi, T. Phulpin, J. Hadji-Lazaro, and C. Clerbaux. (2008) Tracking and quantifying volcanic SO2 with IASI, the September 2007 eruption at Jebel at Tair, Atmospheric Chemistry and Physics, Vol. 8, p. 7723–7734. doi:10.5194/acp-8-7723-2008.

Clarisse, L., D. Hurtmans, A. J.,Prata, F. Karagulian, C. Clerbaux, M.D Mazière, and P.-F Coheur. (2010) Retrieving radius, concentration, optical depth, and mass of different types of aerosols from high-resolution infrared nadir spectra, Applied Optics, Vol. 49 (19), p. 3713-3722.

Clarisse, L., D. Hurtmans, C. Clerbaux, J. Hadji-Lazaro, Y. Ngadi, P.-F. Coheur. (2012) Retrieval of sulphur dioxide from the infrared atmospheric sounding interferometer (IASI), Atmospheric Measurement Techniques, Vol. 5, p. 581-594. doi: 10.5194/amt-5-581-2012.

Clarisse, L., P.-F. Coheur, A. J. Prata, J. Hadji-Lazaro, D. Hurtmans and C. Clerbaux. (2013) A unified approach to infrared aerosol remote sensing and type specification, Atmospheric Chemistry and Physics, Vol. 13 (4), p. 2195-2221.

Dacre, H. F., A. L. M. Grant, R. J. Hogan, S. E. Belcher, D. J. Thomson, B. J. Devenish, F. Marenco[2], M. C. Hort, J. M. Haywood, A. Ansmann, I. Mattis, L. Clarisse. (2011) Evaluating the structure and magnitude of the ash plume during the initial phase of the 2010 Eyjafjallajökull eruption using lidar observations and NAME simulations, Journal of Geophysical Research, Vol. 116(D20). doi:10.1029/2011JD015608.

Degruyter, W., and C. Bonadonna. (2012) Improving on mass flow rate estimates of volcanic eruptions, Geophysical Research Letters, Vol. 39(16). doi:10.1029/2012GL052566.

Dellino, P., M. T. Gudmundsson, G. Larsen, D. Mele, J. A. Stevenson, T. Thordarson, and B. Zimanowski. (2012) Ash from the Eyjafjallajökull eruption (Iceland): Fragmentation processes and aerodynamic behavior, Journal of Geophysical Research, Vol. 117. doi: 10.1029/2011JB008726.

Dufresne, J.-L., J. Quaas, O. Boucher, S. Denvil, and L. Fairhead. (2005) Contrasts in the effects on climate of anthropogenic sulfate aerosols between the 20th and the 21st century, Geophysical Research Letters, Vol. 32(21). doi:10.1029/2005GL023619

Durant, A.J., C. Bonadonna, and C. J. Horwell. (2010) Atmospheric and Environmental Impacts of Volcanic Particulates, Elements, 6(4), p. 235-240.
doi: 10.2113/gselements.6.4.235.

Eckhardt, S., A. J. Prata, P. Seibert, K. Stebel, and A. Stohl. (2008) Estimation of the vertical profile of sulfur dioxide injection into the atmosphere by a volcanic eruption using satellite column measurements and inverse transport modeling, Atmospheric Chemistry and Physics, Vol. 8, p. 3881–3897.

Ganse, A. (2007). A Geophysical Inverse Theory Primer, University of Washington, Seattle.

Graf, H.-F, Q. Li, and M. A. Giorgetta. (2007) Volcanic effects on climate: revisiting the mechanisms, Atmospheric Chemistry and Physics, Vol. 7, p. 4503-4511.

Gudmundsson, M. T.,T. Thordarson, Á. Höskuldsson, G. Larsen, H. Björnsson, A. J. Prata, B. Oddsson, E. Magnússon, T. Högnadóttir, G. N. Petersen, C. L. Hayward, J. A. Stevenson, and I. Jónsdóttir. (2012a) Ash generation and distribution from the April-May 2010 eruption of Eyjafjallajökull, Iceland, Scientific Reports, Vol. 2. doi:10.1038/srep00572

Gudmundsson, M. T., et al. (2012b) The May 2011 eruption of Grímsvötn, EGU General Assembly Conference Abstracts, Vol. 14, found at:
http://meetingorganizer.copernicus.org/EGU2012/EGU2012-12119.pdf

Guffanti M., T.J. Casadevall, and G. Mayberry. (2004) Reducing encounters of aircraft with volcanic-ash clouds. In: Second international conference on volcanic ash and aviation safety. Alexandria, Virginia, USA, p. 1/17–21

Hertel, O., J. Christensen, E. H. Runge, W. A. H. Asman, R. Berkowicz, M. F. Hovmand, and O. Hov. (1995) Development and testing of a new variable scale air pollution model – ACDEP, Atmospheric Environment, Vol. 29, p. 1267–1290.

Holasek, R.E, A. W. Woods, and S. Self. (1996) Experiments on gas-ash separation processes in volcanic umbrella plumes, Journal of Volcanology and Geothermal Research,Vol. 70(3-4), p. 169-181, doi: 10.1016/0377-0273(95)00054-2

ICAO: EUR DOC 019 –Volcanic Ash Contingency Plan – EUR and NAT regions (2nd Edition), International Civil Aviation Organization, 2010.

ICAO (2007), Manual on Volcanic Ash, Radioactive Material and Toxic Chemical Clouds, International Civil Aviation Organization, Montreal, Que., Canada. *http://www.paris.icao.int/news/pdf/9691.pdf*.

IPCC (2007), Climate Change 2007: The Physical Science Basis. Contribution of Working Group I to the Fourth Assessment Report of the Intergovernmental Panel on Climate Change [Solomon, S., D. Qin, M. Manning, Z. Chen, M. Marquis, K.B. Averyt, M.Tignor and H.L. Miller (eds.)]. Cambridge University Press, Cambridge, United Kingdom and New York, NY, USA.

Ishimine, Y. (2006) Sensitivity of the dynamics of volcanic eruption columns to their shape, Bulletin of Volcanology, Vol. 68, p. 516–537. doi: 10.1007/s00445-005-0027-4

Jacob, D.J (1999), Introduction to Atmospheric Chemistry, Princeton University Press.

Karnieli, A., Y. Derimian, R. Indoitu, N. Panov, R. C. Levy, L. A. Remer, W. Maenhaut, and B. N. Holben. (2009) Temporal trend in anthropogenic sulfur aerosol transport from central and eastern Europe to Israel, Journal of Geophysical Research, Vol. 114(D10). doi:10.1029/2009JD011870.

Kerminen, V.-M., J. V. Niemi, H. Timonen, M. Aurela, A. Frey, S. Carbone, S. Saarikoski, K. Teinilä, J. Hakkarainen, J. Tamminen, J. Vira, M. Prank, M. Sofiev, and R. Hillamo. (2011) Characterization of a volcanic ash episode in southern Finland caused by the Grimsvötn eruption in Iceland in May 2011, Atmospheric Chemistry and Physics, Vol. 11, p. 12227–12239. doi:10.5194/acp-11-12227-2011

Kravitz, B., A. Robock, and A. Bourassa. (2010), Negligible climatic effects from the 2008 Okmok and Kasatochi volcanic eruptions, Journal of Geophysical Research, Vol. 115(D00L05). doi:10.1029/2009JD013525.

Kristiansen, N. I. (2009), Determination of the emission height profile of volcanic emissions using inverse modelling, Master's thesis, 82 pp., Dep.of Geosci., Univ. of Oslo, Oslo, Norway.

Kristiansen, N. I. (2012), Quantifying emission sources, transport and removal time scales of atmospheric pollutants, Dissertation for the degree of Philosophiae Doctor, 64 pp., Department of Geosciences, Univ. of Oslo, Oslo, Norway.

Kristiansen, N. I., A. Stohl, A. J. Prata, A. Richter, S. Eckhardt, P. Seibert, A. Hoffmann, C. Ritter, L. Bitar, T. J. Duck and K. Stebel (2010), Remote sensing and inverse transport modeling of the Kasatochi eruption sulfur dioxide cloud, Journal of Geophysical Research, Vol. 115(D2). doi:10.1029/2009JD013286.

Kristiansen, N. I., A. Stohl, A. J. Prata, N. Bukowiecki, H. Dacre, S. Eckhardt, S. Henne, M. C. Hort, B. T. Johnson, F. Marenco, B. Neininger, O. Reitebuch, P. Seibert, D. J. Thomson, H. N. Webster, B. Weinzierl. (2012) Performance assessment of a volcanic ash transport model mini-ensemble used for inverse modeling of the 2010 Eyjafjallajökull eruption, Journal of Geophysical Research, Vol. 117(D3). doi:10.1029/2011JD016844.

Krueger A. J. (1983) Sighting of El Chichon sulfur dioxide clouds with the Nimbus 7 total ozone mapping spectrometer, Science, Vol. 220, p. 1377–1379

Krueger, A., L. Walter, P. Bhartia, C. Schnetzler, N. Krotkov, I. Sprod, and G. Bluth. (1985) Volcanic sulfur dioxide measurements from the Total Ozone Mapping Spectrometer (TOMS) Instruments, Journal of Geophysical Research, Vol. 100, p. 14057–14076.

Krueger, A. J., C. C Schnetzler, and L. S Walter. (1996) The December 1981 eruption of Nyamuragira volcano (Zaire), and the origin of the ‘mystery cloud’ of early 1982, Journal of Geophysical Research, Vol.101, p. 15191–15196.

Mastin, L. G. (2007) A user-friendly one-dimensional model for wet volcanic plumes, Geochemistry, Geophysics, Geosystems,Vol. 8(3). doi:10.1029/2006GC001455

Mastin, L.G, M. Guffani, R. Servranckx, P. Webley, S. Barsotti, K. Dean, A. Durant, J.E. Ewert, A. Neri, W. I. Rose, D. Schneider, L. Siebert, B. Stunder, G. Swanson, A. Tupper, A. Volentik, C.F. Waythomas. (2009a) A multidisciplinary effort to assign realistic source parameters to models of volcanic ash-cloud transport and dispersion during eruptions, Journal of Volcanology and Geothermal Research, Vol. 186, p. 10-21.

Mastin, L.G., M. Guffanti, J.E Ewert, and J. Spiegel. (2009b) Preliminary spreadsheet of eruption source parameters for volcanoes of the world: U.S. Geological Survey Open-File Report 2009-1133, Vol. 1.2, 25 p.

McMahon, T. A. and P. J. Denison. (1979) Empirical atmospheric deposition parameters – a survey, Atmospheric Environment, Vol. 13, p. 571–585.

Merucci, L., M.R. Burton, S. Corradini, and G.G Salerno. (2011) Reconstruction of SO2 flux emission chronology from space-based measurements, Journal of Volcanology and Geothermal Research, Vol. 206, p. 80–87.

Morrissey, M., B. Zimanowski, K. Wohletz, and R. Buettner. (2000) Phreatomagmatic fragmentation, in Encylopedia of Volcanoes, edited by H. Siggurdsson, p. 431–445, Academic, San Diego, Calif.

Newhall, C. G., and S. Self. (1982) The Volcanic Explosivity Index(VEI) An Estimate of Explosive Magnitude for Historical Volcanism, Journal of Geophysical Research, 87(C2), p. 1231-1238. doi: 10.1029/JC087iC02p01231.

Platt, U. and J. Stutz. (2008) Differential Optical Absorption Spectroscopy (DOAS), Principle and Applications, ISBN 3-340-21193-4, Springer Verlag, Heidelberg.

Prata, A. J. (1989) Infrared radiative transfer calculations for volcanic ash clouds, Geophysical Research Letters, Vol. 16(11), p. 1293-1296.

Prata, A.J. (2008) Satellite detection of hazardous volcanic clouds and the risk to global air traffic, Naural Hazards, Vol. 51, p. 303-324. doi:10.1007/s11069-008-9273-z.

Prata, A.J, W.I Rose, S. Self, and D.M O'Brien. (2003) Global long-term sulphur dioxide measurements from TOVS data: a new tool for studying explosive volcanism and climate, Volcanism and the Earth's atmosphere, Geophysics monograph, 139 AGU, p. 75-92.

Prata, A.J and C. Bernardo. (2007). Retrieval of volcanic SO2 column abundance from Atmospheric Infrared Sounder data, Journal of Geophysical Research, Vol. 112(D20). doi:10.1029/2006DJ007955.

Prata, A. and J. Kerkmann. (2007) Simultaneous retrieval of volcanic ash and SO2 using MSG-SEVIRI measurements, Geophysical Research. Letters, Vol. 34(L05813) doi:10.1029/2006GL028691.

Prata, A.J, S. C. Carn, A. Stohl, and J. Kerkmann. (2007) Long range transport and fate of a stratospheric volcanic cloud from Soufriere Hills volcano, Montserrat, Atmospheric Chemistry and Physics, Vol. 7, p. 5093-5103

Prata, A. J., and A. Tupper. (2009) Aviation hazards from volcanoes: the state of the science, Natural Hazards, Vol. 51(2), p. 239–244.

Prata, A. J. and A. T. Prata. (2011) Eyjafjallajökull volcanic ash concentrations determined from SEVIRI measurements, Journal of Geophysical Research, Vol. 117(D20).

Penner, J. E, C. C. Chuang, K. Grant. (1998) Climate forcing by carbonaceous and sulfate aerosols, Climate dynamics, Vol. 14, p. 839-851.

Petersen, G. N, H. Bjornsson, P. Arason, and S. von Löwis. (2012) Two weather radar time series of the altitude of the volcanic plume during the May 2011 eruption of Grimsvötn, Iceland, Earth System Sciende Data, Vol. 4(1), p. 121-127. doi: 10.5194/essd-4-121-2012

Petersen, G. N et al. (2012) Altitude estimates of the volcanic plume-top of Grimsvötn measured by C-band weather radar (Keflavik), doi: 10.1594/PANGAEA.778386 (The data from weather radar)

Randel, W. J., F. Wu, J. M. Russel III, J. W. Waters, and L. Froidevaux. (1995) Ozone and temperature changes in the stratosphere following the eruption of Mt. Pinatubo, Journal of Geophysical Research, Vol. 100(D8), p. 16753-16764.

Robock, A. (2000) Reviews of Geophysics, Vol. 38, p. 191-219.

Røed, L. P (2011) Atmospheres and Oceans on Computers: Fundamentals, Lecture notes written for the course GEF4510 at the Meteorology and Oceanography Section, Department of Geosciences, University of Oslo.

Schminke, H.-U., Volcanism, Springer-Verlag Berlin Heidelberg, 2004

Seibert, P. (2000) Inverse modelling of sulfur emissions in Europe based on trajectories, in Inverse Methods in Global Biogeochemical Cycles (edited by P. Kasibhatla, M. Heimann, P. Rayner, N. Mahowald, R. G. Prinn and D. E. Hartley), American Geophysical Union, Washington, D. C., p. 147-154. doi: 10.1029/GM114p0147

Seibert, P., and A. Frank. (2004), Source-receptor matrix calculation with a Lagrangian particle dispersion model in backward mode, Atmospheric Chemistry and Physics, Vol. 4(1), p. 51-63. doi: 10.5194/acp-4-51-2004.

Seibert, P., N.I Kristiansen, S. Eckhardt, A.J Prata, A. Richter, and A. Stohl. (2011) Uncertainties in the inverse modelling of sulphur dioxide eruption profiles, Geomatics, Natural Hazards and Risk, Vol. 2(3), p. 201-216. doi: 10.1080/19475705.2011.590533.

Seifert, P., A. Ansmann, S. Groß, V. Freudenthaler, B. Heinold, A. Hiebsch, I. Mattis, J. Schmidt, F. Schnell, M. Tesche, U. Wandinger, and M. Wiegner. (2011) Ice formation in ash-influenced clouds after the eruption of the Eyjafjallajökull volcano in April 2010, Journal of Geophysical Research, Vol. 116(D20). doi:10.1029/2011JD015702.

Sheridan M.F, K.H, Wohletz. (1983) Hydrovolcanism: basic considerations and review, Journal of Volcanology and Geothermal Research, Vol. 17, p. 1-29.

Sigmarsson, O., I. Vlastelic, R. Andreasen, I. Bindeman, J.-L. Devidal, S. Moune, J. K. Keiding, G. Larsen, A. Höskuldsson, and Th. Thordarson. (2011) Remobilization of silicic intrusion by mafic magmas during the 2010 Eyjafjallajökull eruption, Solid Earth, Vol. 2, p. 271–281. doi:10.5194/se-2-271-2011

Sparks, R. S. J., M. I. Bursik, S. N. Carey, J. S. Gilbert, L. S. Glaze, H. Sigurdsson, and A. W. Woods (1997), Volcanic Plumes, 574 pp., John Wiley, Chichester, U. K.

Stohl, A. (1998) Computation, accuracy and application of trajectories – a review and bibliography, Atmospheric Environment, Vol. 32(6), p. 947-966.

Stohl, A., M. Hittenberger, and G. Wotawa. (1998) Validation of the Lagrangian Particle Dispersion model FLEXPART against large-scale tracer experiment data, Atmospheric Environment, Vol. 32(24), p. 4245–4264. doi:10.1016/S1352-2310(98)00184-8

Stohl, A., C. Forster, A. Frank, P. Seibert, and G. Wotawa. (2005) Technical note: The Lagrangian particle dispersion model FLEXPART version 6.2, Atmospheric Chemistry and Physics, Vol. 5(9), p. 2461–2474.

Stohl, A., A. J. Prata, S. Eckhardt, L. Clarisse, A. Durant, S. Henne, N. I. Kristiansen, A. Minikin, U. Schumann, P. Seibert, K. Stebel, H. E. Thomas, T. Thorsteinsson, K. Tørseth and B.Weinzierl. (2011) Determination of time- and height-resolved volcanic ash emissions and their use for quantitative ash dispersion modeling: the 2010 Eyjafjallajökull eruption, Atmospheric Chemistry and Physics, Vol. 11, p. 4333-4351. doi:10.5194/acp-11-4333-2011, 2011.

Stohl, A., P. Seibert, G. Wotawa, D. Arnold, J. F. Burkhart, S. Eckhardt, C. Tapia, A. Vargas, and T. J. Yasunari. (2012) Xenon-133 and caesium-137 releases into the atmosphere from the

Fukushima Dai-ichi nuclear power plant: determination of the source term, atmospheric dispersion, and deposition, Atmospheric Chemistry and Physics, Vol. 12, p. 2313-2343. doi:10.5194/acp-12-2313-2012, 2012.

Tesche, M., P. Glantz, C. Johansson, M. Norman, A. Hiebsch, A. Ansmann, D. Althausen, R. Engelmann, and P. Seifert. (2012) Volcanic ash over Scandinavia originating from the Grimsvötn eruptions in May 2011, Journal of Geophysical Research, Vol. 117. doi:10.1029/2011JD017090.

Textor C., H.-F. Graf, M. Herzog, and J.M. Oberhuber. (2003) Injection of gases into the stratosphere by explosive volcanic eruptions, Journal of Geophysical Research, Vol. 108(D19), p. 4606. doi: 10.1029/2002JD002987.

Theys, N., R. Campion, L. Clarisse, H. Brenot, J. van Gent, B. Dils, S. Corradini, L. Merucci, P.-F. Coheur, M. van Roozendael, D. Hurtmans, C. Clerbaux, S. Tait, and F. Ferrucci. (2012) Volcanic SO2 fluxes derived from satellite data: a survey using OMI, GOME-2, IASI and MODIS, Atmospheric Chemistry and Physics Discuss., Vol. 12, p. 31349–31412.

Thomas, H.E and A.J. Prata. (2011) Sulphur dioxide as a volcanic ash proxy during the April-May 2010 eruption of Eyjafjallajökull Volcano, Iceland, Atmospheric Chemistry and Physics, Vol. 11, p. 6871-6880. doi: 10.5194/acp-11-6871-2011.

United States Environmental Protection Agency, EPA, *http://www.epa.gov/climatechange/science/causes.html*

Webster, H. N., D. J. Thomson, B. T. Johnson, I. P. C. Heard, K. Turnbull, F. Marenco, N. I. Kristiansen, J. Dorsey, A. Minikin, B. Weinzierl, U. Schumann, R. S. J. Sparks, S. C. Loughlin, M. C. Hort, S. J. Leadbetter, B. J. Devenish, A. J. Manning, C. S. Witham, J. M. Haywood,and B. W. Golding. (2012), Operational prediction of ash concentrations in the distal volcanic cloud from the 2010 Eyjafjallajökull eruption, Journal of Geophysical Research, Vol. 117(D00U08). doi:10.1029/2011JD016790.

Wesely, M. L. and Hicks, B.B. (1977) Some factors that affect the deposition rates of sulfur dioxide and similar gases on vegetation, Journal of the Air Pollution Control Association, Vol. 27(11), p. 1110-1116.

Wigley, T.M.L. (2006) A combined mitigation/geoengineering approach to climate stabilization. Science, Vol. 314, p. 452-454. doi: 10.1126/science.1131728

Wilson, L., R. S. J. Sparks, and G. P. L. Walker. (1980) Explosive volcanic eruptions—IV. The control of magma properties and conduit geometry on eruption column behavior, Geophysical Journal of the Royal Astronomical Society, Vol. 63, p. 117–148.

Wilson, L., and G. P. L. Walker. (1987) Explosive volcanic eruptions—VI. Ejecta dispersal in plinian eruptions: The control of eruption conditions and atmospheric properties, Geophysical Journal of the Royal Astronomical Society, Vol. 89(2), p. 657–679.

Witham, C.S, M. C. Hort, R. Potts, R. Servranckx, P. Husson and F. Bonnardot. (2007) Comparison of VAAC atmospheric dispersion models using the 1 November 2004 Grimsvötn eruption, Metorological Applications, Vol. 14, p. 27-38.

Wohletz, K.H. (1986) Explosively magma-water interactions: Thermodynamics, explosion mechanisms and field studies, Bulletin of Volcanology, Vol. 48, p. 245-264.

Zehner, C. Ed. (2012) Monitoring Volcanic Ash from Space, ESA-EUMETSAT workshop on the 14 April to 23 May 2010 eruption at the Eyjafjöll volcano, South Iceland (ESA/ESRIN), 26-27 May 2010), ESA Publication STM-280. doi: 10.5270/atmch-10-01.

Zimanowski, B. (2000), Physics of phreatomagmatism. Part 1: explosion physics, Terra Nostra, Vol. 6, p. 515–523.